UCLA
UCLA Electronic Theses and Dissertations

Title

A Class of Solid-like Electrolytes for Rechargeable Batteries Based on Metal-Organic Frameworks Infiltrated with Liquid Electrolytes

Permalink

https://escholarship.org/uc/item/0475g9c3

Author

Ma, Shengxiang

Publication Date

2020

Peer reviewed|Thesis/dissertation

UNIVERSITY OF CALIFORNIA

Los Angeles

A Class of Solid-like Electrolytes for Rechargeable Batteries

Based on Metal-Organic Frameworks Infiltrated with Liquid Electrolytes

A dissertation submitted in partial satisfaction of the

requirements for the degree of Doctor of Philosophy

in Chemical Engineering

by

Shengxiang Ma

2020

ABSTRACT OF THE DISSERTATION

A Class of Solid-like Electrolytes for Rechargeable Batteries

Based on Metal-Organic Frameworks Infiltrated with Liquid Electrolytes

by

Shengxiang Ma

Doctor of Philosophy in Chemical Engineering

University of California, Los Angeles, 2020

Professor Yunfeng Lu, Chair

Energy storage and conversion are key technologies in modern society, and they are becoming more and more important. This is mainly due to the severe future impact of fossil fuels on the world's economy and ecology. So, there is an urgent need for alternative energy sources to address the depletion of fossil fuels and the environmental impact of their continued use. However, the large-scale development of renewable energy resources such as wind, solar, geothermal, biomass and hydropower, that are unpredictable and intermittent. Thus, these technologies require highly reliable electrical energy storage (EES) devices, which can store the excess produced electricity and release it on demand.

Rechargeable batteries such as lithium-ion batteries, store energy through electrochemical reactions that typically occur throughout the bulk active materials, allowing comparatively large

amount of energy to be stored compared with electric capacitors. The last decade has witnessed a tremendous growth in lithium-ion batteries for applications such as microelectronics and electric vehicles. However, the development of battery energy density has seriously lagged behind the demand growth of Li-ion batteries. Thus, high energy density electrode materials are extremely demanded in next-generation cutting-edge electronic devices. Parallel to this development, rechargeable batteries based on Na^+, K^+, Mg^{2+} and Al^{3+} ions have also attracted great interests due to their abundance and low cost.

Such batteries generally employ flammable liquid electrolytes, which bring severe safety concerns. In this case, solid electrolytes are believed to be able to suppress Li dendrite growth because of their high mechanical strength and high Li^+ transference number. In order to allow the implementation of high-specific-energy Li-metal batteries, both inorganic and organic solid electrolytes have been explored. Inorganic electrolytes may exhibit high ionic conductivity (e.g., > 10^{-4} S cm^{-1}), whereas scale fabrication of solid batteries remains challenging. Polymeric electrolytes are less difficult to be integrated, whereas their ionic conductivity remains low at ambient temperature (e.g., < 10^{-5} S cm^{-1}). Solid-like electrolytes, which are generally made by encapsulating liquid electrolytes within solid porous scaffolds, represent another direction with the merits of both liquid electrolyte and solid electrolyte.

In this dissertation, we developed a novel family of solid-like electrolytes, which are made by infiltrating MIL-100(Al), a MOF with high porosity and excellent thermal, chemical and electrochemical stabilities, with a series of liquid electrolytes that contain cations from the 3rd period (Na^+, Mg^{2+} and Al^{3+}) and the 1st group (Li^+, Na^+, K^+ and Cs^+). Particularly, the Mg^{2+} solid-like electrolyte exhibits superionic conductivity (>10^{-3} S cm^{-1}) with a low activation energy of 0.20 eV. From Li^+, Na^+, K^+ to Cs^+ with reducing Stokes radii and ionic solvation shell thickness,

both the liquid electrolytes and solid-like electrolytes show a similar trend of increasing conductivity. This work investigates the ion-conduction mechanism of MOFs based solid-like electrolytes, providing reliable principles to the design of fast-conducting solid-like electrolytes for alkali or multivalent metal ions.

Furthermore, we successfully employed MOF-based solid-like electrolytes in Na-metal batteries. Both MOF/polymer composite electrolytes on GF served as functional separator or directly as gel polymer electrolytes show advantages compared with commercial separators. The cell using solid-like electrolyte notably surpasses the cell using liquid electrolyte in terms of cycle stability and Coulombic efficiency. This work expands the application of MOF-based solid-like electrolytes from Li to Na metal batteries, offering the possibility for further applications in high energy density rechargeable batteries.

The dissertation of Shengxiang Ma is approved.

Dante A. Simonetti

Vasilios Manousiouthakis

Ximin He

Yunfeng Lu, Committee Chair

University of California, Los Angeles

2020

TO MY FAMILY

TABLE OF CONTENTS

LIST OF FIGURES

LIST OF TABLES

ACKNOWLEDGEMENTS

I really appreciate the opportunity to be able to pursue my Ph.D. in UCLA, such a beautiful and diverse university. I have learned a lot during my journey at UCLA, not only the research and academic knowledge, but also the interaction with people. Here, I am indebted to so many people who have helped me through my Ph.D. study.

Firstly, I would like to express my sincere gratitude to my principle advisor Prof. Yunfeng Lu for the continuous support of my Ph.D. study and related research, for his patience, motivation, and immense knowledge. In particular, the ability to turn the knowledge studied from books and papers to creative ideas in research is the most important lesson I learned from Prof. Lu. I am always impressed by his endless and diverse knowledge background in science, not only in energy storage devices but also in drug delivery and nanomedicine field. This inspires me to think broader and keep myself learning from everywhere. Laboratory work is replete with challenges in every project; however, Prof. Lu encouraged me to regard setbacks as precious opportunities for training and developing my competencies in persistence and critical thinking to solve the problems. I have not gone back China since my graduate study abroad, Prof. Lu invited us to his house for dinner every Thanksgiving, make me feel at home and full of gratitude. I am indebted to Prof. Lu for all the great opportunities and lessons I learned from him.

Besides my advisor, I would like to thank the rest of my doctoral committee members, Prof. Dante A. Simonetti, Prof. Vasilios Manousiouthakis, and Prof. Ximin He for their support of my doctor candidacy. Their insightful comments and encouragement helped me to widen my research from various perspectives. The classes I took from Prof. Dante A. Simonetti and Prof. Vasilios Manousiouthakis were very useful during my research experiments.

I would also like to thank my undergraduate research advisor, Prof. Shuhong Yu and Dr. Lifeng Chen. My undergraduate research enabled me to experience the entire process of how to appropriately manage and develop a research project, which also helped my Ph.D. journey. As a novice researcher, I learned a lot from Dr. Lifeng Chen, who bring me to the field of lithium-ion batteries and together we accomplished my first academic publication at University of Science and Technology of China. Big congratulation to Prof. Shuhong Yu selected as an academician of Chinese Academy of Sciences. I also greatly appreciate the help from my classmates Yue Feng, Ziyang Jia, Zhengyan Lun, Shu Lu and Dr. Liang Xu, Dr. Qingfang Guan from Prof. Yu's group. Wish you all the best.

To my dear Lu group members and friends at UCLA, you are like family to me during my four years graduate study. I would like to thank Dr. Li Shen, who has been dedicated much time teaching and helping me in all aspects of my journey here. During my dark time of research progress, it is you encouraged me that no research road is easy and gave me professional suggestion about my research. I deeply appreciate your help and guidance for my graduate study. I wish you all the best in your future career. I would also thank to Dr. Fang Liu, to whom I shadow a lot in my first two years graduate study. I am impressed by your self-discipline on timing and professional scientific literacy. Wish you all the best with Dr. Duo Xu and all the success in your future career as a professor. I would also thank Prof. Haobin Wu, who helped me a lot with my research, especially when I first started my own project. I am impressive of your leadership skills and learned a lot from your scientific mind and understanding. I also thank Dr. Jianqiang Shen for teaching me lots of knowledge in MOF area. I would further thank Dr. Zaiyuan Le, Dr. Xianyang Li, Dr. Haiping Wu, Dr. Runwei Mo, Dr. Seung-Ho Choi, Dr. Gurong Shen, Dr. Gen Chen, Dr. Guoqiang Tan, Prof. Bin Xu, Prof. Huijuan Yue and Prof. Dong Zhang for your research advices

and coaching. Wish you all the best in your future career. I also want to thank Dejia Kong, Chen Zhang, Ran Tao, Xinru Li, Wenyue Shi, Jesse Baucom, Pengcheng Xu, Xing Lu, Fan Li, Xinyi Tan, Jinhui Xu, Alexis Fortini, Zheng Cao and all the other members in Lu group. With you everyone, I learned and enjoyed the journey together in the class and lab.

Besides, I also enjoyed the beautiful campus of UCLA and the delicious foods in dining halls. Thank you for providing such good environment and facilities, UCLA campus.

Last but not the least, I would like to thank my parents for supporting me spiritually throughout my Ph.D. study and my life in general. I am very proud of my parents, who always work so hard to give me a better life. I will not let you down and I will carry on your love with me. I hope that I can return you a more relaxing life in short future. I would also thank to my family members, who care and support me all the time. This dissertation is dedicated to my family.

Thank you for all the people who have helped me during my Ph.D. journey, I would carry on and devote myself in the future.

VITA

2012-2016   B.S., Department of Material and Engineering

University of Science and Technology of China, China

2016-2020   Teaching Assistant, Graduate Researcher

Department of Chemical and Biomolecular Engineering

University of California, Los Angeles, USA

PUBLICATIONS

1. **S. Ma.**[†]; L. Shen.[†]; W. Shi.; C. Zhang.; F. Liu.; J. Baucom.; D. Zhang.; H. Yue.; Y. Lu.*, A Class of Solid-like Electrolytes for Rechargeable Batteries Based on Metal-Organic Frameworks Infiltrated with Liquid Electrolytes. Manuscript in preparation.

2. L. Shen.; H. Wu; F. Liu.; C. Zhang.; **S. Ma.**; Z. Le.; Y. Lu.*, Anchoring anions with metal-organic framework-functionalized separators for advanced lithium batteries. **Nanoscale Horizons** 2019, 4 (3), 705-711.

3. C. Zhang.; L. Shen.; J. Shen.; F. Liu.; G. Chen.; R. Tao.; **S. Ma.**; Y. Peng.; Y. Lu.*, Anion-Sorbent Composite Separators for High-Rate Lithium-Ion Batteries. **Advanced Materials** 2019, 31 (21), 1808338.

4. L. Chen.[†]; **S. Ma.**[†]; S. Lu.; Y. Feng.; J. Zhang.; S. Xin.; S. Yu.*, Biotemplated synthesis of three-dimensional porous MnO/C-N nanocomposites from renewable rapeseed pollen: An anode material for lithium-ion batteries. **Nano Research** 2017, 10 (1), 1-11.

INTRODUCTION

1.1 Energy Storage and conversion

Energy storage (supercapacitors, batteries, etc.) and conversion (fuel cells, solar cells, etc.) are key technologies in modern society. It has been estimated that the worldwide demand for energy will double by 2050 and triple by 2100.[1] With decreasing of the reserves of fossil-fuel-type energy sources and urgent consumption of energy, it is generally acknowledged that a technical revolution for clean and regenerative energy is indispensable to ensure the world's sustainable development. Therefore, energy storage and conversion has attracted much attention and intensive research interests.[2]

Portable energy storage devices are prevalent in our daily lives, from cell phones and laptops, to power source in electric vehicles (EVs) and hybrid electric vehicles (HEVs). Among various energy storage devices, capacitors, fuel cells and batteries are both promising technologies for high-power, high-energy storage, but for different purposes.[3]

As shown in the Ragone plot (**Figure 1.1**), electric capacitor can deliver energy very rapidly, but only in small amounts. This property comes from traditional capacitors store energy through electrostatic charging at their electrode-electrolyte interfaces under an applied voltage. For capacitors, it is crucial to increase specific energy but remains a limitation restraining them from applying into large-scale energy storage systems.[4] By comparison, fuel cells hold the largest energy density so far because the fuel are converted into electricity by oxidizing agent processes. However, they are hindered by the lack of breakthroughs in the fuel storage materials and the high cost for further development and commercialization.[5]

1
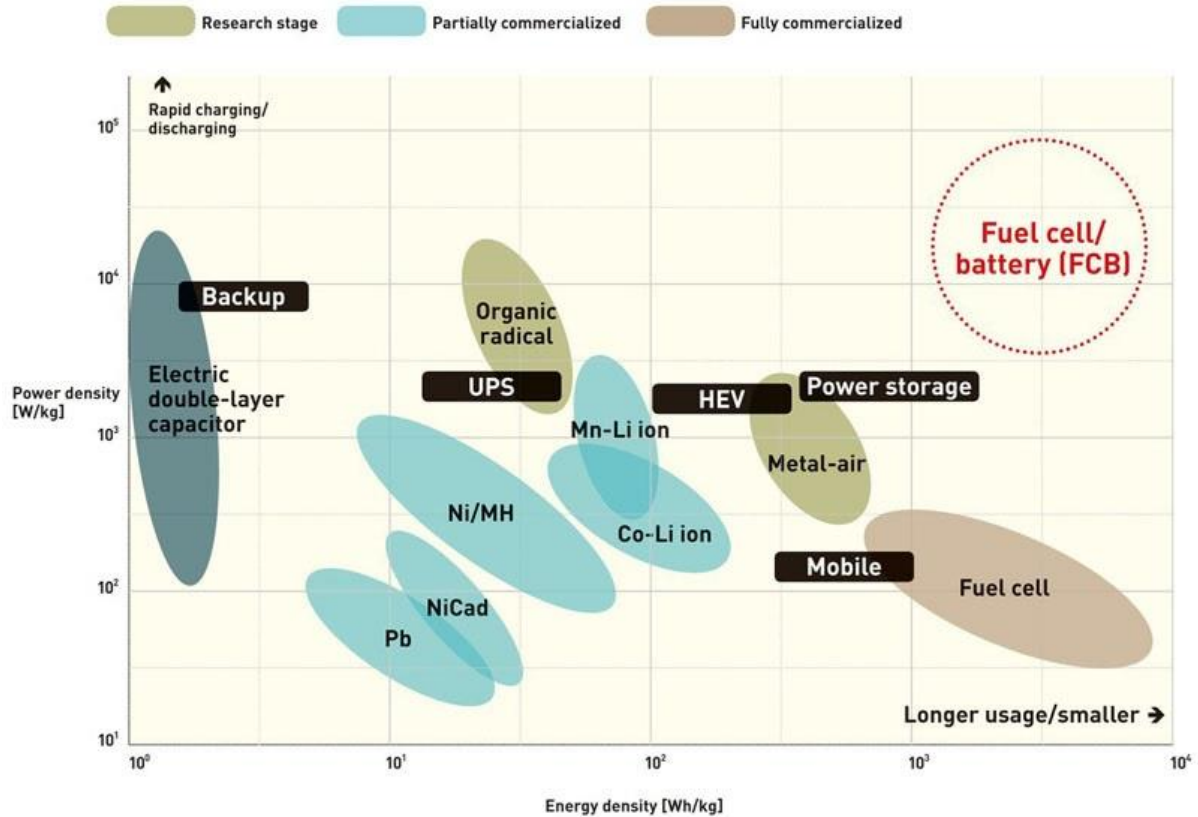
Figure 1.1 Ragone plot comparing the performance of various energy storage devices (power density *vs.* energy density).[6]

In contrast, batteries store energy through electrochemical reactions that typically occur throughout the entire bulk of their electrode active materials, thereby allowing comparatively large amounts of energy to be stored. Research on energy storage generally focus on improving the performance of devices closer to the upper right corner of the Ragone plot. For batteries, there has been increasing demand for higher energy density and lower cost than current state-of-the-art Li-ion batteries. In particular, high energy density lithium-ion batteries are considered as ideal power source for EVs and HEVs. As shown in **Figure 1.2**, the demand for Li-ion batteries increases rapidly, especially with the demand from electric vehicles.
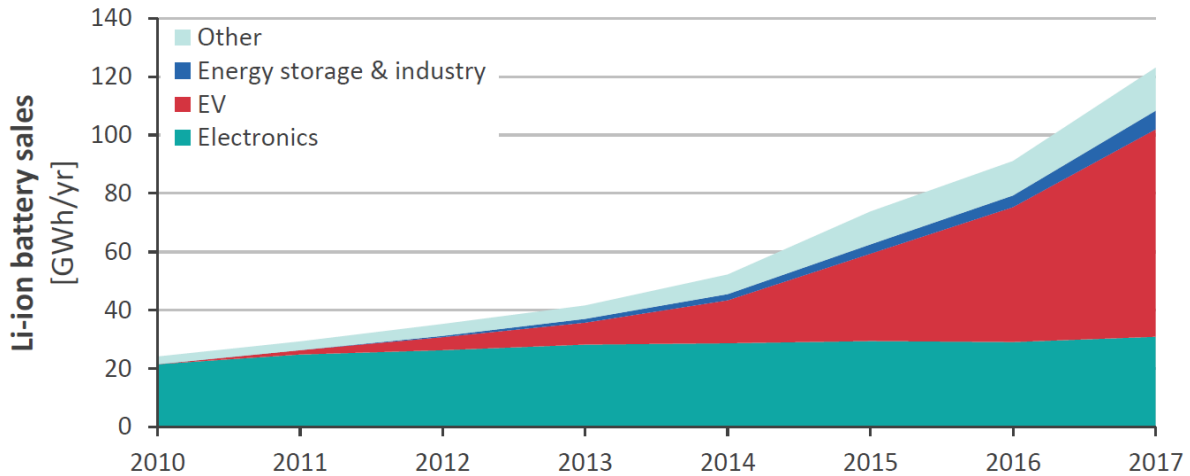
Figure 1.2 Global historical annual growth Li-ion batteries in main market segments.[7] Note: GWh = gigawatt hours, data include sales and stock. Electronics includes mainly portable electronics, EV include Battery Electric Vehicles (BEV), Plug-in Hybrid EVs (PHEV) and electric buses, Energy storage & industry includes stationary storage, uninterruptible power supply (UPS), telecom, and applications in industry, Other includes medical devices, power tools, electric bikes and gardening tools.

However, basic commercial Li-ion batteries using graphite anodes offer EVs a range of around 160 km per charge as approaching its top performance.[8] The development of battery energy density has seriously lagged behind the demand growth of Li-ion batteries. Thus, high energy density electrode materials are extremely demanded in next-generation cutting-edge electronic devices. Another important aspect of Li-ion batteries is related to battery safety because such batteries generally employ flammable liquid electrolytes. In general, current state-of-the-art Li-ion batteries encounter a dilemma in pursuit of high-energy density and enhancement of battery safety.

1.2 Lithium-ion Batteries

1.2.1 Basic of Li-ion Batteries

The lithium-ion battery technology was commercialized by Sony Corporation about 30 years ago, which is based on the use of Li-intercalation properties. Typically, a basic Li-ion cell consists of the cathode (positive electrode) and the anode (negative electrode) for the redox reaction; the electrolytes for ion conduction and the separator allowing the exchange of lithium ions between the two electrodes but not electrons. As shown in **Figure 1.3**, the anode material is a graphic carbon and the cathode material usually composed of layered transition metal oxides $LiMO_2$ (M = Co, Ni).[9] Both electrodes allow reversible intercalation of Li ions from their respective structure. As a result, the 2019 Nobel Prize in Chemistry was awarded to John Goodenough, M. Stanley Whittingham and Akira Yoshino for the development of lithium-ion batteries.[10]
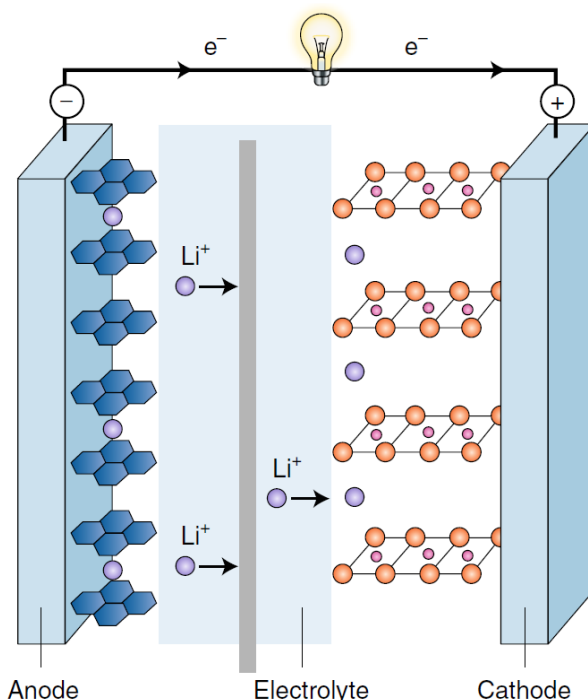
Figure 1.3 Schematic of a rechargeable lithium-ion battery.[11]

1.2.2 Parameters of Rechargeable Batteries

Electrical energy is stored as chemical energy in the electrodes of a rechargeable battery. The output of a battery on discharge is a current $I = \mathrm{d}q/\mathrm{d}t$ at a voltage V for a time Δt corresponding to a stored energy:

$$\int_0^{\Delta t} IV(t)\mathrm{d}t = \int_0^Q V1(q)\mathrm{d}q \qquad (1.1)$$

where the total charge stored is the battery capacity Q.

$$Q = \int_0^{\Delta t} I\mathrm{d}t = \int_0^Q \mathrm{d}q \qquad (1.2)$$

For portable batteries, specific or volumetric capacity (mAh g^{-1}) and energy density (Wh kg^{-1}) are critical parameters. Battery life indicates the cycle life, defined as the number of charge/recharge cycles before the capacity fades to 80 % of its initial values, i.e., $Q/Q_{\mathrm{In}} = 0.8$.[12]
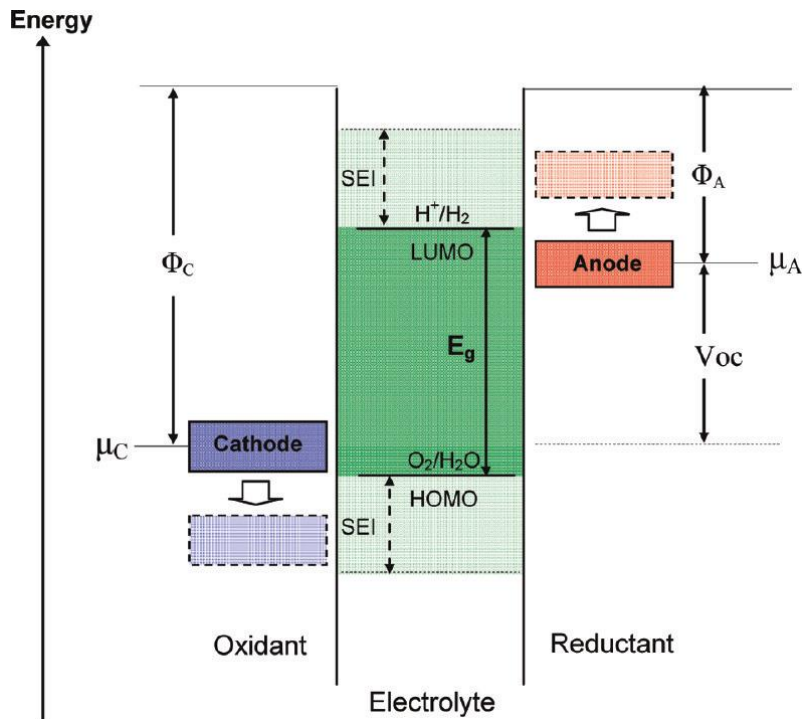
Figure 1.4 Schematic open-circuit energy diagram for a typical battery cell. E$_g$ is the thermodynamic stability window of the electrolyte.[13]

The cell voltage is related to whole cell system, including cathode, anode and electrolyte. **Figure 1.4** illustrate the relative electron energies in the electrodes and the electrolyte within a thermodynamic stable battery cell. Typically, during discharge process, the cathode is the oxidant and the anode is the reductant. The energy separation E_g between the lowest unoccupied molecular orbital (LUMO) and the highest occupied molecular orbital (HOMO) of the electrolyte indicates the thermodynamic stability window of the electrolyte.[13] The electrochemical potentials of cathode and anode are represented as μ_C and μ_A. Thus, the open-circuit voltage of a battery cell is given by the following equation:

$$V_{OC} = \frac{\mu_A - \mu_C}{e} \tag{1.3}$$

where e is the magnitude of the electron charge.

If $\mu_A > E_{LUMO}$, electrons on the anode are inclined to transfer to the unoccupied orbital of the electrolyte, inducing the intrinsic reduction reactions of the electrolyte unless a passivation layer blocks the electron transfer. Similarly, a cathode with $\mu_C < E_{HOMO}$ will oxidize the electrolyte unless the passivation layer creates a barrier to electron transfer. Such passivation layer called as solid electrolyte interphase (SEI), which can effectively block the electron transfer while only allow ions to go through, avoid further decomposition of organic electrolyte.[14] In the meantime, SEI layer formed at the electrode/electrolyte boundary can give a kinetic stability to a larger V_{OC}. For example, the lead acid cell has an acidic electrolyte (H_2SO_4) and a $V_{OC} \approx 2.0$ V, which is much higher than the thermodynamic voltage limit of water electrolysis (1.23 V).[15]

1.2.3 Development of Li-ion Batteries

The past decade has witnessed a growing trend towards next-generation lithium-ion batteries with higher specific capacity/energy density. As lithium-ion batteries are approaching the theoretical capacity of both cathode/anode materials, especially graphite anode. For pursing next-generation higher energy density rechargeable batteries, many approaches are recently being explored, including the development of high-energy electrode materials such as silicon anodes[16] and high capacity Li-rich cathodes[17], and novel high-energy battery technologies, such as lithium-sulfur[18-19], lithium-air[19-20], lithium-metal[21], magnesium-air[22-23], aluminum-air batteries[24] and all-solid-state batteries.[25-26] As shown in **Figure 1.5**, the historical evolution and advances of Li-ion batteries serve as a guideline for the future direction of next-generation Li-ion batteries.
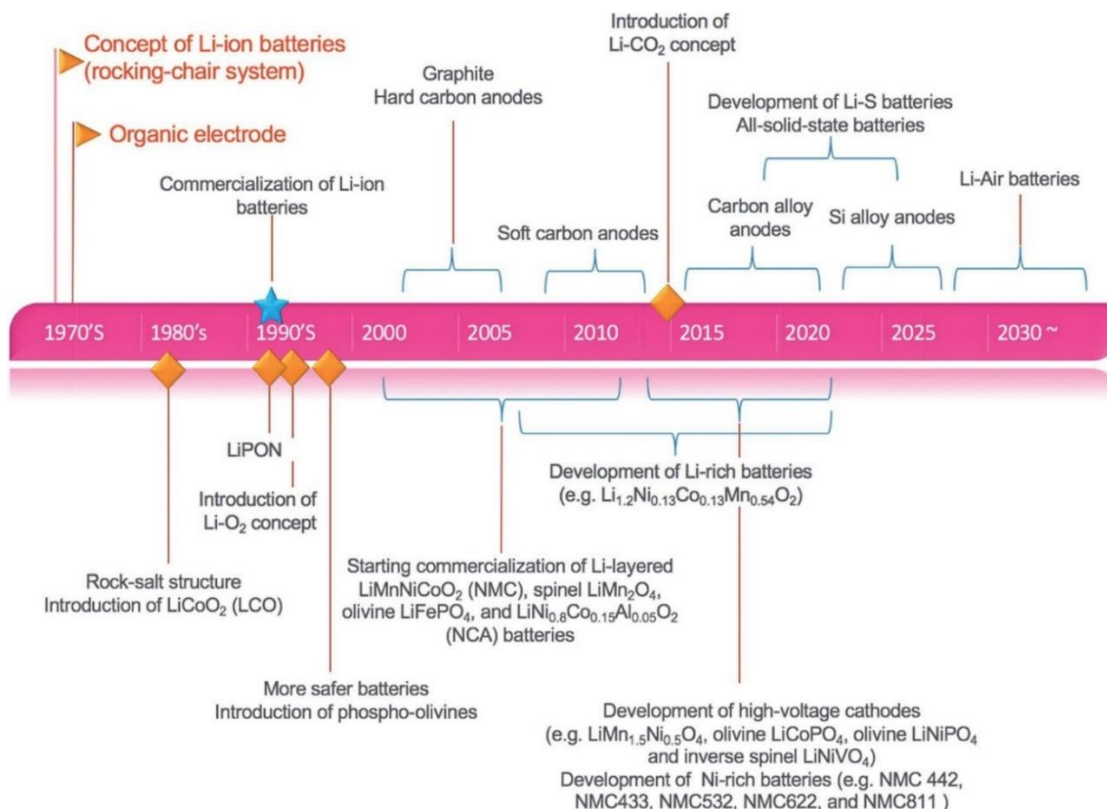
Figure 1.5 Historical evolution and advances of lithium-ion battery technologies.[27]

1.3 Beyond Li-ion Batteries

1.3.1 Lithium Metal Batteries

From **Figure 1.6**, we can clearly notice the unprecedented characteristics of lithium metal, that is, its high theoretical specific capacity (3,861 mAh g^{-1} vs. 372 mAh g^{-1} for conventional graphite anode), light weight (0.53 g cm^{-3}), and lowest electrochemical potential (-3.04 V vs. standard hydrogen electrode (SHE)), for the implementation of high-specific-energy Li-metal-based batteries.[28]
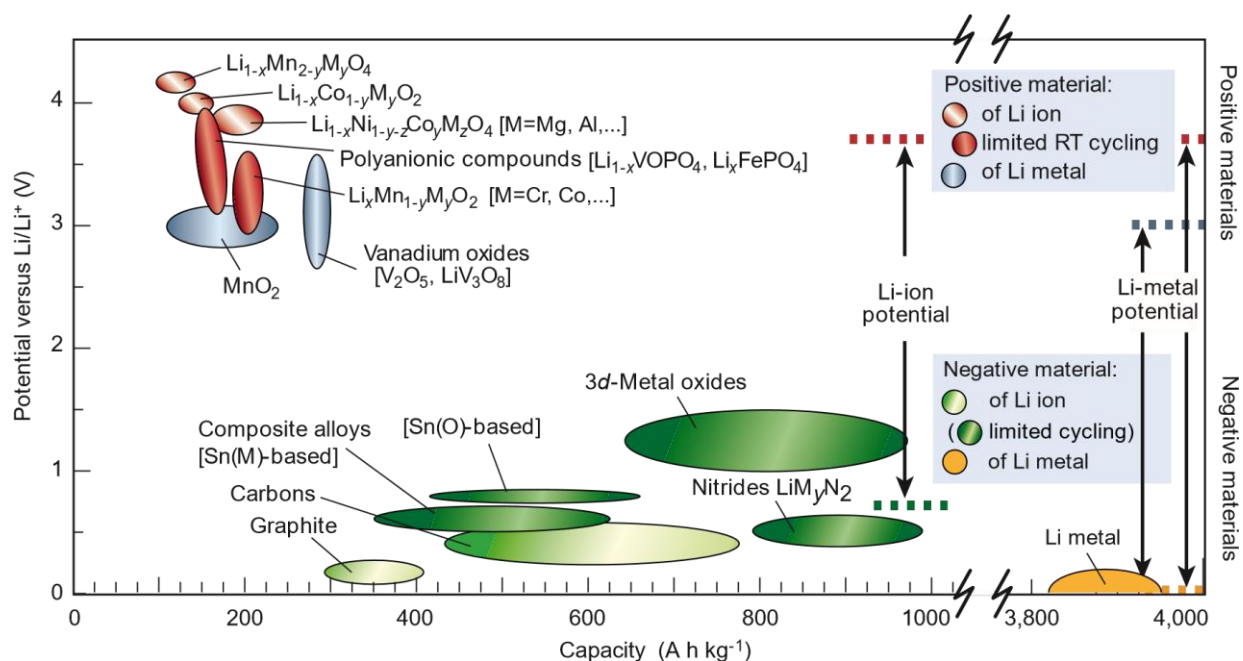
Figure 1.6 Voltage versus capacity for positive- and negative-electrode materials presently used or under serious considerations for the next generation of rechargeable Li-based cells.[29]

It is generally accepted to calculate the specific theoretical capacity (Q_c) based on the Li metal, and the high value of 3,861 mAh g^{-1} is obtained as below:

$$Li - e^- \leftrightarrow Li^+ \tag{1.4}$$
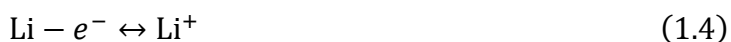
$$Q_c = \frac{\text{Charge}}{\text{Mass}} = \frac{6.02 \times 10^{23} \text{ atom } (1.6 \times 10^{-19} \frac{C}{\text{atom}}) \frac{1 \text{ mAh}}{3.6 \text{ C}}}{1 \text{ mol } \frac{6.94 \text{ g}}{\text{mol}}}$$

$$= 3{,}861 \text{ mAh g}^{-1} \tag{1.5}$$

The lithium metal battery is considered to be one of the most promising candidates for next generation high-energy-density electrochemical energy storage devices.[14] However, as a "hostless" anode, there are two main barriers. One is the uncontrolled dendrite formation during repeated charge/discharge processes, and another is the virtually relative infinity volume change during long-term cycling. These two barriers consequently lead two critical problems for Li anodes – one is severe safety hazards and catastrophic failure because of potential short circuits caused by sharp Li filaments piercing through the separator; another is low Coulombic efficiency (CE) and short cycle life (**Figure 1.7**).[30]
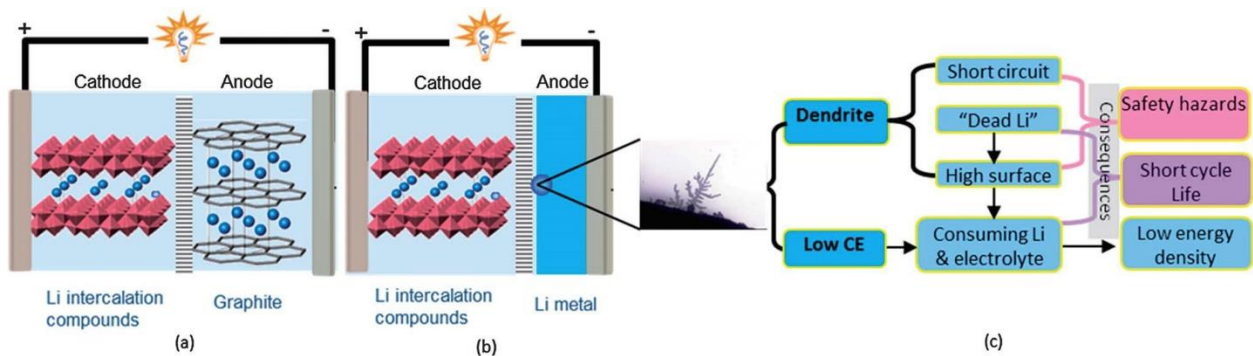
Figure 1.7 Schematic diagram of (a) Li ion batteries; (b) Li metal batteries; (c) the typical morphology of Li dendrite and the main problems related to dendrites and low coulombic efficiency.[30]

Even though various strategies have been explored to stabilize Li-metal anodes, such as artificial solid electrolyte interphase (SEI) to block Li dendrite growth[31], coating Li-metal anodes with

polymers[32], ceramics[33], using halogenated salts or alkaline-metal salts as electrolyte additive[34-35], the challenges remain unsolved. Because these approaches do not change the fundamental, self-amplifying behavior of the dendrite growth. In this case, solid electrolytes are believed to be able to suppress Li dendrite growth because of their high mechanical strength and high Li^+ transference number.[26, 36]

1.1.3 Rechargeable Metal Batteries

Parallel to lithium metal batteries, rechargeable batteries based on sodium, potassium, magnesium, and aluminum have also attracted great interest due to their abundance, safety and low cost.[37-39] **Figure 1.8** compares the earth crust abundance and energy density among different metal anodes in electrochemical storage systems, which shows much higher abundance of sodium, potassium, magnesium and aluminum compared with lithium. Thus, these materials are expected to lower the cost and satisfy the demand for large-scale energy storage applications.
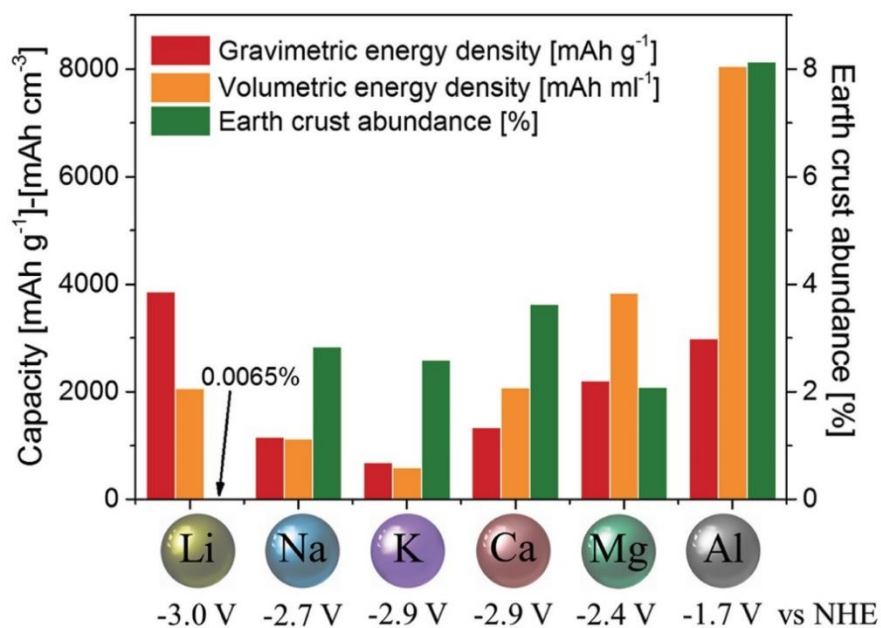
Figure 1.8 Comparison between gravimetric and volumetric capacities, standard reduction potential and heart crust abundance of metal anodes used or proposed for application in electrochemical storage systems.[40]

Sodium-ion batteries are considered most practical candidate power source due to the high availability and similar chemistry to that of lithium-ion.[41] However, sodium based batteries still encounter several challenges such as slow kinetics and unstable cyclability,[42] and its high standard reduction potential (–2.71 V vs. SHE) strongly limit the energy density of sodium-ion batteries.[43] Potassium has lower standard reduction potential (–2.93 V vs. SHE), which allows potassium-ion batteries to operate at higher potentials compared with sodium-ion batteries. Nevertheless, low ion diffusivity in solid electrodes/poor K^+ reaction kinetics and high reactivity of potassium metal still hinder the future development of potassium-ion batteries.[44] Besides the alkali metals, secondary multivalent ion batteries such as bivalent magnesium and trivalent aluminum are of great interest.[40] Theoretically, the use of multivalent ion increase the number of electrons exchanged during electrochemical process, which lead to high volumetric capacity values. However, the major issues in the development of multivalent batteries include the discovery of both high-voltage cathodes and high compatibility electrolytes.[45]

1.1.4 Lithium Sulfur Batteries

Lithium-sulfur (Li-S) battery is a promising energy-storage technology due to their high theoretical specific capacity (1675 mAh g^{-1}), high energy density (2600 Wh kg^{-1}), natural abundance and environmental friendliness.[46-47] However, the major issue preventing the practical applications of lithium-sulfur batteries is the "shuttle effect" caused by dissolution of the discharge/charge intermediates (that is, a series of lithium polysulfides, LiPSs) in organic

electrolytes (**Figure 1.9**). The undesired shuttle effect leads to the capacity loss of the sulfur cathode, low charge-discharge efficiency and precipitation of insoluble/insulating Li_2S_2/Li_2S on lithium metal anode, causing the loss of energy-bearing materials. The batteries rely on the reversible reaction:

$$2\,Li^+ + 2\,e^- + x\,S \underset{\text{Charge}}{\overset{\text{Discharge}}{\rightleftharpoons}} Li_2S_x \quad 1 < x < 8 \tag{1.6}$$
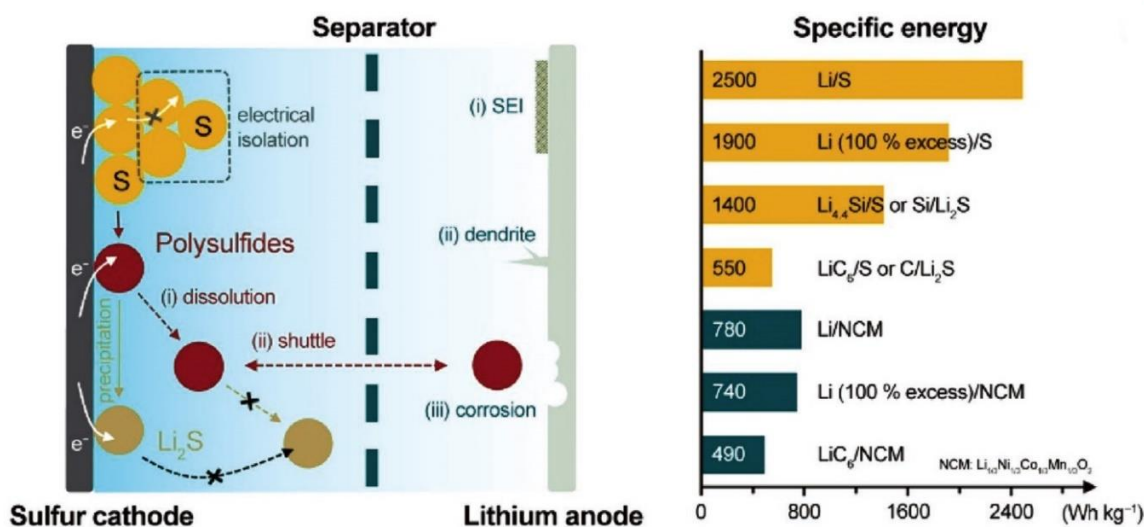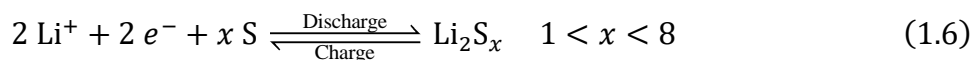
Figure 1.9 Schematic of a typical Li–S battery and specific energies of various rechargeable battery systems.[47]

In early stages, the main approach is to infiltrate molten sulfur into porous conductive carbon materials, resulting in interconnected conducting networks and enhanced physical entrapment of the LiPSs. For instance, hosts included meso- and microporous carbons, carbon nanotubes and fibres, graphene, etc. There are two fundamental problems within this approach. Firstly, simple physical (spatial) entrapment is not sufficient to prevent diffusion and shuttling of LiPSs during long-term cycling. This results in loss of active materials, accumulation of insulating layers on the anode and capacity fading. The second problem is the large electrolyte volume/sulfur ratio required

to wet the large volume of porous carbon and to solubilize the LiPSs, which greatly reduces the volumetric energy density of Li-S batteries.[48]

Another type of high surface area hosts, metal organic frameworks (MOFs) attracted much attention due to their ability to combine physical encapsulation within the MOF pores with strong chemical anchoring to the MOF. Ideally, such a MOF support would constrain both redox end members (S and Li_2S) and all PS intermediates present during operation of a Li-S cell. In this case, MOFs can maximize the utilization of active material and there is no need for any S-containing species to migrate into or out of the MOF pores, assuming these species remain accessible to Li^+ and electrons.[49] However, the use of MOF-based materials in a cathode as a porous host to contain sulfur may be an unsuitable choice because of the insulating nature of MOF-based materials.
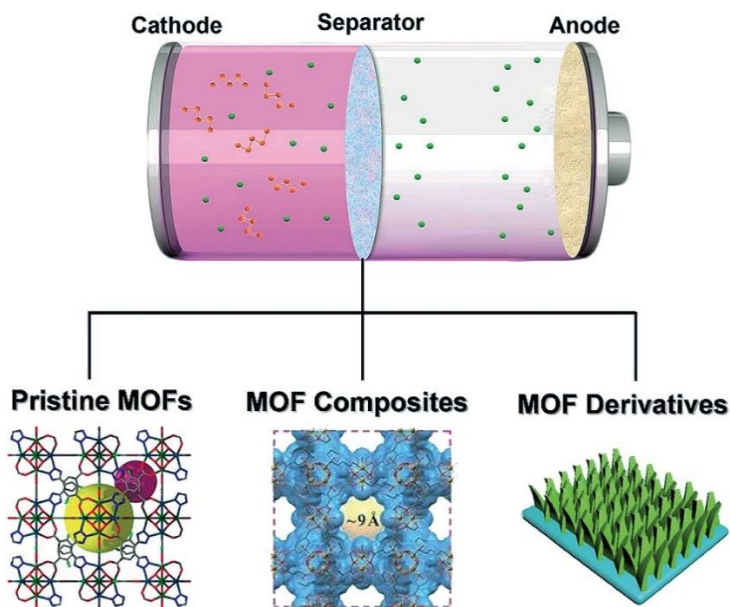
Figure 1.10 Schematic illustration of employing pristine MOFs, MOF composites and MOF derivatives as separators in Li–S battery.[50]

Recently, a useful approach to address the shuttle effect is to determine a method to block the shuttle pathway of polysulfides. In this case, MOF-based materials with large surface area and

highly ordered pores with tunable porosity would be appropriate candidates as separators in Li-S battery (**Figure 1.10**). However, not every type of MOF is suitable for specific function. For example, HKUST-1, a Cu-based MOF, has poor performance as separator in Li-S battery due to the reaction between Cu^{2+} and lithium or sulfur.[51] Similar limitation should be determined, and studies in this research direction still require more attention and efforts.

1.1.5 Advantages of solid electrolytes

One of the severe limitations for high-energy batteries is the flammable organic-liquid electrolyte as the safety hazard. In this case, adapting solid electrolytes are considered an ultimate solution to address the safety concerns,[52] mitigate the growth of metal dendrites, and promote the adaption of metal batteries with high energy density.[53] **Figure 1.11** schematically shows the lithium-ion battery and solid-state batteries with different cathodes. Clearly, the volume advantage of solid-state batteries allows greatly increasement of volumetric energy density of the cell. Such solid-state batteries using lithium metal will lead to EVs with a range of more than 350 km per charge.[54] There are many advantages of solid electrolytes in in terms of device fabrication (facile shaping, patterning and integration), stability (non-volatile), safety (non-explosive) and excellent electrochemical properties (high conductivity and wide potential window).[55]
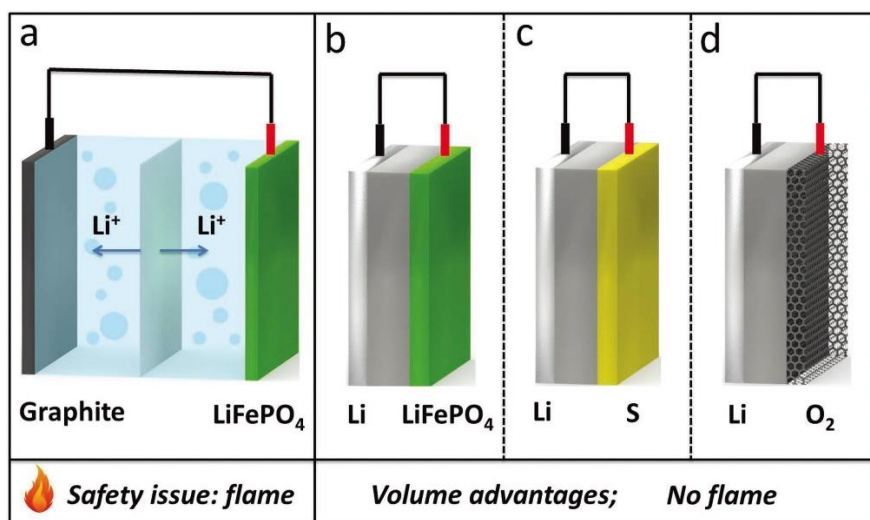
Figure 1.11 Schematic illustration of a) a conventional lithium-ion battery with LiFePO$_4$ (LFP) cathode, graphite anode, and liquid electrolyte; b-d) solid-state batteries with LFP, sulfur, or oxygen cathodes, Li-metal anode, and solid-state electrolyte membrane.[25]

1.4 Current state-of-the-art of solid electrolytes

1.4.1 Historical outline of solid electrolytes

The history of solid-state ionic conductors can be traced back to as early as the 1830s, when Faraday discovered the outstanding property of conduction in heated solid Ag$_2$S and PbF$_2$.[56] However, it is generally believed that the 1960s are considered starting point for high-conductivity solid-state electrolytes when a fast 2D sodium-ion-transport phenomenon was discovered in β-alumina (Na$_2$O·11Al$_2$O$_3$), which was applied in high temperature Na-S batteries[57] (see **Figure 1.12** for a timeline of developments). In the 1980s, β-alumina was used in another type of high temperature system, the Na/MeCl$_2$ batteries (also called ZEBRA cell). Attempts to use solid-state polymer electrolytes in lithium-based batteries began in the 1980s after the discovery of lithium-ion conduction in a PEO-based system.[58] Inorganic solid-state electrolytes have also been used in lithium-ion batteries since the 1990s, after a lithium phosphorus oxynitride (LiPON) material

15

was fabricated as a thin film by Oak Ridge National Laboratory.[59] Considerable research has focused on the development of inorganic lithium-ion conductive ceramic materials, such as LISICON-like (lithium superionic conductor), garnets-type, sulfide-type, NASICON-like (sodium superionic conductor), lithium nitrides, lithium hydrides, perovskites, and lithium halides.[60] From the 2000s, solid electrolytes have been used in emerging lithium batteries with gaseous or liquid cathodes, such lithium-air batteries, lithium-sulfur batteries and lithium-bromine batteries.[61] Most recently, a unique "mediator-ion" battery concept has been proposed for high-energy, low-cost aqueous batteries with solid electrolytes.[62]
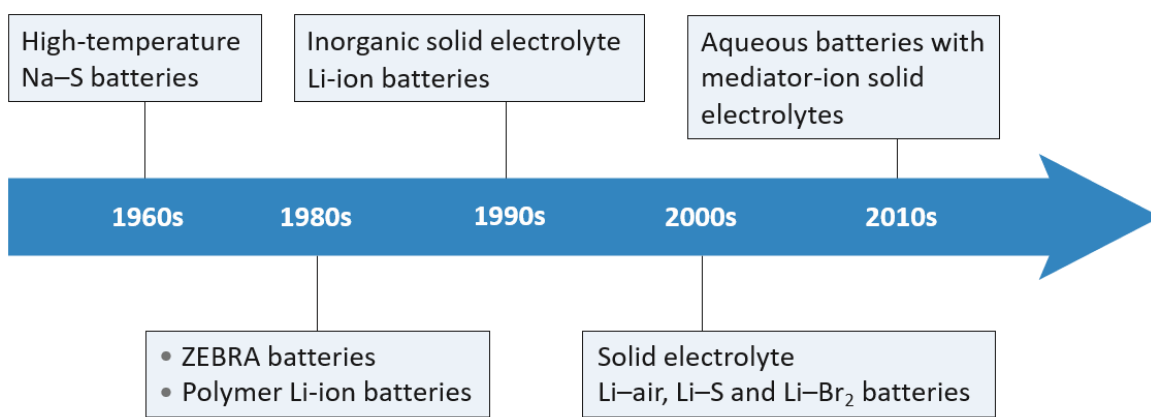
Figure 1.12 A historical outline of the development of solid-state electrolyte.[61]

1.4.2 Summary of common electrolyte systems and their properties

Ionic conductivity is a pivotal property for solid electrolytes. However, for practical application in electrochemical energy storage and conversion systems, other properties are also important. The main properties required for solid-state electrolytes are: high ionic conductivity, low ionic area-specific resistance, a wide electrochemical stability window, good interfacial compatibility, good thermal stability, high mechanical strength, low materials and processing cost, easy device integration and environmental friendliness.[61, 63-64] As we mentioned before, much progress has

16

been made to fabricate improved both inorganic and organic (polymer) solid-electrolyte materials.

Figure 1.13 gives a summary of common electrolyte systems for liquid, ceramic, solid polymer, and quasi solid-state (solid-like) electrolytes.
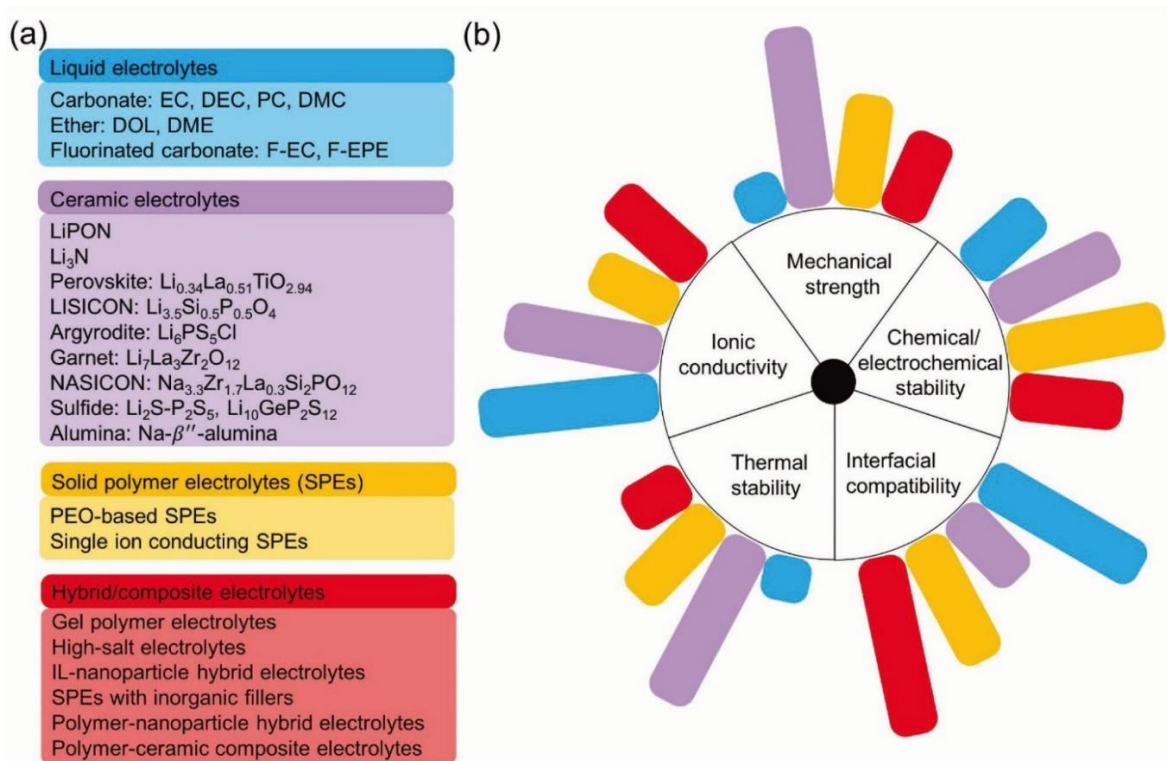
Figure 1.13 (a) Summarization of common electrolyte systems for liquid, ceramic, solid polymer, and quasi solid-state electrolytes. (b) Different physical and electrochemical characteristics of liquid, ceramic, solid polymer, and hybrid/composite electrolytes.[65]

As we can see from above, each electrolyte system has its advantages and disadvantages. For example, liquid electrolytes hold high ionic conductivity but usually suffer from poor thermal stability, mechanical strength and narrow electrochemical stability window.[66] Ceramic materials exhibit high chemical stability and high mechanical strength. However, they are non-flexible and expensive to develop large-scale production. While for solid polymer electrolytes (SPEs), PEO-based SPEs are stable with lithium metal and less difficult to be integrated but has limited thermal

stability and their conductivity remains low at ambient temperature (e.g., $< 10^{-5}$ S cm^{-1}).[67] Hybrid/composite electrolytes, also called as solid-like electrolytes, which are generally made by encapsulating liquid electrolytes within solid porous scaffolds, represent another direction with the merits of both liquid electrolyte and solid electrolyte.[68-70] For examples, solid-like electrolytes based on hollow SiO_2 and Al_2O_3 spheres could provide ambient ionic conductivities over 10^{-3} S cm^{-1}.[68, 71-73] Over the years, researchers have explored many other materials. Metal-organic frameworks (MOFs), or porous coordination polymers (PCPs) are a class of compounds which consist of metal clusters or nodes linked by organic moieties. MOFs are highly crystalline and electrical insulators, are compatible with a wide range of mobile cations, and present regular pore networks that allow, in principle, swift ion movement.[74]

1.4.3 Ion-transport mechanisms and properties

1.4.3.1 Ion-transport mechanisms

Ionic conduction is a phenomenon of charged of charged particles, similar to electronic conduction, and can be defined as follows:

$$\sigma = nZe\eta \tag{1.7}$$

where σ: conductivity; n: carrier concentration; Ze: charge of the conducting carrier; and $Z=1$ when the carrier is a lithium ion; η: mobility.

From thermodynamic theory, the mobility and the self-diffusion coefficient can be related as follows:

$$\eta = \frac{ZeD}{k\mathrm{T}} \tag{1.8}$$

Where D: self-diffusion coefficient; k: Boltzmann constant; T: temperature.

The ion-conduction mechanisms in solid-state conductors are significantly different from those in liquid electrolytes. In solution, the diffusion of ions is limited by the friction of the conducting material. It is described by the famous Stokes-Einstein equation, applying a friction coefficient.[67] Due to reasonably fast exchange between the solvating molecules and uniform surroundings, the potential energy profile of mobile lithium ions in aprotic electrolytes can be considered horizontal (**Figure 1.14**, right). In contrast, the diffusion of mobile species in a crystalline solid need to pass through periodic bottleneck points, which define an energetic barrier that separates the two local minima (typically crystallographic sites for lithium) along the minimum energy pathway (**Figure 1.14**, left). This energy barrier is generally referred as migration or motional energy, E_m, which greatly influences ionic mobility and ionic conductivity.[60]
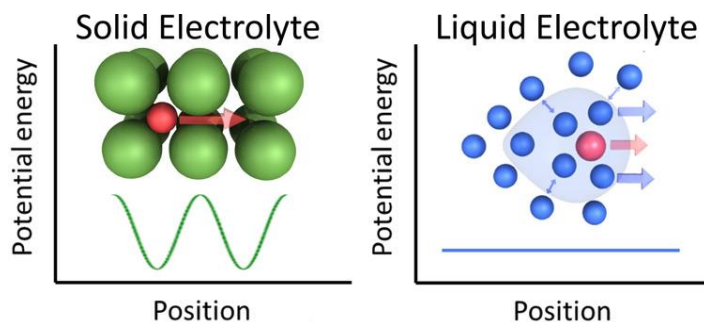
Figure 1.14 Potential energy of a mobile ion migration in solid electrolyte and liquid electrolyte.[60] Left and right show the potential energy of migration in a crystalline solid of an interstitial mobile ion and a charged species in red with a solvation shell of electrolyte molecules (highlighted in blue) in liquid electrolytes, respectively.

Diffusion of a conducting carrier is frozen in porous materials, and in this case, the diffusion constant is described by applying the random-walk model, with hopping frequency f and one-step distance d:

$$D = \frac{fd^2}{6} \tag{1.9}$$

It should be noted that the factor 1/6 arises from three-dimensional unity and can be changed by the dimensions of the conduction mechanism. Given that the hopping frequency depends on the activation energy (E_a), the conductivity is described by the following equation:

$$\sigma = \frac{n(Ze)^2 d^2}{6kT} f_0 \exp\left(-\frac{E_a}{kT}\right)$$

$$= \frac{\sigma_0}{T} exp\left(-\frac{E_a}{kT}\right) \tag{1.10}$$

where E_a is the activation energy of diffusion.

The ionic conductivity of crystalline solids is also dependent on the amount of interstitials, vacancies and partial occupancy on lattice sites or interstices, which is determined by the ionic energy gap or defect formation energy (E_f) in stoichiometric ion conductors (known as the intrinsic regime). In addition, interstitials and vacancies can be created by substitution of aliovalent cations, whose formation energetics is governed by the trapping energy, E_t (known as extrinsic regime). In both intrinsic and extrinsic regimes, the apparent activation energy E_a of ion conductivity contains contributions from both the defect formation energy E_f or E_t and the migration energy E_m.[75] E_a is equal to $E_m + E_f/2$ or $E_m + E_t/2$ for temperature-dependent concentrations of mobile lithium ions in intrinsic and substituted lithium-ion conductors, respectively. Plotting the logarithm of the product of conductivity and temperature as a function of the reciprocal of temperature yields apparent activation energy of lithium-ion conduction.

1.4.3.2 Ionic mobility

The properties of the electrolyte are dependent upon the electrolyte solution structure. Propylene carbonate (PC) is one of the primary organic solvents for state-of-the-art lithium ion battery

electrolytes. PC is a stable dipolar aprotic solvent of a moderately high relative permittivity (64.4 at 25 °C), and its structure is shown in **Figure 1.15**. Studies suggest that cations are more solvated in PC than anions due to the distribution of charges in the solvent dipole. The negative end of dipole is localized on the carbonyl oxygen, which is relatively more accessible to the cations, whereas the positive charge is distributed over the atoms in the chain H_3C-CH-CH_2. Thus, cations are more solvated than anions in PC.[76]

Propylene Carbonate (PC)   Dimethyl Sulfoxide (DMSO)
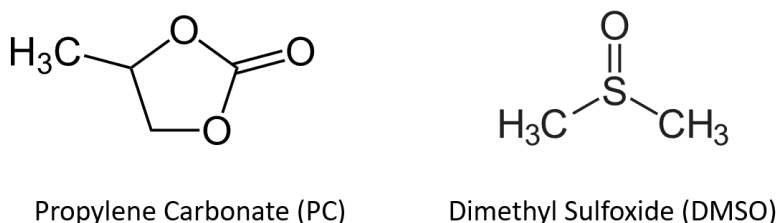
Figure 1.15 Chemical structure of Propylene Carbonate (Left) and Dimethyl Sulfoxide (Right).

Dimethyl sulfoxide (DMSO) is a dipolar aprotic solvent as shown in **Figure 1.15**. It has similar properties to PC, an intermediate relative permittivity (46.7 at 25 °C) and extensive dissolving power. The negative center of DMSO is located at oxygen atom. The solvent properties of PC and DMSO are compared in Table 1, the similar properties of DMSO with PC enable its application in battery devices.

Table 1 | Summary of solvent properties of PC and DMSO[77-79]

	T_m (°C)	T_b (°C)	ε	ρ/g cm^{-3}	η/mPa s	DN
PC	− 49.2	241.7	64.4	1.199	2.50	15.1
DMSO	18.5	189	46.7	1.095	1.98	29.8

melting temperature T_m, boiling temperature T_b, relative permittivity ε, density ρ, viscosity η, donor number DN

The ionic mobility is known to be determined by several factors. To begin with, (i) ion-solvent interactions, which determine the size of solvated ions in solution and described by Stokes radius (R_s) as the following Stokes' equation:

$$R_s = \frac{Z_i F^2}{6\pi\eta_0\lambda_i^\infty N_A}$$ (1.11)

where Z_i, F, η_0, λ_i^∞, N_A are number of ionic charge, Faraday constant, viscosity, limiting molar ionic conductivity and Avogadro constant, respectively.[80] The limiting molar ionic conductivity can be correlated to the limiting ionic mobility by equation (1.12).

$$\lambda_i^\infty = \mu_i^\infty F$$ (1.12)

At very high intensities of the field of the ions, a long-range ordering effect of the ion on the solvent molecules becomes noticeable. This effect can be applied to the multivalent cations such as Mg^{2+}, Al^{3+} and causes a viscosity increase.[81] (ii) The second factor of the moving ions undergoes ion-dipole interactions with the solvent molecules, resulting in frictional resistance, so-called dielectric friction. (iii) The third factor that may influence the mobility is ion-ion interaction, which reduces the mobility in solutions with finite ionic strength relative to the limiting case at infinite dilution.[82-83] (iv) Reinforcing electrostatic interaction with the counter-ions, which usually found in organic solvents with intermediate or low relative permittivity. Aggregates of ion and counter-ion, formed by ion association (with solvent separated ions) or ion pair formation (with direct contact of the ions), further reduce the mobility and the extend of reduction depends on the degree of formation of the aggregate.[84]

1.4.4 Electrolyte performances measurement

Ionic conductivity (σ, S cm^{-1}) can be measured by electrochemical impedance spectroscopy (EIS) after placing the pellets or membranes between two stainless steel blocking contacts in a

2032-type coin cell. The setup frequency range is from 10^6 to 1 Hz and alternating-current (AC) amplitude is 100 mV. The resistance can be obtained by fitting the Nyquist plot to the model circuit shown in **Figure 1.16**, using the ZView software. The ionic conductivity can be calculated using equation (1.11).

$$\sigma = \frac{L}{R \times S}$$
(1.13)

where σ is ionic conductivity (S cm^{-1}), L is the pellet thickness (cm), S is the pellet area (cm^2) and R is the resistance (Ω) obtained from the measurement.
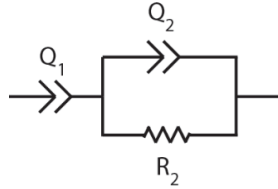
Figure 1.16. The equivalent circuit used for fitting impedance spectra. R_2 is a resistor and Q_1 and Q_2 are constant phase elements which are imperfect capacitors.

To calculate **activation energies** (E_a, eV), the impedances could be measured in a hydrothermal oven at various temperatures (T, K). Conductivity at each temperature can be obtained at equilibrium as indicated by negligible difference from consecutive measurement. Based on the Nernest-Einstein relation (1.10) we mentioned before, the activation energy can be obtained from a plot of $\log(\sigma T)$ against $1/T$. Since $\log T$ does not vary much over a small temperature range, a simpler expression can be used by plotting $\log(\sigma)$ against $1/T$, each linear fitting should be qualified by coefficient of determination R^2 over 0.99.

$$\sigma = \frac{\sigma_0}{T} exp\left(-\frac{E_a}{kT}\right)$$
(1.14)

where σ_0 is a pre-exponential factor, T is the temperature, E_a is the activation energy and k is the Boltzmann constant.[85]

The **transference number** (t) can be measured by combining AC impedance and potentiostatic polarization techniques using symmetric cell, such as Li/electrolyte/Li cell. Usually, AC impedance test (10^6 to 1 Hz, 20 mV amplitude) can be performed to obtain initial resistance (R^0) of the passivating layers. Then a constant small DC voltage (V, 20 mV) signal can be applied to symmetric cell, monitoring its initial current (I^0) till the current reaching a steady state current (I^s), which was followed by another AC impedance test to get steady-state resistance (R^s) of the passivating layers. The lithium-ion transference number can be calculated from equation (6).[86]

$$t_{\mathrm{Li}^+} = \frac{I^s(V\text{-}I^0R^0)}{I^0(V\text{-}I^sR^s)} \tag{1.15}$$

Sodium-ion transference number (t_{Na^+}) was measured using the same approach accordingly. The resistance can be obtained by fitting the Nyquist plot to the model circuit in **Figure 1.17** using ZView software.
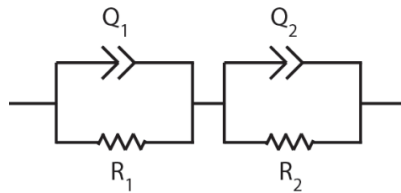
Figure 1.17 The equivalent circuit used for fitting impedance spectra. R1 and R2 are resistors and Q1 and Q2 are constant phase elements which are imperfect capacitors.

1.5 Solid-like electrolytes constructed from metal-organic frameworks (MOFs)

1.5.1 Alternative approach to fabricate solid-like electrolytes

We have mentioned many types of solid lithium ionic conductors, which are attractive due to their inherent advantages in term of safety and device fabrication. However, their ionic conductivities at room temperature are typically more than an order of magnitude below the requirement for normal battery operation. In contrast, organic liquid electrolytes feature very fast ionic transport properties but introduce the obvious flammability of carbonate solvents.[87]

Herein, we have been interested in a strategy to combine the benefits of liquid electrolytes (conduction) with the rigidity of a solid electrolyte. In principle, it is easy to combine the advantages both from solid electrolytes and liquid electrolytes in one material that has a solid-like mechanical modulus for dendrites blocking and liquid-like room-temperature ionic conductivities for Li^+ transport. Many works along this direction have been carried out recently by the Archer group and Goodenough group in which polymer-based nanocomposites are used as the host for the loading of liquid electrolytes, including PVDF-HFP/Al_2O_3, PEO/Al_2O_3, and PVDF-HFP/PVP/Sb_2O_3. [88-90] As expected, these nanocomposites reveal a good mechanical strength to overcome the dendrites problems, providing an alternative approach to fabricate robust solid electrolytes. However, their nanopores are less controllable with relatively dynamic frameworks, which may allow dendrites to pass through causing a short-circuit.[68] Therefore, we are aiming to find a class of solid-like electrolytes with well-defined porous nanoarchitectures.

Here, metal-organic frameworks (MOFs) are excellent platforms for exploring such solid-like electrolytes. They are highly crystalline, electrically insulating, nanoporous with well-defined rigid pores and exhibit high surface area, large pore volume and open pore structure with highly designability. As shown in **Figure 1.18**, MOFs and their derivatives are two developing families

of functional materials for energy storage and conversion. The intrinsically electrical insulating property and the porous structure of MOFs enable a facial electrolyte penetration and ion transportation. The key advantage that MOFs bring to such applications is the possibility of introducing chemically functionalizable pores. For example, metal sites are designable for strong Lewis acid-base interaction and ligand functionality are controllable, thereby combing intended chemical and physical properties to the materials.[91-92]
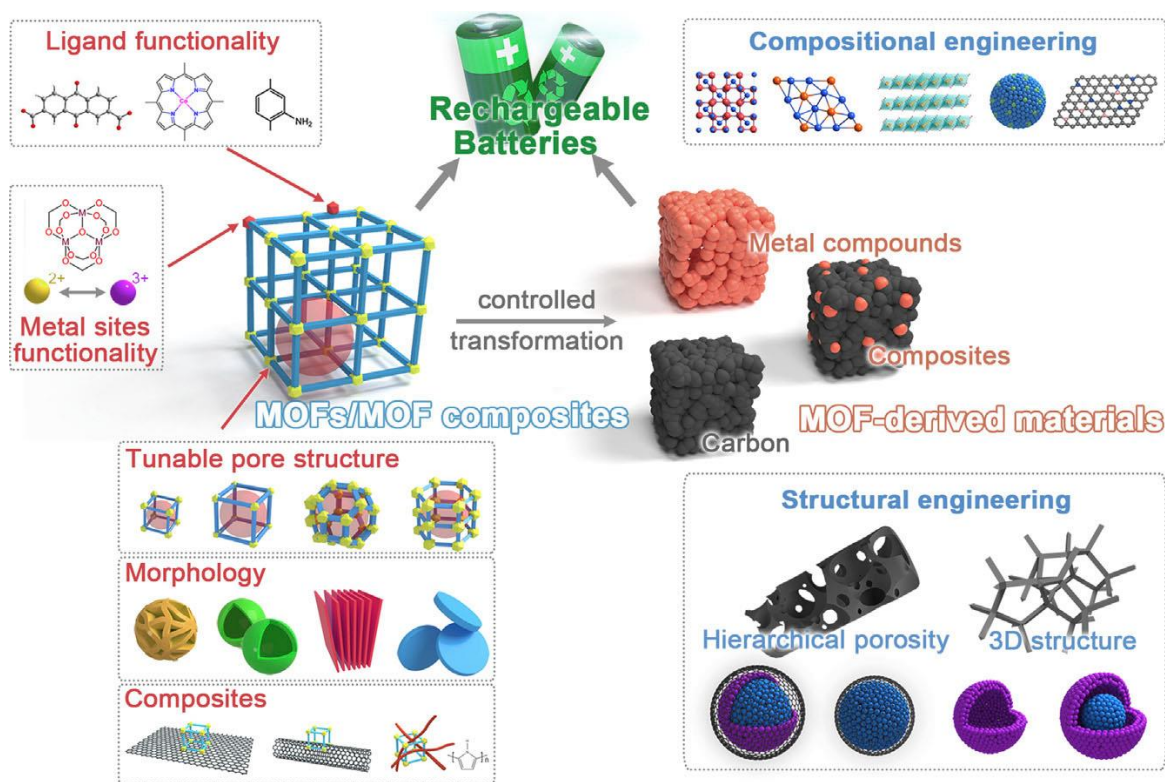
Figure 1.18 Schematic illustration of MOF-related materials for rechargeable batteries[92]

1.5.2 General classification of MOFs

There are various types of metal-organic frameworks (MOFs) including different classifications. According to the different organic ligands we can divide MOFs into metal carboxylic acid frameworks[93], metal azolate frameworks[94], and mixed ligands frameworks. For metal carboxylic

acid frameworks, it is easier to control the structures and modify the organic ligands, while the stability and predictability of the structures are better for metal azolate frameworks. These properties can be recognized by the framework design principles. For example, the sp^3 O atom in the carboxylate usually coordinates variably (typically up to three metal ions) (**Figure 1.19**). In comparison, each N-donor of azolate generally coordinates with only one transition-metal ion in the same direction as its lone electron pair as those in pyridines.[94]
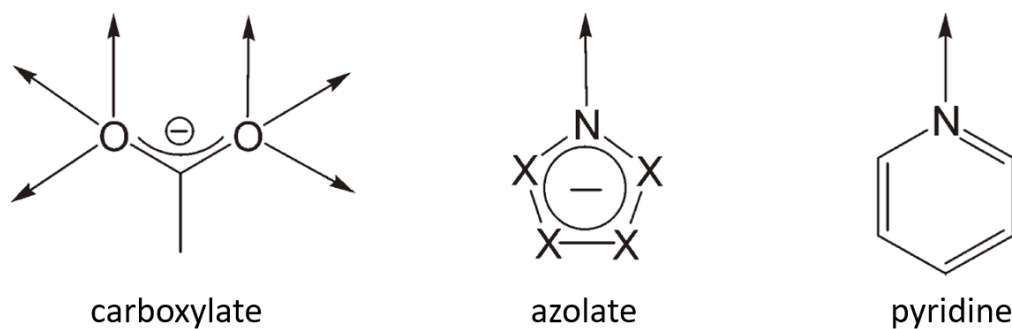
Figure 1.19 Comparison of typical coordination modes of carboxylate, azolate and pyridine (X=C-H or N)[94]

Here we exhibit several well investigated MOFs for metal carboxylic acid frameworks and metal azolate frameworks in **Figure 1.20** and **Figure 1.21**, respectively. These MOFs have been well investigated primarily for their gas adsorption properties as well as for possible application in sensing, drug delivery, catalysis, and optoelectronics.[95] Recently, the potential impact of these materials as solid-like electrolytes has been confirmed by numerous examples of high proton conductivity[96-97], but report of Na^+, Mg^{2+}, or Al^{3+} ion conductors are relatively rare.
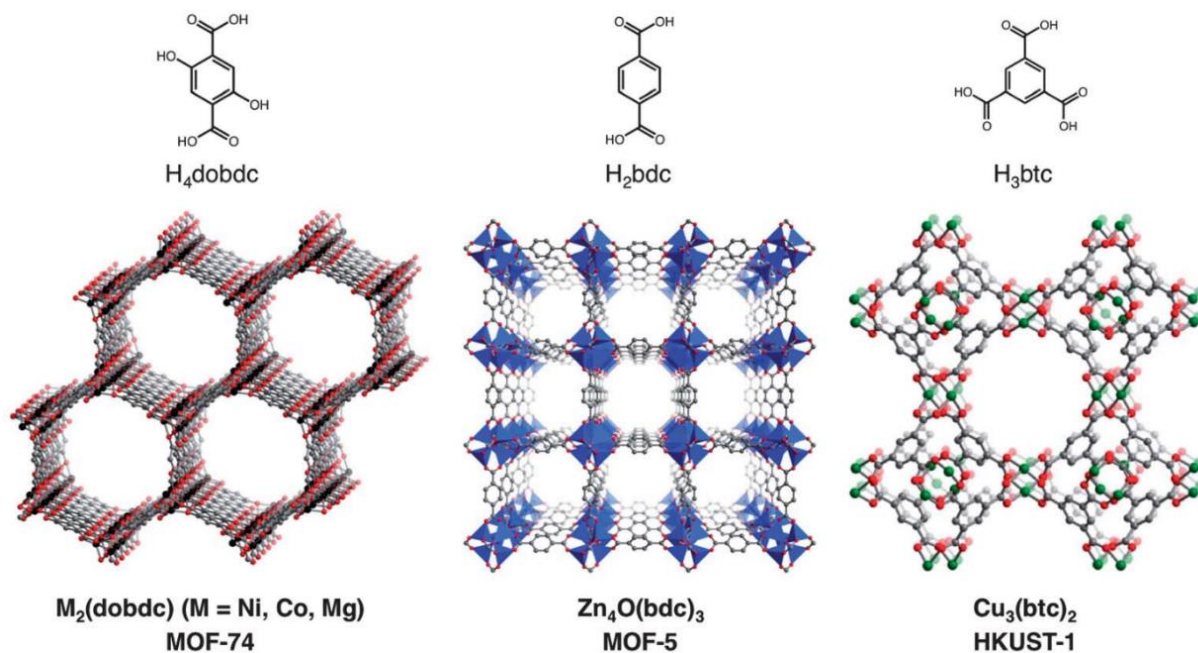
Figure 1.20 Well-investigated MOFs for metal carboxylic acid frameworks.[95] Crystal structures and organic bridging ligands for metal carboxylic acid frameworks: $M_2(dobdc)$ (M = Ni, Co, Mg; $dobdc^{4-}$ = 2,5-dioxido-1,4-benzenedicarboxylate; MOF-74), $Zn_4O(bdc)_3$ (bdc^{2-} = 1,4-benzenedicarboxylate; MOF-5), and $Cu_3(btc)_2$ (btc^{3-} = 1,3,5-benzenetricarboxylate; HKUST-1). Green, gray, and red spheres represent Cu, C, and O atoms, respectively; H atoms have been omitted for clarity. Black spheres represent Ni, Co, or Mg atoms, and blue tetrahedra represent Zn atoms.
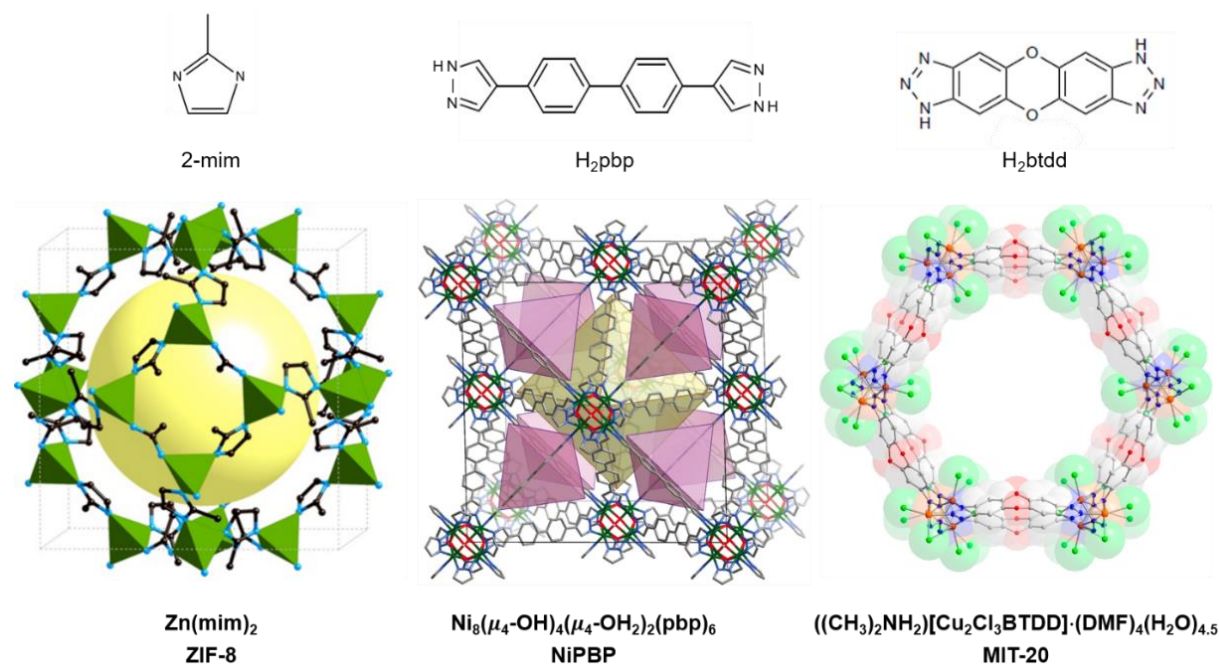
Figure 1.21 Well-investigated MOFs for metal azolate frameworks. Crystal structures and organic bridging ligands for metal azolate frameworks: $Zn(mim)_2$ (Black and blue spheres represent C and N, green tetrahedra represent Zn atoms, β-cage with inner cavity highlighted in yellow; ZIF-8)[98], fcc-$Ni_8(\mu_4\text{-OH})_4(\mu_4\text{-OH}_2)_2(pbp)_6$ (C, grey; Ni, green; N, blue; O, red; NiPBP),[94] $((CH_3)_2NH_2)[Cu_2Cl_3BTDD]\cdot(DMF)_4(H_2O)_{4.5}$ (C, grey; Cu, yellow; N, blue; Cl, green; O, red; MIT-20).[99] H atoms have been omitted for clarity.

1.5.3 Strategies explored in MOFs based solid-like electrolytes

Although difficulties, several strategies have been explored in introducing free Li^+, Na^+ or Mg^{2+} ions into MOFs by Jeffrey R. Long's group. The first Li^+ and Mg^{2+} MOF-based solid-like electrolytes was successful introduced by using $Mg_2(dobdc)$ (Mg-MOF-74), the structure of $Mg_2(dobdc)$ consists of one-dimensional hexagonal channels with diameters of ~14 Å that are lined with coordinatively unsaturated Mg^{2+} cation sites (see **Figure 1.22**). The key point of this strategy is that after alkoxide anions bind to these sites, it can form not only relatively free Li^+

cations moving channels but also a high density of charge carriers framework which allow Li^+ cations to hop from site to site while remaining solvated by the carbonate molecules. The result shows the new solid lithium electrolyte $Mg_2(dobdc) \cdot 0.35LiO^iPr \cdot 0.25LiBF_4 \cdot EC \cdot DEC$ can reach 3.1×10^{-4} S cm^{-1} at 300K and an activation energy of 0.15 eV. Also, this paper reveals that intraparticle transport dominates conduction through single-particle data.[70] Furthermore, this type of MOF can be applied to solid magnesium electrolytes which can reach to 0.25 mS cm^{-1}.[69]
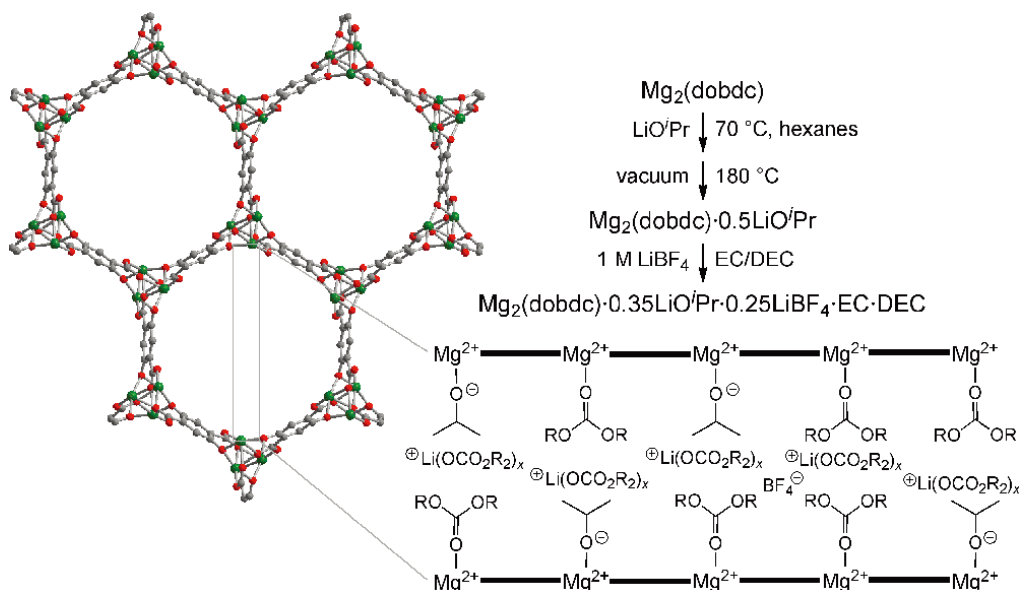
Figure 1.22 Structure of $Mg_2(dobdc)$ and the scheme for its modification to form the solid electrolyte.[70] A representation of a cross-sectional view along a channel of the solid is shown at the lower right [R= $-CH_2-CH_2-$ (EC) or $-CH_2CH_3$ (DEC)].

An alternative strategy is the post-synthetic functionalization of the inorganic units within MOFs. The metal cations present in the MOF crystal lattice are organized in well-defined inorganic structural patterns, which generally known as secondary building units (SBUs).[100] For example, bridging OH groups within MOFs can exhibit a high density of functional groups, by dehydrating of inorganic clusters and grafting of LiO^tBu in $Zr_6O_4(OH)_4(bdc)_6$ (UIO-66) leads to good solid

30

ionic conductors. The result shows the room temperature ionic conductivity of the LiO^tBu-grafted UIO-66 sample can reach 1.8×10^{-5} S cm^{-1}.[91] The mechanism is proposed in **Figure 1.23**, the highlight of this paper is to construct a Li$^+$ solid electrolyte in which the anions are immobilized through post-synthetic functionalizable SBUs, would not only prevent polarization effects (one is decrease of the operating voltage of the cell) caused by anion migration but would also avoid the decomposition of the reactive electrodes. The latter phenomenon has been confirmed as an important contributor to capacity fade in batteries.[101]
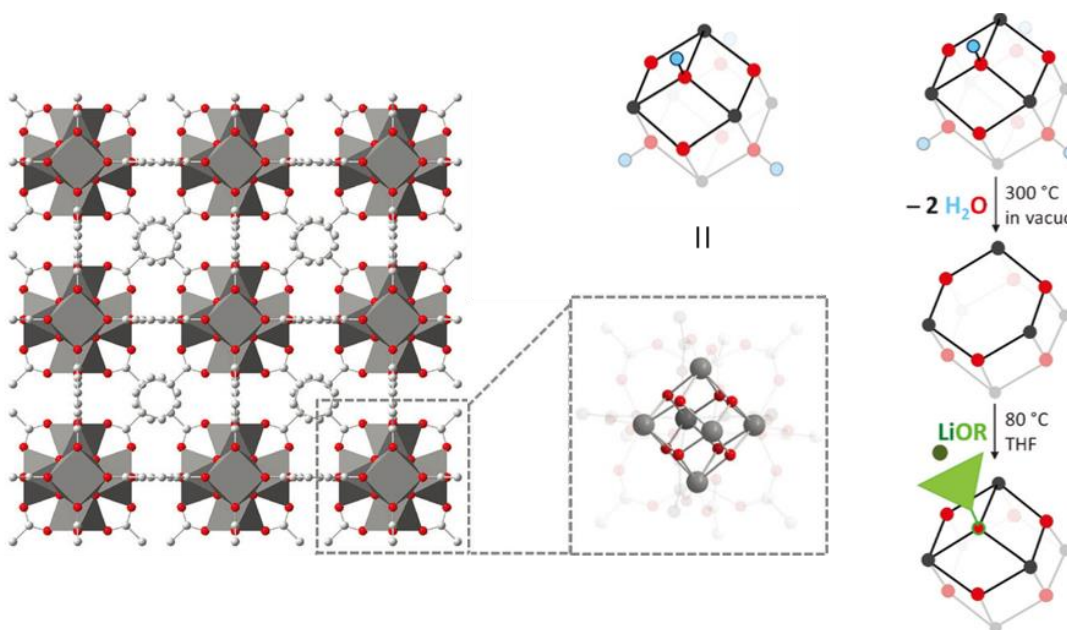
Figure 1.23 Mechanism of the two-step dehydrating and grafting process.[91] On the left, the position of the $Zr_6O_4(OH)_4(O_2CR)_{12}$ clusters in the crystal lattice and the structure of the cluster core is shown. On the right, the two-step modification process is depicted, which consists of dehydration of the cluster core and subsequent grafting of lithium tert-butoxide. Zr gray, O red, C dark green, H blue. The aliphatic part of the grafted alkoxide is represented by a light green triangle.

A third approach is to take advantage of the equilibrium conditions between metal and ligands in MOFs, that is by selecting scandium (III) to partially replace cadmium (II) in the parent MOF formula $\{[CdM(\mu_4\text{-pmdc})_2(H_2O)_2] \cdot solv_n$ (M^{II} = Cd, Mn, Zn). This trivalent metal imposes a charge imbalance that requires monovalent ions to be present in the crystal structure and remaining mobile (Sc^{3+} + M^+: $2 \times pmdc^{2-}$, M=Li, Na). In this work, two new heterometallic 3D porous scandium(III)/ alkaline/ pyrimidine-4,6-dicarboxylate frameworks, namely EHU1(Sc,Li) and EHU1(Sc,Na), have been achieved. The results show the EHU1(Sc,Li) $\cdot$ (LiBF$_4$) exhibits a promising conductivity of 4.2×10^{-4} S cm^{-1} at room temperature with a low activation energy (0.25 eV), and EHU1(Sc,Na) $\cdot$ (NaPF$_6$) represents the first MOF to show ionic conductivity provided by the Na ion of 9.2×10^{-5} S cm^{-1} at room temperature.[102]

Most recently another strategy put forward a potential blueprint to optimize ion carrier density in MOF solid electrolytes by preferential formation of an anionic MOF: MIT-20. From the structure of ((CH$_3$)$_2$NH$_2$) [Cu$_2$Cl$_3$BTDD] $\cdot$ (DMF)$_4$(H$_2$O)$_{4.5}$ (MIT-20, see **Figure 1.24**), it is confirmed by ^{1}H NMR that the MIT-20 is formally anionic with the charge balance provided by free dimethylammonium (DMA) cations. Thus, the free DMA indicated that MIT-20 could function as a platform for various cationic species, including Li$^+$, Na$^+$, or Mg^{2+} for developing solid electrolytes in the presence of appropriate solvents.[99] We note that solid-like MOF electrolytes were also synthesized by reacting a Cu-azolate framework with metal halides (LiCl, MgBr$_2$ and AlCl$_3$), where the abundant OMSs bind with the halide anions, leading to the formation of solid-like electrolytes with an ionic conductivity of 2.4×10^{-5}, 1.3×10^{-4} and 8.1×10^{-6} S cm^{-1} in presence of PC, respectively.[103] Nonetheless, aluminum is commonly used as the current collectors in lithium-ion batteries, the use of metal halides, unavoidably raising the corrosion concerns.[104]
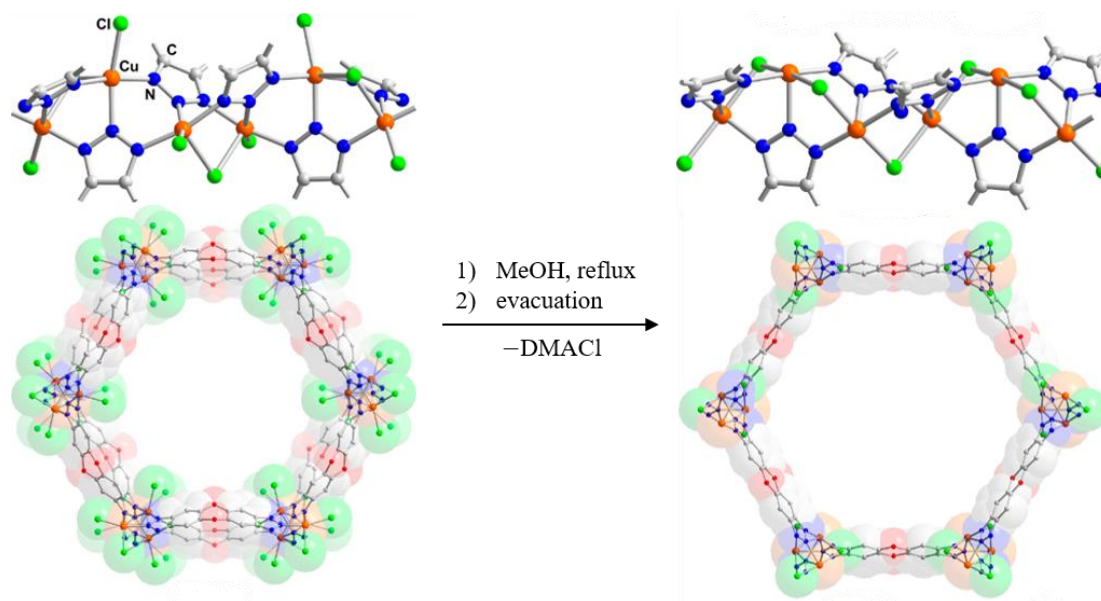
Figure 1.24 X-ray crystal structure of MIT-20 and MIT-20d. The latter formed from the former by loss of DMACl. The structure of MIT-20-X (X=LiCl, LiBr, Na, Mg), are analogous to MIT-20. H atoms are omitted for clarity.[99]

In conclusion, we collect the strategies mentioned before to **Table 2**, give a panoramic summary of state-of-the-art MOFs based solid electrolytes. To date, despite serval strategies have been investigated in MOFs based solid electrolytes, the fundamental mechanism and theory, general approach towards ionic conductors and adaptation of ionic conductors for practical battery applications have not been fully explored. In this dissertation, we developed a novel class of MOFs based solid-like electrolytes with artificial ionic channels, which can provide superior ionic conductivity and low activation energy. Then we applied the MOFs to different cations, from the 3rd period (Na^+, Mg^{2+} and Al^{3+}) and the 1st group (Li^+, Na^+, K^+ and Cs^+) with same anions to investigate whether different ionic radii of cations carriers can bring different properties to MOFs based solid-like electrolytes.

Table 2 | Summary of MOFs based solid-like electrolytes from literatures

Compound	Ion	σ (S/cm)	E_a (eV)	Year	Ref.
$Mg_2(dobpdc) \cdot Mg(OPhCF_3)_2 \cdot Mg(TFSI)_2$	Mg^{2+}	2.5×10^{-4}	0.11-0.19	2014	[69]
$Mg_2(dobdc) \cdot LiO^iPr \cdot LiBF_4$	Li^+	3.1×10^{-4}	0.15	2011	[70]
$[Zr_6O_4(OH)_4(bdc)_6] \cdot LiO^tBu$	Li^+	1.8×10^{-5}	0.18	2013	[91]
$EHU1(Sc,Li) \cdot (LiBF_4)$	Li^+	4.2×10^{-4}	0.25	2016	[102]
$EHU1(Sc,Na) \cdot (NaPF_6)$	Na^+	9.2×10^{-5}	0.64	2016	[102]
$MIT-20-LiBF_4$	Li^+	4.8×10^{-4}	0.16	2017	[99]
MIT-20-Na	Na^+	1.8×10^{-5}	0.39	2017	[99]
MIT-20-Mg	Mg^{2+}	8.8×10^{-7}	0.37	2017	[99]
MOF-LiCl	Li^+	2.4×10^{-5}	0.34	2019	[103]
$MOF-MgBr_2$	Mg^{2+}	1.3×10^{-4}	0.24	2019	[103]
$MOF-AlCl_3$	Al^{3+}	8.1×10^{-6}	0.32	2019	[103]

Furthermore, with relatively rare research on Na^+, Mg^{2+} and Al^{3+} ion conductors, we extended the applications of MOFs based electrolytes from lithium-ion batteries to sodium-ion batteries, lithium-sulfur batteries. For instance, sodium-ions batteries are considered as the best candidate for mid-to-large-format energy storage applications because sodium is widely available (fourth most abundant element on earth) and exhibits similar chemistry to that of LIBs. The study of solid electrolytes for sodium-ions batteries is still at a very early stage, but the advantages of solid-state electrolytes such as thermal and chemical stabilities, safety (non-explosive) and versatile geometries attract us to further investigate this area.[105]

1.6 Practical application of solid electrolytes in battery devices

1.6.1 Polymer-based composite solid electrolytes
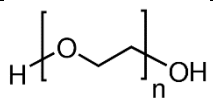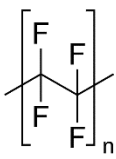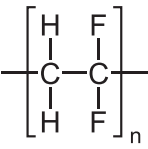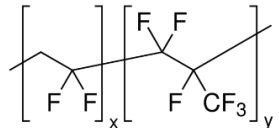
Despite much efforts have been made in solid electrolyte system, the application of solid electrolytes in real batteries is still hard to realize due to the ionic conductivity and the electrochemical stability issues. To meet the commercial requirements, high ionic conductivity, favorable mechanical strength, and outstanding interfacial compatibility with electrode are the most fundamental requirements for solid electrolytes.[106] As we discussed before, oxide and sulfide materials are two types widely used in inorganic electrolytes. For example, $Li_{10}GeP_2S_{12}$ solid electrolyte exhibits an extremely high lithium ionic conductivity of 12 mS cm^{-1} at room temperature.[52] However, high processing difficulty, poor compatibility and low oxidation stability limit its wide application.[107] In this case, solid polymer electrolytes not only provide high electrochemical stability and high safety, but are also good in flexibility and easy to produce. These properties endow the high possibility for the use of solid polymer electrolytes in the next-generation high energy density batteries. In the meantime, solid polymer electrolytes also called as polymer gel electrolytes, can stabilize the Li metal dendrite growth even when the electrolyte modulus is well below that of Li-metal.[108] Solid polymer electrolytes, including polyethylene oxide (PEO), polytetrafluoroethylene (PTFE), polyvinylidene difluoride (PVDF), Poly(vinylidene fluoride-hexafluoropropylene) (PVDF-HFP) have been extensively investigated. However, the ionic conductivity and mechanical strength of solid polymer electrolytes are not ideal, trade-off between modulus and conductivity is the major obstacle for their further application.[109] In order to improve the polymer electrolyte system, various composites had been mixed into polymers. As shown in **Figure 1.25**, including inert ceramic fillers, fast-ion conductive ceramics, lithium salts, ionic liquid, etc.[110]
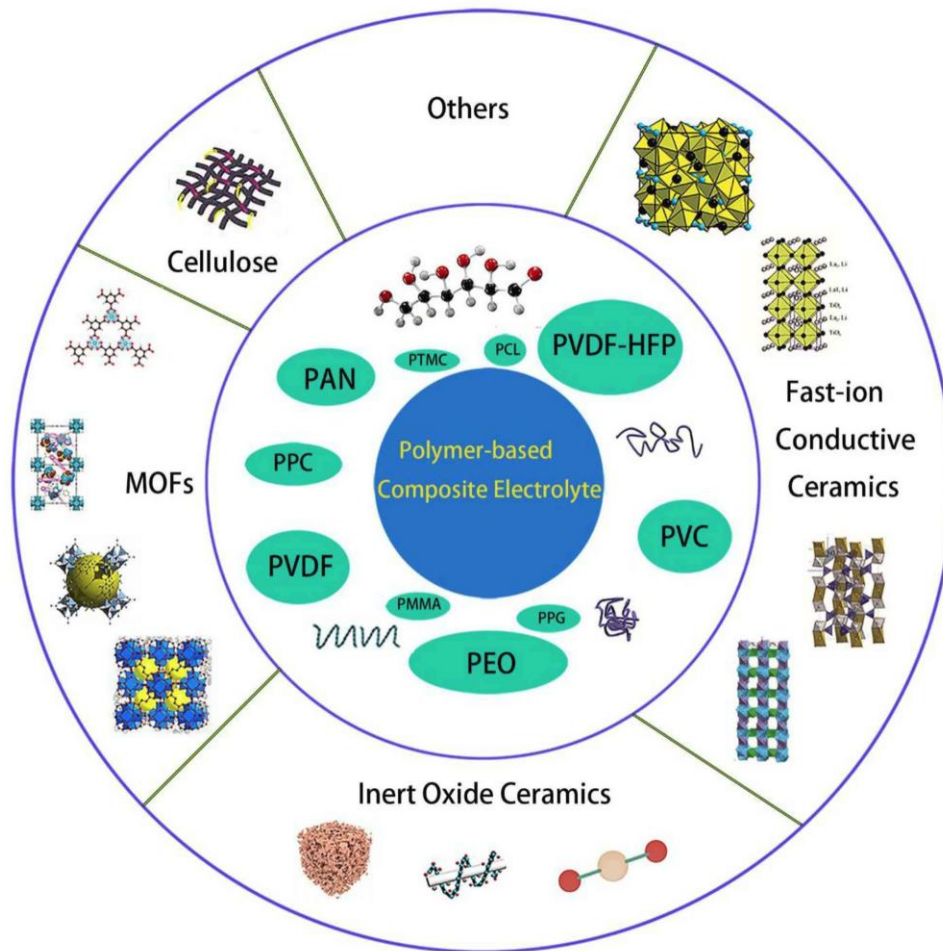
Figure 1.25 Categories of the existing polymer-based composite solid electrolytes.[110]

The commonly used polymer matrices and properties for polymer-based composite solid electrolytes are summarized in **Table 3**. To get high lithium ion conductivity, polymer should not only dissolve lithium salt, but also be able to interact with lithium ions. The polar groups in the polymer (—O—, —F—, etc.) are effective building blocks for dissolving lithium salts. In the beginning, most of the research focused on the PEO and its derivatives. The lone pair of oxygen on the PEO segment is coordinated to lithium ion by Coulombic interaction, increase the dissociation between the lithium ion and anion. However, lithium ion tends to imprison on the PEO chains, resulting in low ionic conductivity at ambient temperature.[111]

Table 3 / Common polymer matrix and properties[110, 112]

Polymer matrix	Molecular formula	T_g (ºC)	T_m (ºC)
PEO		− 64	65
PTFE		130	327
PVDF		− 40	178
PVDF-HFP		− 90	135

glass transition temperature T_g, melting temperature T_m

Although solid-state PEO-based batteries have been commercialized by BlueCar since the 2000s, several challenges remain for improvement of their performance (specifically the ionic conductivity in low temperature) and achieving full commercialization.[113] Recently, the progressive deterioration of PEO-based solid polymer electrolyte resulting outgassing of the cell during cycling has been reported. The researcher concluded that polymer (PEO) decomposition was the principal failure mechanism for this type of Li-polymer battery with NMC or LFP cathode.[114] For PTFE, PVDF, PVDF-HFP polymer matrix contain strong electron-withdrawing functional group (—F—), which is beneficial for the dissolution of lithium salts to keep a high concentration of charge carriers. PTFE has good chemical and thermal stability, which can be used as membrane separator in lithium ion batteries.[115] PVDF and PVDF-HFP comprising both amorphous and crystalline phase, the amorphous phase of the polymer helps for higher carriers concentration, whereas the crystalline phase acts as mechanical support for the polymer

electrolyte.[116] Due to the copolymerization of VDF and HFP, PVDF-HFP has a relatively lower crystalline compared with PVDF. Therefore, PVDF-HFP contains more amorphous domains to capable of trapping larger amount of liquid electrolytes. Hence, PVDF-HFP is regarded as the most promising matrix for gel polymer material.[117]

1.6.2 Strategies of composite polymer electrolytes in real batteries

As we discussed in **Figure 1.25**, several composite approaches have been explored to further improve the ionic conductivity of solid polymer electrolytes. For example, addition of inert ceramic fillers, fast-ion conductive ceramics, MOFs and ionic liquid into the polymer skeleton, which can inhibit the recrystallization kinetics of the polymer chains for intensifying localized amorphization, ultimately increasing the ionic conductivity and electrochemical stability of the composite polymer electrolytes simultaneously.[118]

1.6.2.1 Inert ceramic-based composite polymer electrolytes

Cui et al.[119] introduced a in situ synthesis of monodispersed SiO_2 nanospheres into PEO-LiClO$_4$ composite polymer electrolytes, which significantly suppress the crystallization of the PEO matrix, presenting an ionic conductivity of 4.4×10^{-5} S cm^{-1} at 30 ℃. Similar approach proposed a self-assembly in situ construction of 3D network-structured PEO@SiO$_2$, achieving an improved ionic conductivity of 1.1×10^{-4} S cm^{-1} at 30 ℃.[120] The strategy here using Lewis-base and weak hydrogen bonds (as shown in **Figure 1.26**) for self-assembly in situ synthesis. The crystallinity of PEO was reduced remarkably by synergistically rigid-flexible coupling dynamic balance, which lead to high ionic conductivity and improved SEI stability (electrochemical stability window > 4.8 V at 90 ℃).
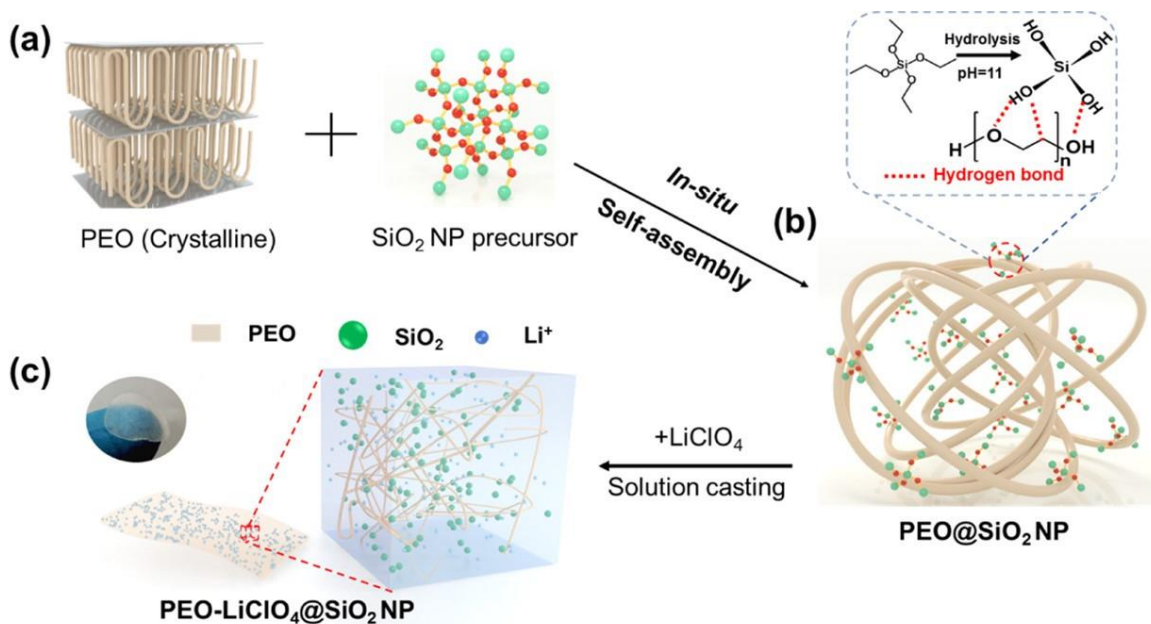
Figure 1.26 Synthetic routes and morphology of the PEO−LiClO4@SiO$_2$ CPEs. (a) Crystalline PEO and SiO2 nanoparticle precursor (TEOS). (b) SiO$_2$ nanoparticles self-assembly into PEO amorphous chains through a hydrogen bond. The inset shows the in situ hydrolysis reaction of TEOS.(c) PEO-based CPE membranes obtained by solution casting.[120]

1.6.2.2 Fast-ion conductive ceramics composite polymer electrolytes

As the polymer matrix in the composite polymer electrolytes, PEO is most explored. However, PEO shows higher viscosity and poor film-forming ability compared with PVDF. The polarization of PVDF is effective in dissociating lithium salt and probably enhance the ionic conductivity.[121] Furthermore, PVDF has good electrochemical stability and much better thermal stability and mechanical strength than PEO.[122] Here, a flexible composite polymer electrolytes compose of PVDF matrix and Li$_{6.75}$La$_3$Zr$_{1.75}$Ta$_{0.25}$O$_{12}$ (LLZTO) fillers was reported.[123] The research indicates that La atom of LLZTO could complex with the N atom and C=O group of solvent molecules N,N-dimethylformamide (DMF) and induces the chemical dehydrofluorination of the PVDF skeleton

and thus enhances the interactions between the PVDF matrix, lithium salt, and LLZTO particles

(see **Figure 1.27** for complex structures). As a result, a high conductivity of 5×10^{-4} S cm^{-1} at

25 ºC, high mechanical strength, and good thermal stability were achieved.
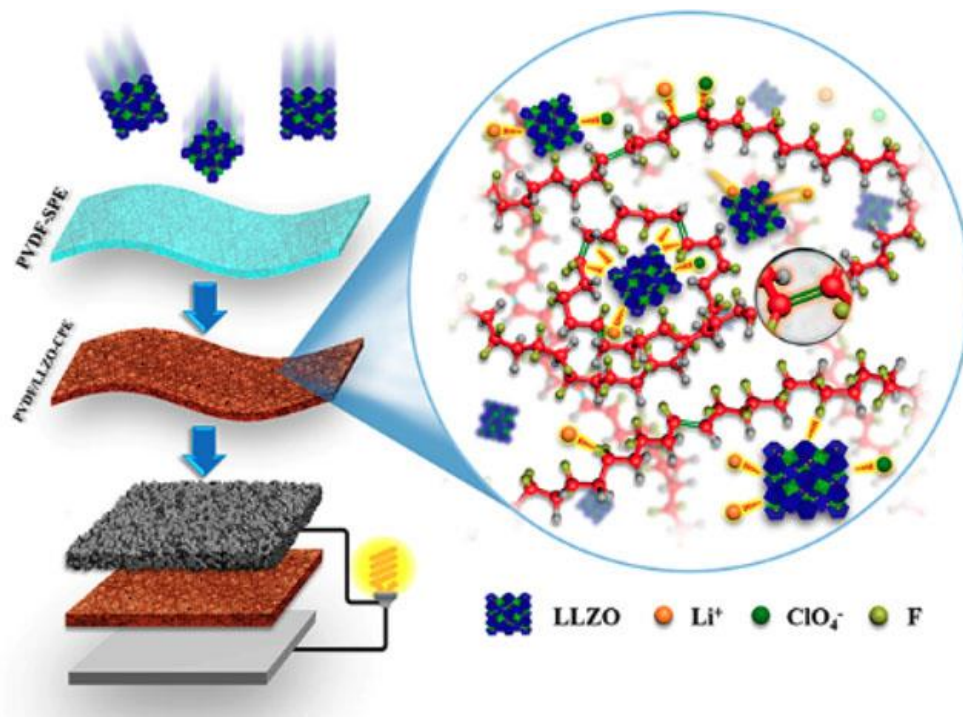
Figure 1.27 Complex structures of PVDF/LLZTO-CPEs, where blue clusters denote LLZTO[123]

1.6.3 MOF-based solid-like electrolytes in batteries application

1.6.3.1 MOF with ionic liquid solid-like electrolytes

To address the interfacial issue and achieve higher energy density of solid-state batteries, a solid-

like electrolytes based on ionic-liquid-impregnated MOF nanocrystal (Li-IL@MOF) was reported.

The strategy here is to use MOF as a porous host provides 3D open solid framework and the Li$^+$

containing ionic liquid guest serves as the Li$^+$ conductor. As shown in **Figure 1.28**, Li-IL@MOF

solid-like electrolyte shows a high room-temperature ionic conductivity of 3×10^{-4} S cm^{-1}, an

improved Li$^+$ transference number of 0.36 and good compatibilities against both Li metal and

active electrode.[124] The author concluded that the nanoconfined Li-IL guest can provide a unique

interfacial wettability effect between the solid-like electrolyte and the active electrodes, lead to a remarkable battery performance.
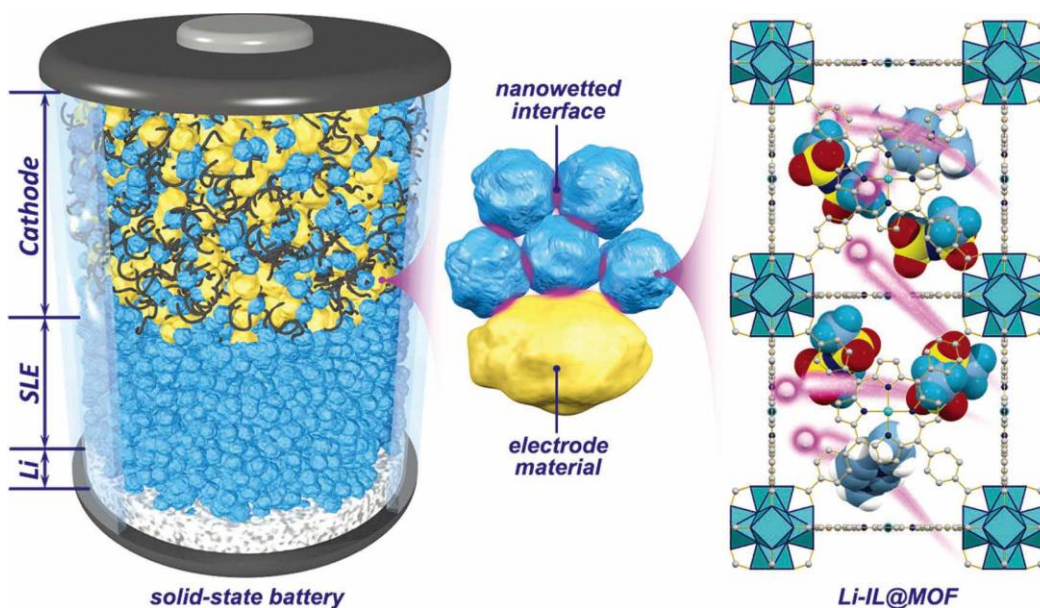
Figure 1.28 Schematic illustration for the architecture and nanowetted interfacial mechanism of the solid-state battery with a magnification showing crystal structures of the MOF.[124]

However, the MOF used here is MOF-525 (Cu), which narrows the electrochemical window (from 2 – 4.1 V) due to the redox-active Cu(II) centers.[125] Thus, this solid-like electrolyte was not applicable to the high-voltage layered oxide cathodes. In the meantime, the ionic liquid is LiTFSI in [EMIM][TFSI], where EMIM is 1-ethyl-3-methylimidazolium and TFSI is bis(trifluoromethylsulfonyl)amide. Here, the use of ionic liquid undoubtedly significantly increases the cost for battery devices, where [EMIM][TFSI] cost $576 for 25 g at Sigma-Aldrich.

1.6.3.2 MOF-polymer composite solid electrolyte

As we mentioned before, it is found that addition of inorganic fillers such as Al_2O_3, SiO_2, MgO, and $MgAl_2O_4$ in PEO-based composite polymer electrolytes is an effective way to improve the

ionic conductivity and the interfacial contact between electrolytes and electrodes. This is because inorganic particles greatly promote charge carrier transportation through decreasing the crystallinity of PEO.[126] Moreover, it has been demonstrated that the Lewis acidic surface properties of nano-scale fillers can enhance the interaction with anions, which is beneficial for dissociating the lithium salt and increasing chare carrier transport.[127] Compared with inert inorganic nanoparticles, MOFs not only possess similar properties to inorganic zeolite fillers (high thermal stability, large surface area and microporous structure), but also Lewis acidic surface properties. Besides, MOFs have unique organic functional groups, which can be easily decorated. Here, a hybrid composite polymer electrolyte in which the MOF (UIO-66-NH$_2$) is chemically linked with the polymer (PEGDA). As a result, a moderate ionic conductivity (4.31×10^{-5} S cm^{-1}), superior interfacial compatibility, and excellent high/low temperature cell performance were reported.[128]
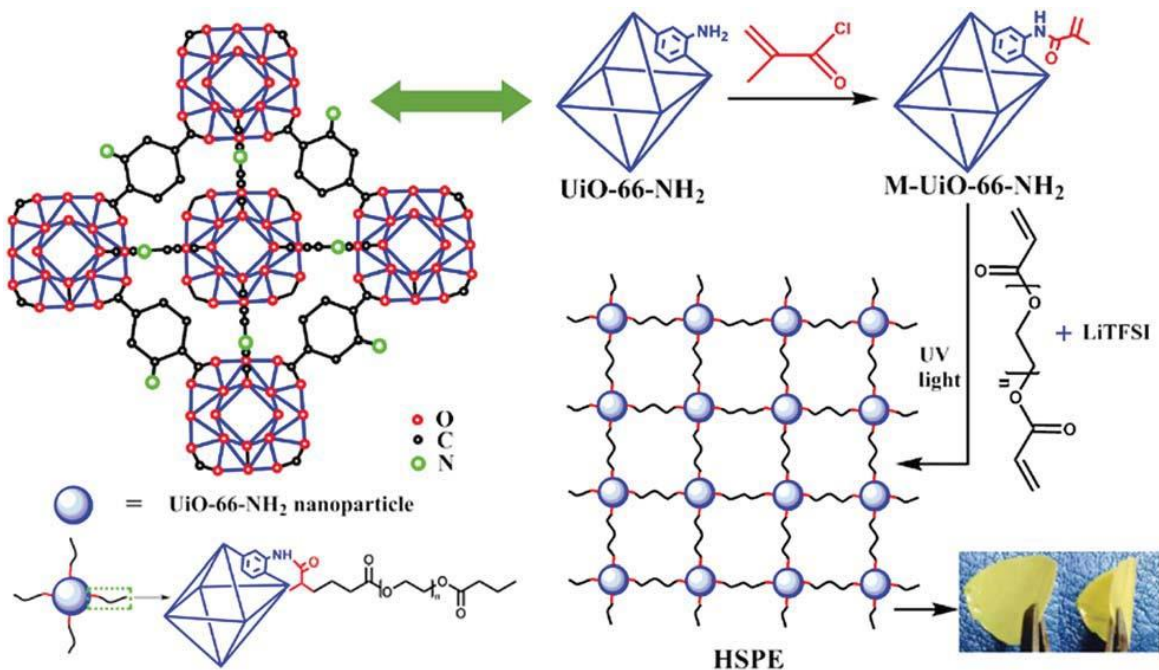
Figure 1.29 Synthetic route of the hybrid covalently linked MOFPEGDA- based all-solid-state electrolyte[128]

OBJETIVES

In general, the objective of this dissertation is to develop a novel family of solid-like electrolytes by infiltrating MOF scaffolds with the liquid-electrolyte counterparts, which address the safety concerns in current state-of-the-art Li-ion batteries. In the meantime, allow the implementation of high energy density batteries, such as Li-metal batteries. This work attempts to reveal the ion-conduction principles of the solvated cations in anion-complexed MOFs, containing cations from the 3rd period (Na^+, Mg^{2+} and Al^{3+}) and 1st group (Li^+, Na^+, K^+ and Cs^+). Thus, this work endeavors to provide reliable principles to the design of fast-conducting solid-like electrolytes for alkali or multivalent metal ions.

Furthermore, this dissertation tries to expand the application of such MOF-based solid-like electrolytes from Li^+ to Na^+, explore the potential utilization in real batteries devices (Such as Na-metal batteries). In addition, this work attempts to modify the MOF metal centers to investigate the possibility for further applications such as Li-S batteries.

EXPERIMENTAL PROCEDURES

3.1 Chemicals

All chemicals were used without further purification except for Aluminum perchlorate nonahydrate. The major chemicals used in this dissertation are listing as following:

Aluminum nitrate nonahydrate (Al(NO$_3$)$_3$ · 9H$_2$O, ACS reagent, $\geqslant$98%, Sigma-Aldrich)

Trimethyl trimesate (C$_6$H$_3$(CO$_2$CH$_3$)$_3$, 98%, Sigma-Aldrich)

Lithium perchlorate (LiClO$_4$, battery grade, dry, 99.9%, Sigma-Aldrich)

Sodium perchlorate (NaClO$_4$, anhydrous, $\geqslant$99.0%, Sigma-Aldrich)

Magnesium perchlorate (Mg(ClO$_4$)$_2$, dry, ACS reagent, $\geqslant$99.0%, Sigma-Aldrich)

Aluminum perchlorate nonahydrate (Al(ClO$_4$)$_3$·9H$_2$O, 98%, Sigma-Aldrich) was vacuum-dried for 24 h at 150 ℃ to get rid of water of crystallization.

Potassium perchlorate (KClO$_4$, ACS reagent, $\geqslant$99.0%, Alfa Aesar)

Cesium perchlorate (CsClO$_4$, Reagent Grade, Alfa Aesar)

Propylene carbonate (PC, anhydrous, 99.7%, Sigma-Aldrich)

Dimethyl sulfoxide (DMSO, anhydrous, >99.8%, Alfa Aesar)

Polytetrafluoroethylene dispersion (PTFE 60 wt % dispersion in H$_2$O, Sigma-Aldrich)

Poly(vinylidene fluoride-co-hexafluoropropylene) (PVDF-HFP, Kynar Flex 2801)

Ethylene carbonate (EC, anhydrous, 99%, Sigma-Aldrich)

Dimethyl carbonate (DMC, anhydrous, 99%, Sigma-Aldrich)

Sodium phosphate monobasic (NaH$_2$PO$_4$, anhydrous 99%, Acros Organics)

Ammonium metavanadate (NH$_4$VO$_3$, ACS reagent, Acros Organics)

3.2 Sample Preparation

Synthesis of MIL-100(Al). The MOF was synthesized according a reported microwave-assisted method.[129] Briefly, 1.43 g of aluminum nitrate nonahydrate and 1.21 g of trimethyl trimesate were dispersed in 20 mL of water, followed by the addition of 4 mL nitric acid (4 M). The mixture was then transferred to a microwave reactor, which was heated at 1500 W to 240 ℃ in 6 min and held at 240 ℃ for 1 min. After the reactions, the sample was collected by centrifugation and washed with water, followed by methanol exchange over a period of three days. The sample was replenished with fresh methanol twice a day and dried at 80 ℃ overnight before further characterizations.

Synthesis of solid-like electrolytes M-MOF (M=Li, Na, K, Cs, Mg and Al). The MOF particles were activated under vacuum at 350 ℃ for 24 hours and subsequently transferred to an argon-filled glovebox without contacting with moisture in the air. Then, the samples were soaked in 1M $NaClO_4$, $Mg(ClO_4)_2$ or $Al(ClO_4)_3$ in PC (denoted as M-PC) or 1M $LiClO_4$, $NaClO_4$, $KClO_4$ or $CsClO_4$ in DMSO (denoted as M-DMSO) overnight. The resulted M-MOF (where M stands for cations) electrolytes were then collected as powders after removing any excessive liquid by filtration and pressed into pellets with a diameter of 13 mm at 300 MPa. The surface of each pellet was wiped with tissue paper prior to further electrochemical tests.

Preparation of Li-MOF and Na-MOF electrolyte membranes. The activated MIL-100(Al) powders were homogeneously dispersed in ethanol, and 10 wt% PTFE aqueous dispersion was added to the mixture. After continuous stirring and evaporation of the solvent, the mixture was rolled into flexible MOF/PTFE composite membranes. The membranes were tailored into a desirable size and subjected to the activation process and then soaked in Li-PC and Na-PC. Li/Na-

MOF/PTFE membrane electrolytes were pressed at 200 MPa to extrude any excessive liquid electrolyte and wiped with tissue paper prior to further electrochemical tests.

Synthesis of Na$_3$V$_2$(PO$_4$)$_3$/carbon (NVP/C) electrode. The synthesis of the NVP/C composites was performed by following a mechanical-thermal route.[130] In a nylon jar, 1.22 g NH$_4$VO$_3$, 1.87 g NaH$_2$PO$_4$, 3 g citric acid were added at a molar ratio of 2:3:3. In addition, ethanol (20 ml) was added to the mixture to afford a solid-liquid rheological body. The resulting slurry was ball-milling with Zirconia milling balls for 12 h in air (MSK-SFM-3-MTI Corporation). The milled precursors were dried in oven overnight at 70 °C and then ground with a pestle. In the end, the NVP/C was obtained from the precursors *via* preheating it at 400 °C for 4 h followed by annealing at 800 °C for 8 h in argon atmosphere with a heating rate of 5 °C min^{-1}.

Preparation of MOF/PVDF-HFP composite electrolytes. Both separator and gel electrolyte preparation were performed in glove box under argon atmosphere. Firstly, 0.24 g PVDF-HFP was dissolved in 6 ml mix solvent of EC and DMC (volume ratio 1:5). The solution was stirred at 60 °C for 1h and then 0.24 g activated MIL-100(Al) was added to the solution for continuing stirring overnight before use. Furthermore, we change the content of activated MIL-100(Al) from 0 %, 25 %, 50 % to 75 % with total weight of MOF and PVDF-HFP as 0.48 g, denoted as wt% MOF. The resulting 200 μL composite mixture was dropped on the surface of glass fiber separator (Whatman, GF-C), forming a composite film on the surface of supporting separator after solvent evaporation, denoted as wt% MOF-GF. For solid-like gel electrolyte, 40 uL composite mixture comprising 75 wt% activated MIL-100(Al) particles and 25 wt% PVDF-HFP was casted on Na metal foil. After solvent evaporation, the MOF-polymer composite coated Na foil was gelled by adding 12 μL Na-PC prior to cell assembly.

3.3 Electrochemical Studies

Ionic conductivity was measured using EIS after placing a pellet between two stainless steel in a 2032-type coin cell. The conductivity of liquid electrolytes M-PC (M=Na, Mg and Al) was collected by saturating a glass fiber membrane (Whatman, GF-C) with M-PC. The frequency range was from 10^6 to 1 Hz, and AC amplitude was 100 mV. Ionic conductivity (σ, S cm^{-1}) was determined by using the end point of the semicircle as the ionic resistivity (R, Ohm), thickness (L, cm), and area of the pellet (S, cm^2) based on the formula $\sigma = L/(R \times S)$. To measure the activation energies (E_a), the temperature-dependent ionic conductivities (equilibrated in oven) were fitted into Arrhenius relation ($\sigma=(\sigma_0/T)e^{\wedge}(-E_a/k_BT)$) with a linear fitting coefficient over 0.99, where the σ_0 is a pre-exponential factor, T is the temperature and k_B is the Boltzmann constant.[60]

For cyclic voltammetry (CV) tests, lithium/sodium foils were utilized as the reference/counter electrodes and stainless-steel plates were used as the working electrodes. The CV of Li-MOF and Na-MOF membranes were performed between -0.2 and 5 V (*vs.* Li/Li$^+$ or Na/Na$^+$) at 0.5 mV s^{-1}. CV measurements were performed on a Bio-Logic VMP3 electrochemical workstation, impedance measurements were conducted on a Solartron1860/1287 Electrochemical Interface.

Lithium-ion transference number (t_{Li}^+) was measured by combining an AC impedance measurement and a potentiostatic polarization measurement using Li/electrolyte/Li cells. First, an AC impedance test (10^6 to 1 Hz, 20 mV amplitude) was performed to obtain the initial bulk resistance (R_b^0) and the interfacial resistance (R_{int}^0). The symmetric cell was then subjected to a constant DC voltage (V, 20 mV), during which the initial current (I_0) was monitored until reaching the steady state current (Iss). Another AC impedance test was then conducted to obtain the steady state bulk resistance (R_b^{ss}) and the steady state interfacial resistance (R_{int}^{ss}). t_{Li}^+ was then calculated

47

by the formula: $t_{Li}^+ = I_{ss}(V-I_0 R_{int}^0)/(I_0(V-I_{ss}R_{int}^{ss}))$. Sodium-ion transference number (t_{Na}^+) was measured using a similar approach.

The electrochemical measurements were tested with 2032-type coin cells assembled in a glove box filled with pure argon gas. For sodium-metal batteries, sodium foil was used as anode, 1 M $NaClO_4$ in PC was used as the electrolyte. For Li-S batteries, 1 M LiTFSI with 0.2 M $LiNO_3$ in 1,3-dioxolane/1,2-dimethoxyethane (DOL/DME, v:v = 1:1) was used as electrolyte. For Li-$Li_4Ti_5O_{12}$ (LTO) batteries, 1 M $LiPF_6$ in EC/DEC (v:v = 1:1) was used as electrolyte. The cathode sheets for coin-cell fabrication were prepared by blade-coating of electrode slurry. For cathodes with loading of the active material (~ 2 mg cm^{-2}), (NVP/C, sulfur or LTO), carbon black, and polyvinylidene fluoride (PVDF) were mixed with weight ratio of 8:1:1 to form a homogeneous slurry with N-methyl-2-pyrrolidone (NMP) and then casted onto carbon-coated aluminum foil with a doctor blade. The electrodes were dried at 70 °C in vacuum overnight and then cut into pieces with a diameter of 10 mm.

Galvanostatic charge-discharge measurements were carried out using a Land CT2000 battery tester. The voltage window for Na-NVP, Li-S cells, and Li-LTO cells were 2.5−4.2 V, 1.6–2.7 V, and 1–3 V, where 1 C equals to 118 mA g^{-1}, 1675 mA g^{-1}, and 175 mA g^{-1} respectively. Specific capacities were calculated with respect to the mass of NVP, sulfur and LTO.

3.4 Materials characterizations and structural analysis.

Crystalline structures of the MIL-100(Al) and M-MOF (M=Na, Mg and Al) electrolytes were determined with a Rigaku powder X-ray diffractometer (XRD) using Kα radiation (λ = 1.54 Å). Surface morphology and particle size were determined by scanning electron microscopy (Nova 230 Nano SEM). The BET surface area was determined from adsorption isotherms using a

Micromeritics ASAP 2020 Surface Area Analyzer. Infrared spectra experiments were performed in a transmission mode on a Jasco 420 Fourier transform infrared (FT-IR) spectrophotometer. Thermogravimetric analysis (TGA) was carried out in argon or air atmosphere by a ramping rate of 10 °C min^{-1} using NETZSCH STA 449 F5 Jupiter$^{®}$. X-ray photoelectron spectroscopy (XPS) analysis were performed in the high-vacuum chamber of AXIS Ultra DLD. All the spectra were fitted to Gaussian−Lorentzian functions and a Shirley-type background using CasaXPS software. The binding energy values were all calibrated using C 1s peak at 285.0 eV. Aluminum versus sodium and magnesium ratios were determined by inductively coupled plasma atomic emission spectrometer (ICP-AES, Shimadzu, ICPE-2000) using standard aluminum, sodium and magnesium solutions from Sigma-Aldrich. Calibration were carried out by a series of standard Na, Mg and Al (5, 10, 20, 40 ppm) solutions as baselines, then decomposed 20 ppm electrolytes samples in aqua regia (HNO$_3$: HCl = 1:3 in volume ratio) and dispersed again in 5 wt% HCl solution for quantitative analysis.

RESULTS AND DISCUSSION

4.1 Design and synthesis of MOFs based solid-like electrolytes

4.1.1 Choice of MOFs

From the nonaqueous liquid electrolytes for lithium-based rechargeable batteries, we already know that $LiClO_4$ has been a popular electrolyte solute owing to its solubility and high conductivity (~6.0 mS/cm, 1.0 M in PC at 25 ºC) as well as its high anodic stability. Compared with other electrolyte salts, perchlorate salts also have the merits of being relatively less hygroscopic and are stable to ambient moisture.[67] Thus, they are suitable to serve as a series of cation conductors to be interacted with the unsaturated metal sites in MOFs. To achieve a good performance, the electrolyte materials also need to be chemically stable. Normally most MOFs are unstable in water, acidic and/or basic media[131]. It is not practicable to use unstable MOFs as solid electrolytes. To construct chemically stable MOFs, much progress based on using highly charged metal ions and/or metal-containing secondary building units, such as $Zr_6O_4(OH)_4(CO_2)_{12}$ in Zr-MOFs and $M_3O(X)(CO_2)_6$ (M=Cr or Al and X=F,OH or Cl) in the MIL series of MOFs, has provided feasible approaches to design and synthesize stable MOFs that are able to withstand harsh conditions.[132-133] Form the Zr-MOFs such as UIO-66 showed in **Figure 4.1**a, its secondary building unit is $Zr_6(\mu_3\text{-O})_4(\mu_3\text{-OH})_4$, we aware that removal of the bridging μ_3-OH groups leads to more unsaturated metal sites. In comparison, MIL-MOFs such as MIL-100(Al) showed in **Figure 4.1**b, its secondary building unit is $Al_3(\mu_3\text{-O})(\mu_1\text{-OH})(H_2O)_2$, during dehydration it will be easier to remove the terminal aquo or hydroxyl group than the μ_3-OH in UIO-66.[134]
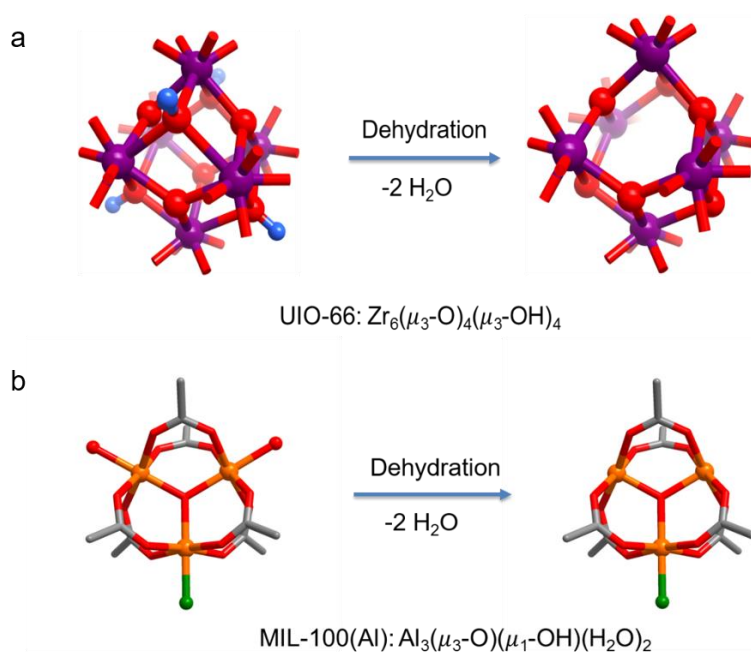
Figure 4.1 Comparison of UIO-66 and MI-100(Al) during dehydration. (a) UIO-66: Zr purple, O red, H blue; (b) MIL-100(Al): Al yellow, O red, C grey, OH green.

Meanwhile, compared with the Cu-azolate MOF, MIL-100(Al) possesses excellent thermal, chemical and electrochemical stabilities, allowing scaled fabrication of solid-like electrolytes.[129] Compared with other solid-like electrolytes using ceramic hollow structures, the anion-complexing and pore-channel structured MIL-100(Al) offers unique advantages on tuning ion transport behaviors under nanoscale environment.[135] Not only the MIL-100(Al) show similar properties to inorganic ceramic materials (such as high thermal stability, large surface area, and Lewis acidic surface properties), but also have unique functional metal centers and organic groups. Besides, aluminum-based MOFs have significant industrial interests (low cost, low density) and Al^{3+} is a strong Lewis acid to interact with guest species.[136] A series of liquid electrolytes containing cations from the 3rd period (Na^+, Mg^{2+} and Al^{3+}) and the 1st group (Li^+, Na^+, K^+ and Cs^+) were systematically explored.

4.1.2 Synthesis and activation of MIL-100(Al)

The optimization of the synthesis of MOFs at the nanoscale has been intensively studied.[137] Typically MIL100-type MOFs can be synthesized by hydrothermal synthesis within a very narrow pH range (0.5-0.7) after heating a mixture of aluminum nitrate, trimethyl 1,3,5-benzenetricarboxylate (Me_3btc), nitric acid, and water at 210 °C for 3.5h.[138] Then the optimization of the synthesis was achieved by the green microwave synthesis, it presented important advantages over the others, such as homogeneous heating along the reactor, lower reaction times and lower polydispersity together with higher synthetic yields. To date, microwave synthesis has been a superior method for MOFs syntheses. Here, we use trimethyl trimesate instead of trimesic acid as the organic precursor, which allows the rapid formation of the pure MIL-100(Al) phase as monodispersed submicron-sized particles of 535 nm (PDI = 0.22) and with a remarkable yield of 98%.[129] The reaction time can be reduced at a heating ramp of 6 min to 210 °C then held for 1 min. After hydrothermal treatment, the resulting mixture need to be washed by water and methanol several times through centrifugation to get pure MIL-100(Al) and exchange solvent molecules remained in the pores. Without these processes, the presence of occluded species within MOF compounds could seriously block access to their pore system, reducing considerably their potential surface area. For instance, anions such as NO_3^- and extra-framework ligands.

Figure 4.2a shows the nanoporous structure of MIL-100(Al), which composes of trimers of alumina (Al) octahedrons capped by terminal ligands (e.g., H_2O and OH^-) and trimesic acid (BTC), containing super-tetrahedrons that contain mesoporous cages (2.5/2.9 nm in diameter) with accessible microporous apertures (0.55/0.86 nm in diameter).[139] Heating MIL-100(Al) ($Al_3O(BTC)_2OH\cdot(H_2O)_2$) at elevated temperature eliminates the metastable H_2O molecules and generates activated MIL-100(Al) ($Al_3O(BTC)_2OH$) with OMSs.[140] Complexing the ClO_4^- anions

with the OMSs immobilizes the anions, allowing effective transport of the solvated cations within the nanoporous channels. (**Figure 4.2**b)
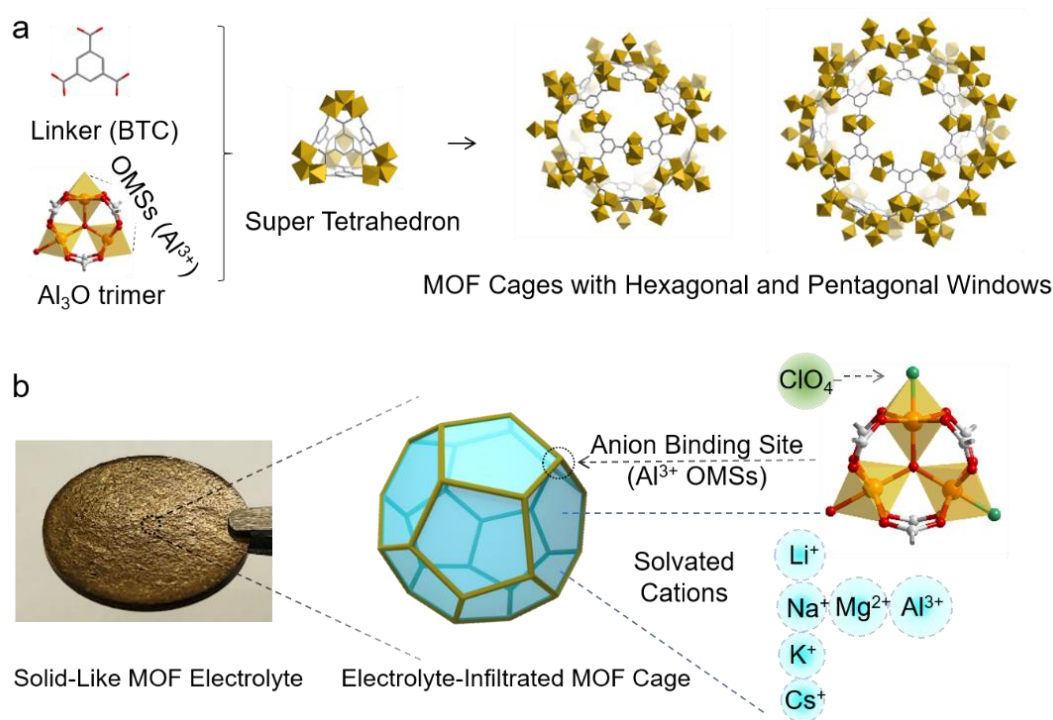
Figure 4.2 (a) A schematic illustration of super tetrahedrons from trimesate linkers (BTC) and Al_3O trimer (Al in orange, O in red, C in grey) forming MIL-100(Al) with mesoporous cages with accessible windows. (b) A photograph of a solid-like electrolyte, where the MOF cages are filled with electrolytes containing cations from the 3rd period (Na^+, Mg^{2+} and Al^{3+}) and from the 1st group (Li^+, Na^+, K^+ and Cs^+) while the anions are complexed to OMSs.

MIL-100(Al) was synthesized using a microwave-assisted method,[129] which shows a particulate size around 500 nm under scanning electron microscope (SEM, **Figure 4.3**a). Nitrogen adsorption/desorption isotherms suggest a highly porous structure with a Brunauer–Emmett–Teller (BET) surface area of 1611 m^2 g^{-1} and a pore volume of 0.95 cm^3 g^{-1} (**Figure 4.3**b). Based on the density functional theory (DFT) model, MIL-100(Al) displays a pore size distribution (inset,

Figure 4.3b) peaking at ~ 0.7 and ~ 2 nm, which are consistent with the aperture and internal diameter of mesoporous cages, respectively (**Figure 4.2**a).[138]
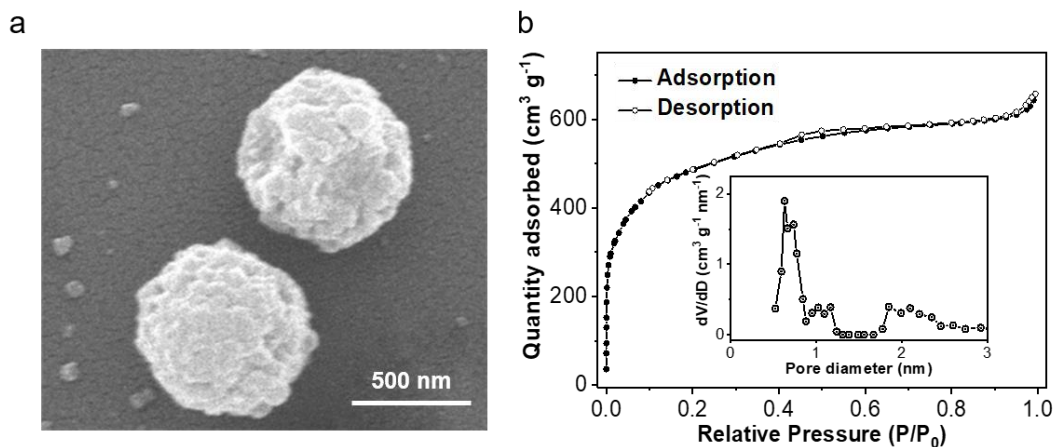
Figure 4.3 (a) A SEM image of MIL-100(Al) particles. (b) N_2 adsorption/desorption isotherms of MIL-100(Al) (inset: pore size distribution derived from a DFT model).
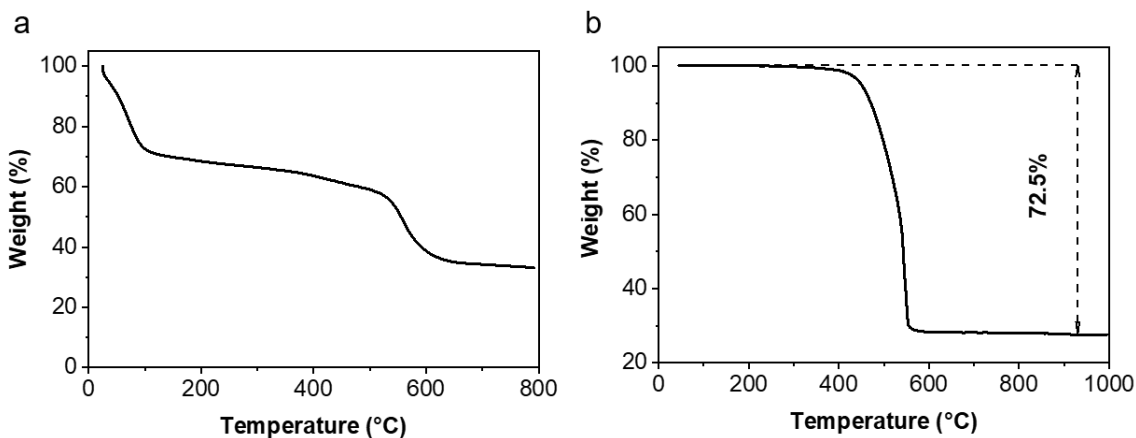
Figure 4.4 (a) TGA plots for pristine MIL-100(Al) in argon. (b) TGA plot for activated MIL-100(Al) in air.

Activation is a key process to prepare useful solid porous materials as catalysts, adsorbents, and molecular sieves. The activation temperature and formula of MIL-100(Al) was determined by thermal gravimetric analysis (TGA). **Figure 4.4**a shows a TGA plot of the pristine MIL-100(Al)

particles in argon, revealing a progressive weight loss up to ~ 350 ℃, which corresponds to the activation process that removes the trapped solvent molecules and bound H_2O from the MOF. The activated MIL-100(Al) is thermally stable up to 400 ℃ in air (**Figure 4.4**b). The weight loss of 72.5% at 600 ℃ is associated with the oxidation of the MOF, which is in accordance with the reported formula as $Al_3O(OH)(BTC)_2$. So we choose temperature up to 350 ℃ to activate MIL-100(Al), confirming the removal of total bounded water molecules within the structure, which leads to relatively more unsaturated metal sites.[140]

4.1.3 Synthesis of solid-like electrolytes

X-ray diffraction (XRD) pattern of the MOF particles (**Figure 4.5**a) illustrates a crystalline structure, which is well retained after thermal activation at 350 ℃ under vacuum. The major peaks of MIL-100(Al) before and after activation are in good agreement with the simulated pattern of MIL-100(Al).[138] The Fourier-transform infrared spectroscopy (FT-IR) further confirms the structural integrity and presence of OMSs after activation. **Figure 4.5**b compares the spectra of pristine and activated MIL-100(Al), which show little change with respect to the vibrations of MOF skeleton at 1404 cm^{-1} (symmetric vibration of $-COOH_{BTC}$) and 1626 cm^{-1} (coordination bonds of $Al-O_{BTC}$).[134] A shift (from 686 to 690 cm^{-1}) pertaining to metal center ($Al-\mu3-O$) signifies the elimination of bound H_2O on Al^{3+} and emergence of OMSs, which is accompanied by a change in color of MIL-100(Al) from light yellow to dark yellow (**Figure 4.5**c).[141]
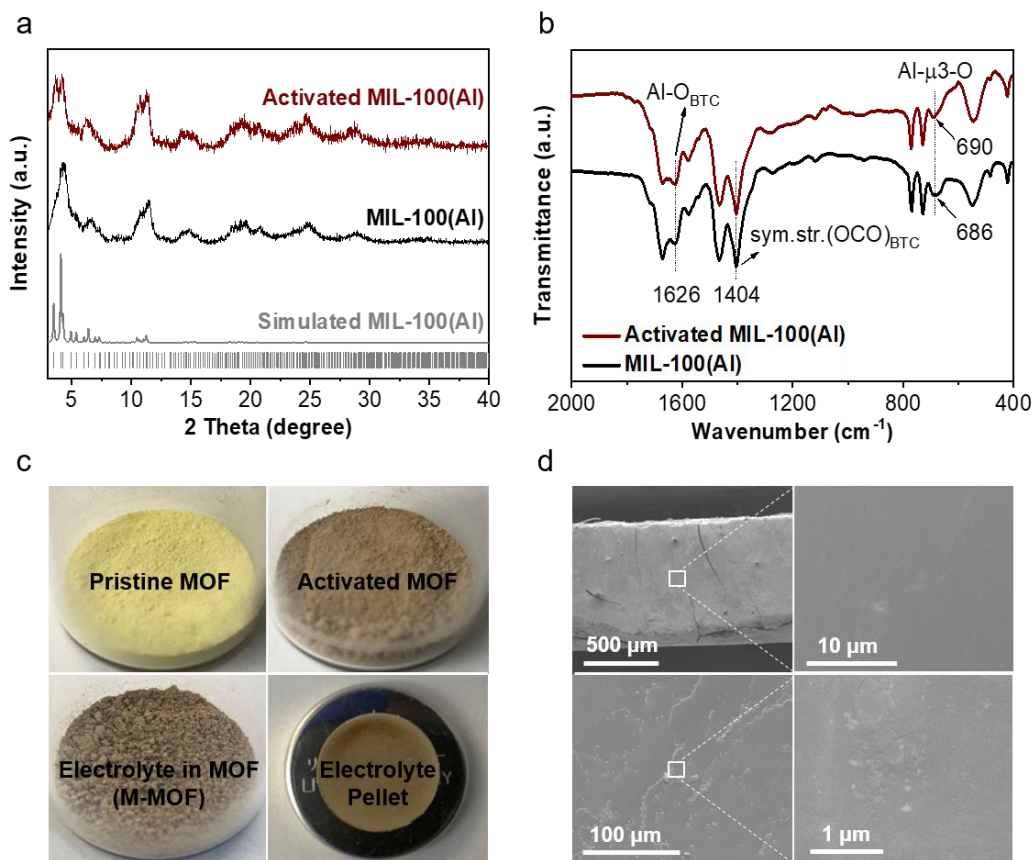
Figure 4.5 (a) X-ray diffraction patterns, and (b) FT-IR spectra of pristine and activated MIL-100(Al). (c) Photographs of pristine, activated, electrolyte-infiltrated MOF particles and an electrolyte pellet. (d) SEM images of an electrolyte pellet (top: cross-sectional view, bottom: in-plane view).

Perchlorate salts (1 M in PC) was used as the liquid electrolytes (denoted as M-PC, where M stands for the cations). The solid-like electrolytes (denoted as M-MOF, where M stands for the cations) were prepared by soaking the activated MOF powders with the liquid electrolytes, following by filtering, and pressing the powders into flow-free electrolyte pellets. SEM images of the electrolyte pellets show absence of macropores from the cross-sectional and in-plane views

(**Figure 4.5**d). The XRD patterns show the crystalline structure of M-MOF is well preserved (**Figure 4.6**).
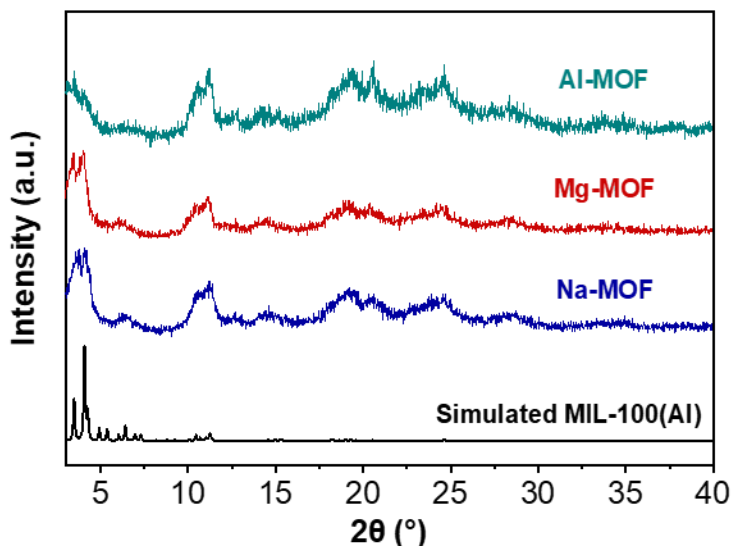
Figure 4.6 X-ray diffraction pattern of simulated MIL-100(Al) and M-MOF (M=Na, Mg and Al).

4.1.4 Ionic conduction mechanisms

The interactions between the MOF scaffold and the infiltrated liquid electrolytes were probed by FT-IR. As shown in **Figure 4.7**a, the FT-IR spectra of the electrolytes (Na-PC, Mg-PC and Al-PC) closely resemble each other except for the carbonyl groups (C=O) of PC at 1790 cm^{-1}, which are sensitive to the solvation status of the cations.[142] Despite the trend of decreasing ionic radii with increasing atomic number within a same period, Na$^+$, Mg^{2+} and Al^{3+} bear increasing solvation with PC due to increasing charge density (increasing Lewis acidity), resulting in the multiple peak shoulders below 1790 cm^{-1} (**Figure 4.7**b). For instance, Na-PC has one dominant peak at 1790 cm^{-1} signifying the solvation of Na$^+$ with PC, Mg-PC shows an additional peak at 1749 cm^{-1},

whereas Al-PC has two peak shoulders at 1742 cm^{-1} and 1708 cm^{-1}, indicating that stronger solvation of the cations with PC is associated with larger charge density of cations.[143-144]
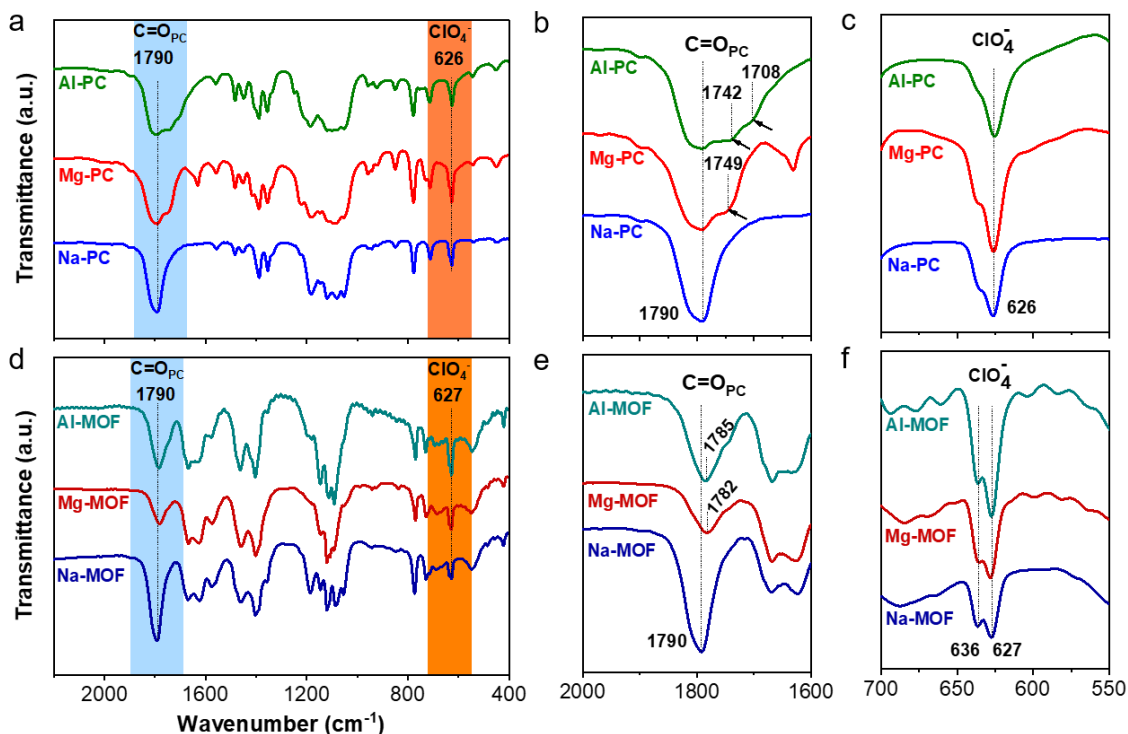
Figure 4.7 (a-c) FT-IR spectra of M-PC. (d-f) FT-IR spectra of M-MOF, M=Na, Mg and Al.

In contrast, the resulted solid-like electrolytes exhibit only one dominant C=O peak. Meanwhile, Mg-MOF shows a C=O peak at 1782 cm^{-1}, which is lower than that of Na-MOF (1790 cm^{-1}) and Al-MOF (1785 cm^{-1}), suggesting a stronger solvation in Mg-MOF compared with Na-MOF and Al-MOF (**Figure 4.7**d-e).[142, 145] Moreover, in M-PC, the peaks at 626 cm^{-1} represent the symmetric vibrations of the ClO$_4^-$ (**Figure 4.7**c),[146] whereas in M-MOF (**Figure 4.7**f), the shoulder peaks at 636 cm^{-1} (asymmetric vibrations of ClO$_4^-$) exhibit more pronounced intensity, suggesting symmetric breakdown of the ClO$_4^-$ anions in presence of MOF due to binding of the ClO$_4^-$ with the OMSs.[135, 145]

4.1.5 Electrolytes performance of M-MOF (M = Na, Mg and Al)

The ionic conductivity of the solid-like electrolytes was measured by electrochemical impedance spectroscopy (EIS). The Nyquist plots of M-MOF (M = Na, Mg and Al) in ambient temperature (**Figure 4.8**a) consist of semi-circles in the high frequency and a linear tail at low frequency region, the intersection of which corresponds to ionic resistance from electrolyte.[70, 91, 147] As a result, Na-MOF, Mg-MOF and Al-MOF afford an ambient ionic conductivity of 0.44, 1.0 and 0.13 mS cm^{-1}, respectively. **Figure 4.8**b shows the temperature-dependent conductivity and corresponding thermal activation energy (E_a) derived from the Arrhenius equation (see the Supporting Information for details), where Mg-MOF shows the smallest E_a (0.20 eV) compared to Na-MOF (0.28 eV) and Al-MOF (0.37 eV). The superionic Mg-MOF with an ionic conductivity of 1.0 mS cm^{-1} and E_a of 0.20 eV is among the best Mg^{2+}-based solid-like conductors thus far reported.[69, 103, 147]
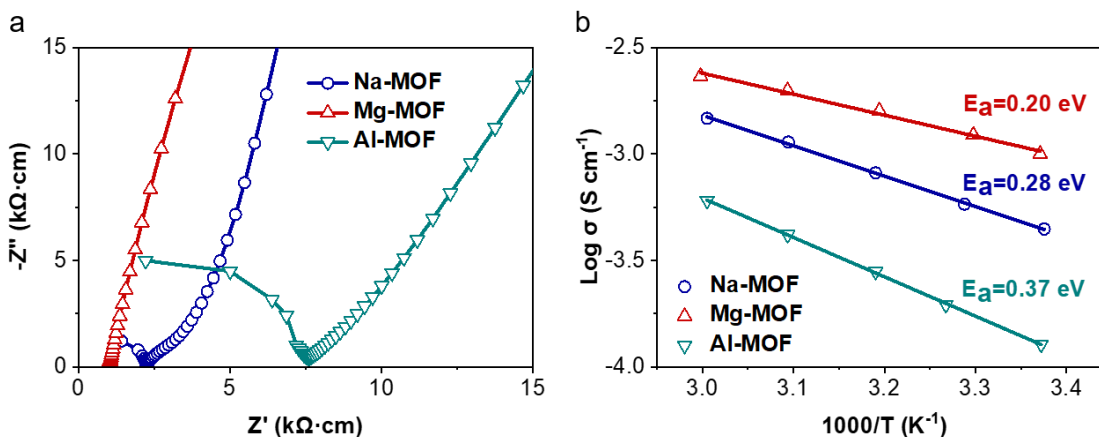
Figure 4.8 (a) Nyquist plots of M-MOF at the ambient temperature. (b) Temperature-dependent conductivities and Arrhenius plots of M-MOF.

To understand the conduction behaviors of M-MOF, conductivities of their liquid-electrolyte counterparts were also investigated. Their ionic conductivities and E_a (**Figure 4.9**) were measured by a similar approach using liquid-electrolyte-soaked separators.
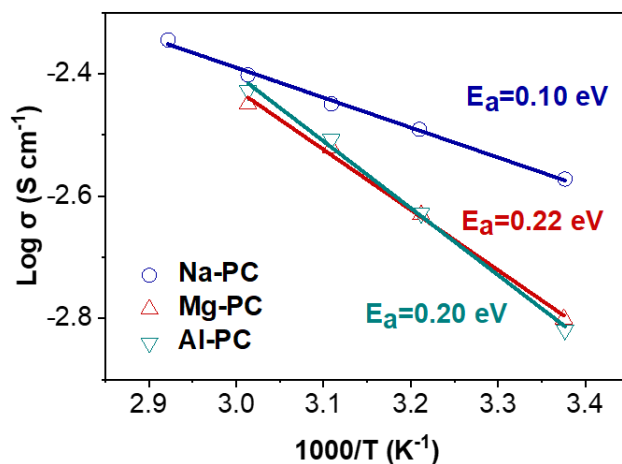
Figure 4.9 Arrhenius plots of M-PC (M=Na, Mg and Al) liquid electrolytes in glass fiber and calculated activation energy for ionic conduction.
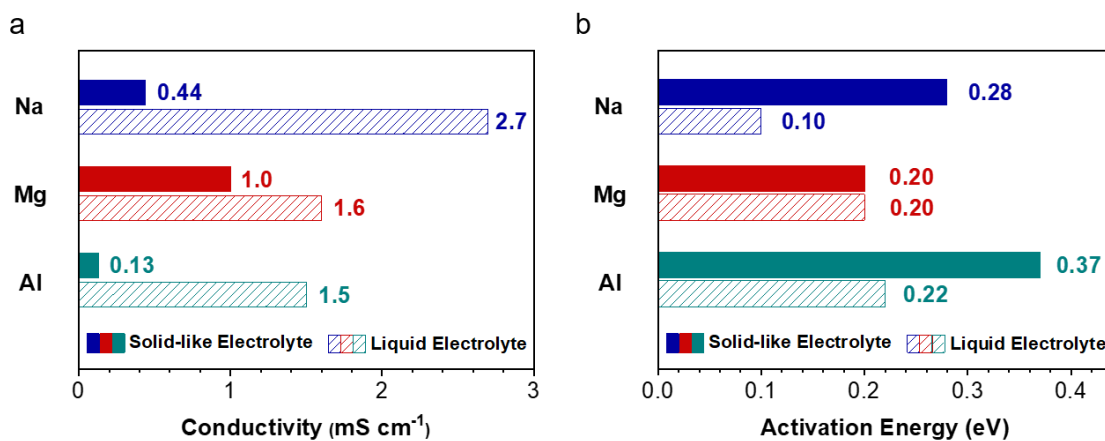
Figure 4.10 (a) Ionic conductivity, and (b) E_a comparisons between M-PC and M-MOF, M = Na, Mg and Al.

As summarized in **Figure 4.10**a-b, a descending ionic conductivity (from 2.7, 1.6 to 1.5 mS cm^{-1}) and ascending E_a (from 0.10, 0.20 to 0.22 eV) are observed for Na-PC, Mg-PC, and Al-PC, respectively. The trend observed in the liquid electrolytes could be interpreted by the intensifying solvent-cation interactions with the increase in charge density, which is consistent with FT-IR results (**Figure 4.10**b). The thickening solvation sheath and increasing electrolyte viscosity could significantly hinder the ion translocation, which reduces the ionic conductivity and increases E_a.[39, 81, 148-149]

4.1.6 Composition of M-MOF (M = Na, Mg and Al)

Compared with the liquid-electrolyte counterparts, M-MOF generally shows reduced ionic conductivity and increased E_a, which is accordance with expectation, as the liquid electrolytes were confined within the nanoporous MOF scaffolds. Nevertheless, as shown in **Table 4**, M-MOF electrolytes all exhibit reasonably high conductivities (> 0.1 mS cm^{-1}) that are sufficient for battery operations.

Table 4 / Composition and ion conduction results of M-MOF and M-PC electrolytes. (M=Na, Mg and Al)

Electrolytes	Estimated composition	Molar concentration of charge carrier	Conductivity (mS cm^{-1})	E_a (eV)
Na-MOF	$Al_3O(OH)(BTC)_2(NaClO_4)_{1.3}$	1.3	0.44	0.28
Mg-MOF	$Al_3O(OH)(BTC)_2(Mg(ClO_4)_2)_{1.6}$	1.6	1.0	0.20
Al-MOF	$Al_3O(OH)(BTC)_2(Al(ClO_4)_3)_{0.8}$	0.8	0.13	0.37
Na-PC	1M $NaClO_4$ in PC	1.0	2.7	0.10
Mg-PC	1M $Mg(ClO_4)_2$ in PC	1.0	1.6	0.20
Al-PC	1M $Al(ClO_4)_3$ in PC	1.0	1.5	0.22

Among the three solid-like electrolytes, Mg-MOF shows the least reduction in ionic conductivity and the least increase in E_a, providing an impressive conductivity of 1.0 mS cm^{-1} and low E_a of 0.20 eV, which are comparable to its liquid counterpart (1.6 mS cm^{-1} and 0.20 eV). For further investigation, the charge-carrier concentration of M-MOF was also determined using TGA and inductively coupled plasma atomic emission spectroscopy (ICP-AES). As shown in **Table 5**, Mg-MOF possesses the highest content of salt (1.6 mol Mg(ClO$_4$)$_2$) compared to Na-MOF (1.3 mol NaClO$_4$) and Al-MOF (0.8 mol Al(ClO$_4$)$_3$) per unit of MOF structure, yielding the highest charge-carrier concentration and thus the highest ionic conductivity.

Table 5 / ICP-IES result of M-MOF (M= Na, Mg and Al) electrolytes

Compound	Na (ppm)	Mg (ppm)	Al (ppm)	Formula
Na-MOF	11.79	-	33.25	Al$_3$O(OH)(BTC)$_2$(NaClO$_4$)$_{1.3}$(PC)$_{7.7}$
Mg-MOF	-	13.72	28.75	Al$_3$O(OH)(BTC)$_2$(Mg(ClO$_4$)$_2$)$_{1.6}$(PC)$_{8.1}$
Al-MOF	-	-	46.20	Al$_3$O(OH)(BTC)$_2$(Al(ClO$_4$)$_3$)$_{0.8}$(PC)$_{8.5}$
MIL-100(Al)	-	-	36.80	-

The selective trapped amounts of cations within the same period possibly arise from the different solvated cations: the increasing charge density in order of Na$^+$, Mg^{2+} and Al^{3+} results in increasing size of solvation sheath and increasing coordination strength between charge carriers and solvents,[81, 84] which leverage with MOF aperture size and acidity of OMSs, respectively. Furthermore, the smaller wavenumber of carbonyl vibrations (PC) in Mg-MOF (**Figure 4.7**e) imply that more PC molecules are involved in solvation than those in Na-MOF and Al-MOF, allowing highly mobile solvated Mg^{2+} to efficiently transport through the anion-complexed MOF channels.[150-151] Taken together, the divalent charge of Mg^{2+}, the high concentration and high mobility of charge carriers in Mg-MOF collectively contribute to its superior ionic conductivity

with low activation energy, which originate from the proper solvated size and strength of Mg^{2+} compared with ClO_4^--complexed porous channels.

The composition of M-MOF was estimated with ICP-AES and TGA in argon. ICP-AES of Mg-MOF illustrates a Mg/Al molar ratio of 0.5, which is consistent with our hypothesis that two OMSs are formed in each Al_3 trimer. In the TGA measurement of Mg-MOF, the initial weight loss (~ 48.4%) up to 353 ℃ is attributed to the removal of PC. The subsequent weight drop originates from decomposition of magnesium salt and disintegration of MOF structure. In the DSC of Mg-PC, the decomposition of $Mg(ClO_4)_2$ involves two processes above 353 ℃, which corresponds to the literature.[152] Based on the calculated molecular weight of Mg-MOF, the nominal formula is determined as as $Al_3O(OH)(BTC)_2(Mg(ClO_4)_2)_{1.6}(PC)_{8.1}$ (see details in **Figure 4.11**). Similarly, the formula of Na-MOF and Al-MOF are calculated as $Al_3O(OH)(BTC)_2(NaClO_4)_{1.3}(PC)_{7.7}$ and $Al_3O(OH)(BTC)_2(Al(ClO_4)_3)_{0.8}(PC)_{8.5}$ (**Figure 4.12-13**).
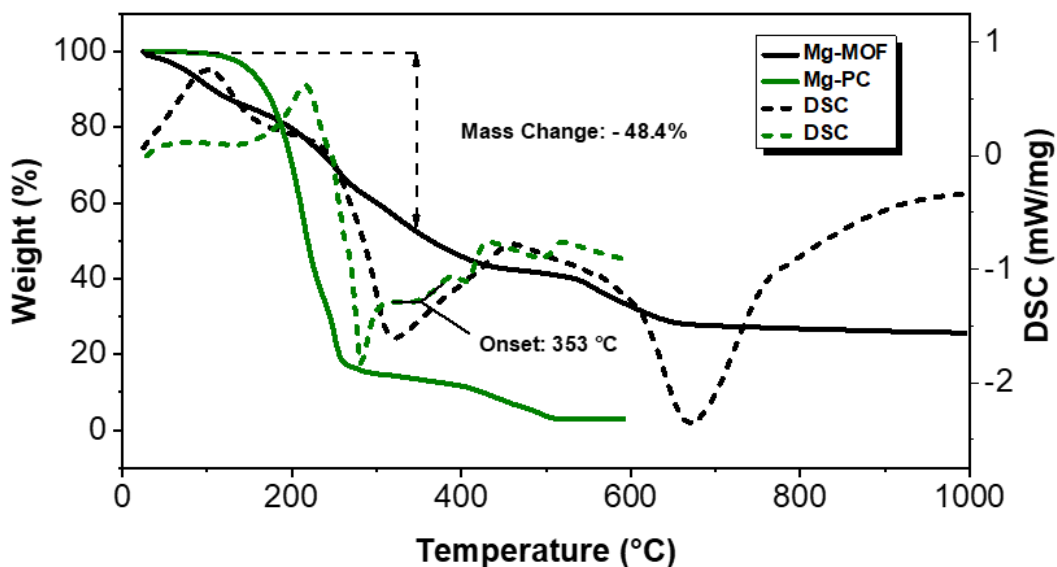
Figure 4.11 TGA plot for Mg-MOF and Mg-PC electrolytes in argon.
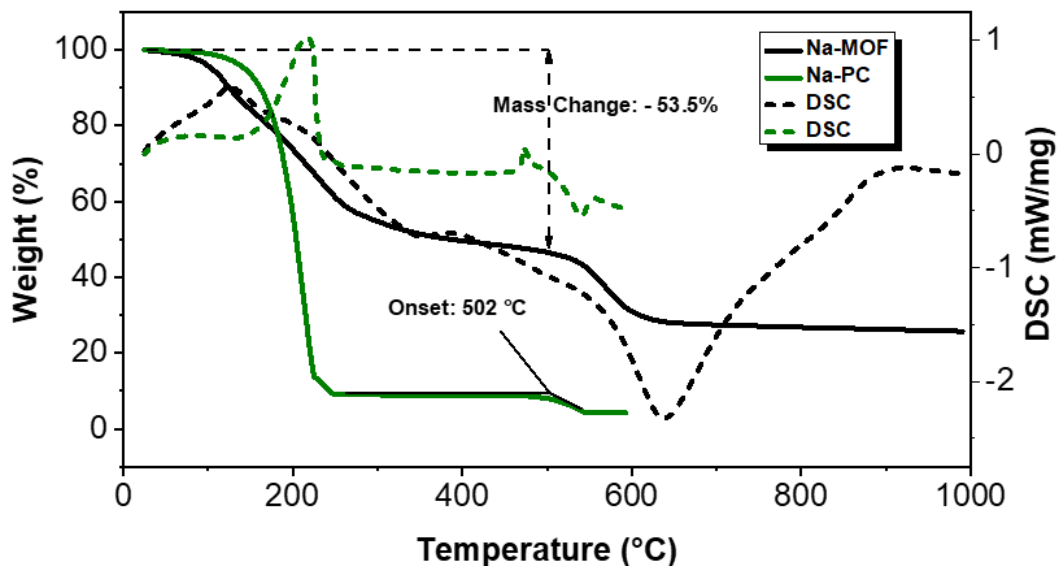
Figure 4.12 TGA plot for Na-MOF and Na-PC electrolytes in argon.

In the TGA measurement of Na-MOF, the initial weight loss (~ 53.5%) up to 502 °C is attributed to the removal of PC. The subsequent weight drop originates from decomposition of sodium salt and disintegration of MOF structure. In the DSC of Na-PC, we can see a fusion at 469 °C and a decomposition of $NaClO_4$ at around 505 °C, which corresponds to the literature.[153] Based on the calculated molecular weight of Na-MOF, the nominal formula is determined as $Al_3O(OH)(BTC)_2(NaClO_4)_{1.3}(PC)_{7.7}$.
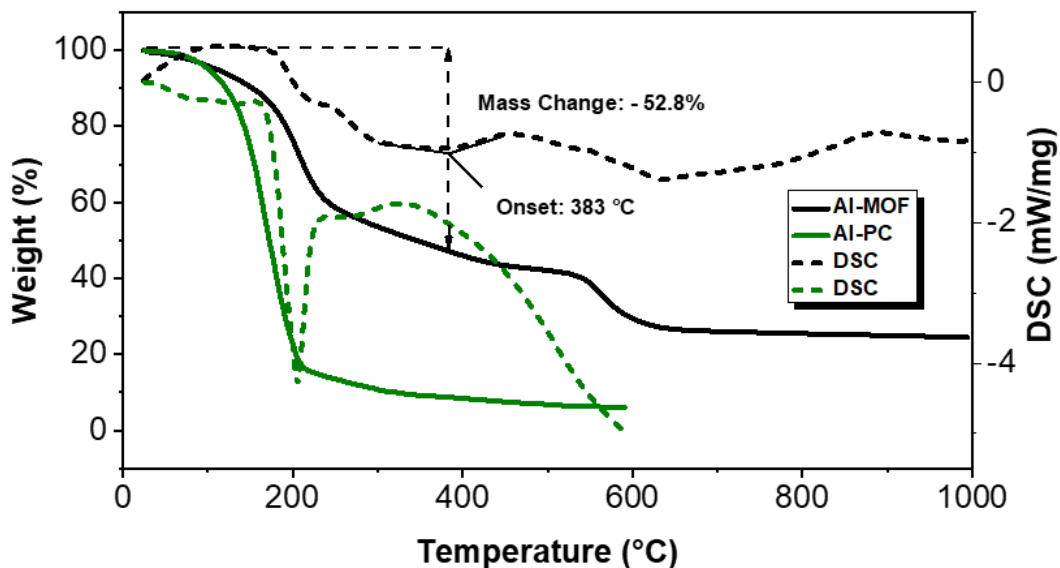
Figure 4.13 TGA plot for Al-MOF and Al-PC electrolytes in argon.

Based on the Al content from the reference MIL-100(Al) in **Table 5**, we estimated the guest per mole MOF in Al-MOF by subtracting the Al in MOF. In the TGA measurement of Al-MOF, the initial weight loss ($\sim 52.8\%$) up to 383 ℃ is attributed to the removal of PC. The subsequent weight drop originates from disintegration of MOF structure and decomposition of aluminum salt. Based on the calculated molecular weight of Al-MOF, the nominal formula is determined as $Al_3O(OH)(BTC)_2(Al(ClO_4)_3)_{0.8}(PC)_{8.5}$.

4.1.7 Electrolytes performance of M-MOF (M = Li⁺, Na⁺, K⁺ and Cs⁺)

As mentioned above, Na^+, Mg^{2+} and Al^{3+} ions are in the same period with reducing radii and increasing charge density. Though the explicit conduction mechanism of the present system is complicated and still elusive, we further validated our design by infiltrating MIL-100(Al) with liquid electrolytes containing cations from a same group (Li^+, Na^+, K^+ and Cs^+), where the cations share the same charge but with increasing radii and decreasing solvated size.[38, 80] Herein, 1M

perchloride-salt electrolytes in dimethyl sulfoxide (DMSO) was used (denoted as M-DMSO, where M = Li, Na, K and Cs) due to the low solubility of $KClO_4$ and $CsClO_4$ in PC.[154]

The conductivity of M-DMSO was first measured and shown in **Figure 4.14**. With increasing the ionic radii and decreasing charge density, Li^+, Na^+, K^+ and Cs^+ ions in DMSO were reported with decreasing solvated size of 0.318, 0.303, 0.291 and 0.246 nm, respectively.[38, 155] Consistently, Li-DMSO, Na-DMSO, K-DMSO and Cs-DMSO show an increasing ionic conductivity of 4.6, 5.7, 6.1, and 6.5 mS cm^{-1}, respectively.[156-157]
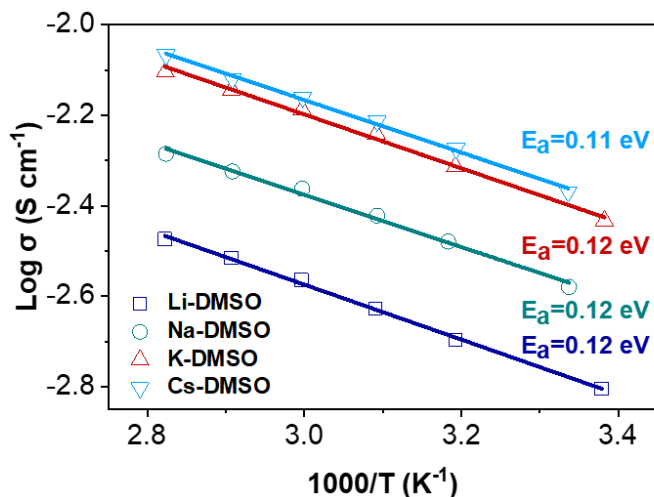
Figure 4.14 Arrhenius plots of M-DMSO (M = Li, Na, K and Cs) liquid electrolytes in glass fiber and calculated activation energy for ionic conduction.
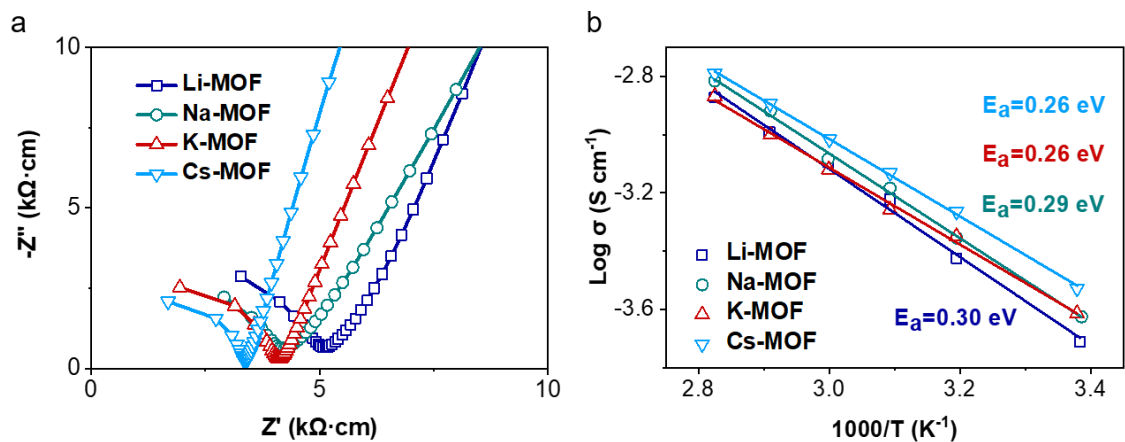
Figure 4.15 (a) Nyquist plots of M-MOF at the ambient temperature. (b) Temperature-dependent conductivities and Arrhenius plots of M-MOF.

Figure 4.15a and **Figure 4.15**b present the Nyquist plots and temperature-dependent conductivity of the corresponding solid-like electrolytes (denoted similarly as M-MOF, M = Li, Na, K and Cs), respectively.
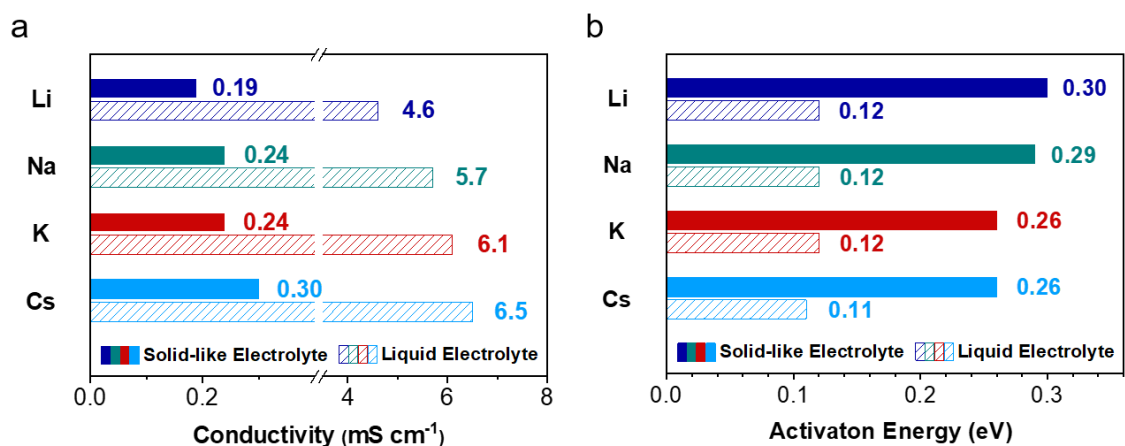
Figure 4.16 (a) Ionic conductivity, and (b) E_a comparisons between M-PC and M-MOF, M = Li, Na, K and Cs.

The ambient conductivities and E_a of the electrolytes are also compared in **Figure 4.16**a and **Figure 4.16**b, respectively. Confining the liquid electrolytes within the MOFs results in M-MOF

with decreased conductivities and increased E_a, which is similar to that observed in **Figure 4.8**. Meanwhile, the conductivity of M-MOFs also increases from Li^+, Na^+, K^+ to Cs^+. Unlike the solvated cations from the 3rd period (Na^+, Mg^{2+} and Al^{3+}), the monovalent cations from the 1st group show small variation in terms of solvation size (see a summary in **Table 6**). Infused with such electrolytes in MOF yields similar trends of ion conduction behaviors like their liquid counterparts.

Table 6 / Ionic radii and Stokes' radii of cations in different solvents

	r_i (nm)[158]	DMSO r_s (nm)[155]	PC r_s (nm)[155]	PC r_s (nm)[80]	H_2O r_s (nm)[159]	H_2O r_s (nm)[160]
Li	0.068	0.318	0.337	0.48		0.238
Na	0.097	0.303	0.310	0.46	0.183	0.184
K	0.133	0.291	0.275	0.36	0.124	0.125
Cs	0.167	0.246	0.220	-		0.119
Na	0.097				0.183	
Mg	0.066				0.345	
Al	0.051					

4.2 Feasibility of solid-like electrolytes in battery applications

4.2.1 MOF/PTFE membrane electrolytes

To assess the feasibility and superiority of such solid-like electrolytes for battery applications, free-standing membrane separators for hosting liquid electrolytes were fabricated by activated MOF powders and polytetrafluoroethylene (PTFE) binder. The membranes (denoted as MOF/PTFE) soaked with 1M $LiClO_4$ in PC and 1M $NaClO_4$ in PC show comparable ionic conductivity and activation energy with their liquid counterparts (**Figure 4.17**).
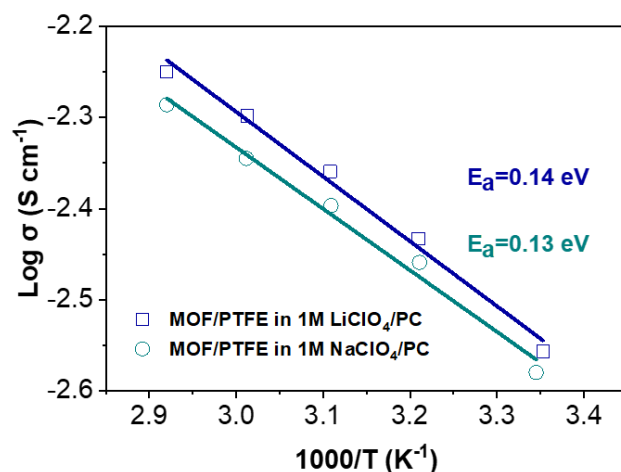
Figure 4.17 Arrhenius plots and derived activation energy of solid-like electrolyte membranes.

The electrochemical stability windows of such solid-like electrolyte membranes were examined by cyclic voltammetry (CV) tests using stainless steel as working electrodes. The results (**Figure 4.18**) indicate reversible Li^+/Na^+ stripping-plating processes on steel electrodes and anionic stability up to 4.5 V (*vs.* Li/Li^+ or Na/Na^+).
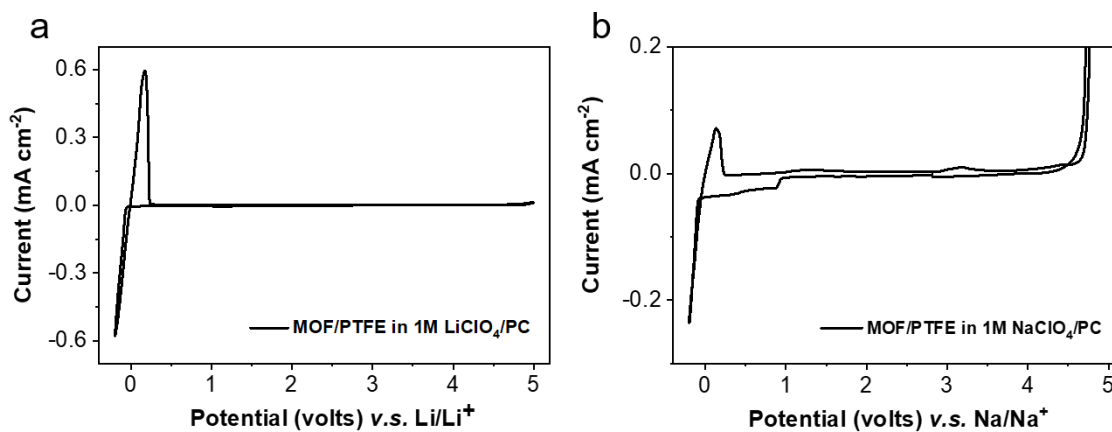
Figure 4.18 CV curves of MOF/PTFE using electrolytes of (a) 1M $LiClO_4$ in PC and (b) 1M $NaClO_4$ in PC.

69

The lithium-ion transference number (t_{Li}^+) and sodium-ion transference number (t_{Na}^+) were measured using the potentiostatic polarization method.[86] The anion-immobilizing MOF particles notably improves the cation-transference numbers higher than 0.5 (**Figure 4.19**a-b, $t_{Li}^+ \approx 0.7$, $t_{Na}^+ \approx 0.5$) relative to a typical value of 0.3 from the liquid electrolytes,[161-162] confirming the role of OMSs on selectively tuning ion transport behaviors.
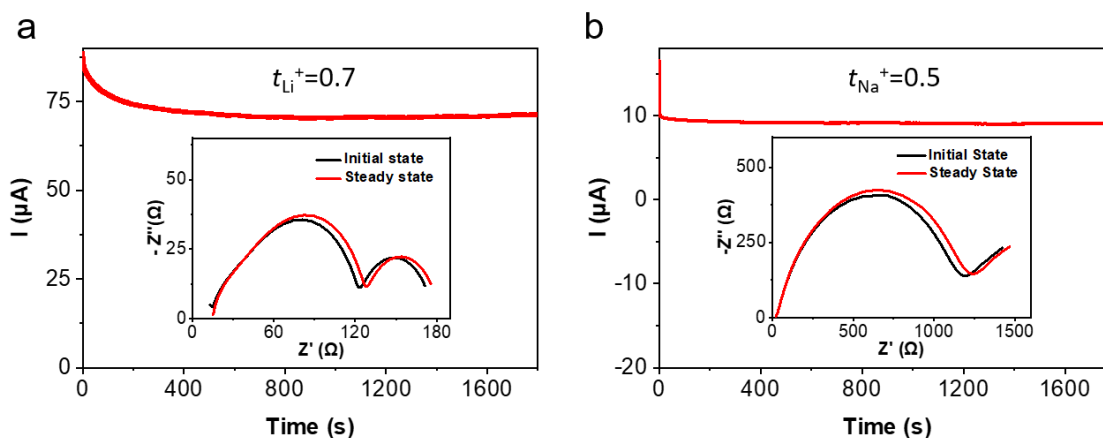
Figure 4.19 Measurements of cation-transference number of MOF/PTFE membrane separators in (a) 1M LiClO$_4$ in PC and (b) 1M NaClO$_4$ in PC.

Galvanostatic cycling of symmetric cells using two identical lithium electrodes and 1M LiClO$_4$ in PC were performed to characterize the long-term stability of MOF against lithium metal. As shown in **Figure 4.20**, the cell using MOF/PTFE exhibits well-maintained overpotential below 30 mV and regular stepwise voltage curves up to 600 hours (300 cycles), suggesting an exceptional electrochemical stability. In comparison, the cell with a commercial separator shows higher overpotential escalating from 50 mV up to 300 mV throughout the test, which could be ascribed to the resistive and unstable interfaces formed in liquid electrolyte.[163]
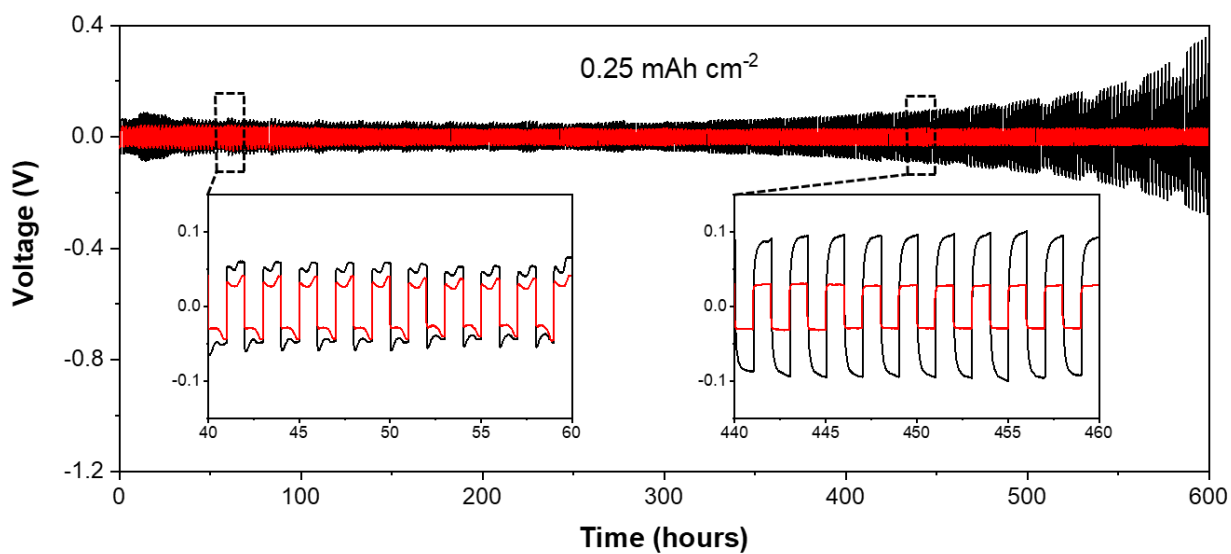
Figure 4.20 Galvanostatic cycling of lithium symmetric cells under current density of 0.25 mAh cm^{-2} and time interval of 1 hour. (MOF/PTFE membrane, red; PP separator, black)

4.2.2 MOF/PVDF-HFP for sodium-metal batteries

To date, most MOF-based solid-like electrolytes focus on lithium-metal batteries as Chapter 1.6 shown. While rare research explored the field of sodium-metal batteries with MOF-based solid-like electrolytes. As we know, the scarcity and uneven distribution of lithium only accounts for 0.0065% of the Earth's crust, which poses challenges to the future development of the energy industry as a result of the shortfall and high price of the raw material. Given the sixth richest element on the earth (about 2.74%) and shared physical as well as chemical properties with Li in many aspects, Na is featured as a promising candidate to substitute Li in large-scale energy storage devices.[164] Hence, we expanded the application of MOF-based solid-like electrolytes from lithium to sodium metal batteries, demonstrating a large application potential for the family of MOF-based solid-like electrolytes.

71

4.2.2.1 Cathode for sodium-metal batteries

Cathodic materials play an important role in achieving exceptional Na storage performance because cathodic materials not only share a large mass fraction in batteries, but also dominate the operating voltage ranges. As a result, cathodic materials determine the cost, safety, specific energy, and specific power of sodium-ion batteries. Here, we choose the $Na_3V_2(PO_4)_3$ (NVP) with a NASICON structure as the cathodic material for Na-metal batteries. NVP with stable 3D host framework possesses better thermal stability, longer cycle life and better safety features among various cathodic materials. The electrochemical voltage-composition curve for sodiation and desodiation reactions in NVP is shown in **Figure 4.21**.[165]
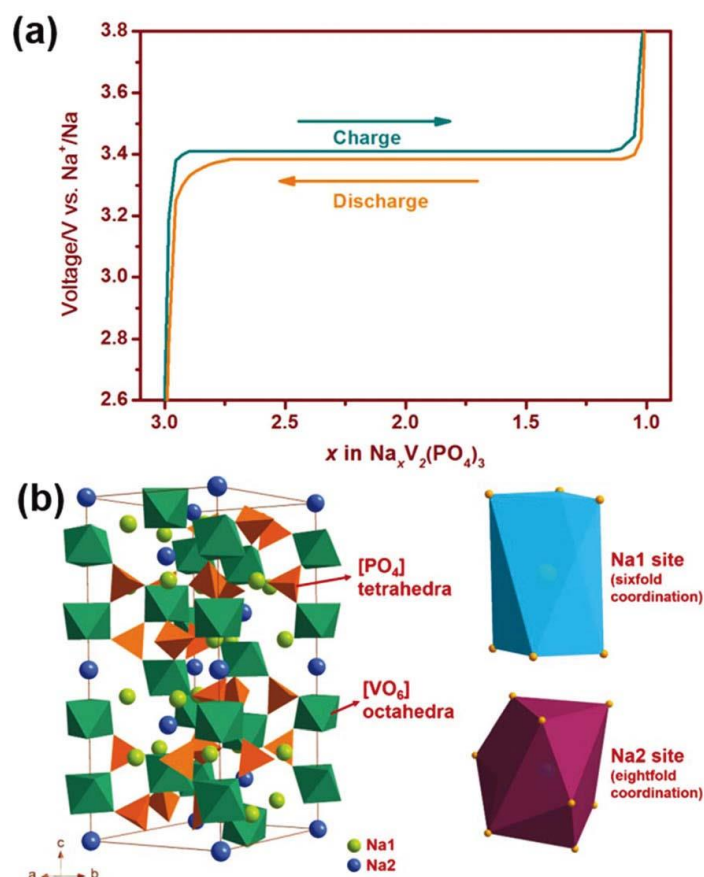
Figure 4.21 (a) Electrochemical voltage–composition curve of the NVP cathode. (b) Crystal structure of rhombohedral NVP.[165]

NVP exhibits a very flat voltage plateau located at around 3.4 V *vs.* Na$^+$/Na, which is associated with the V^{3+}/V^{4+} redox couple, corresponding to the two-phase transition reaction (Na$_3$V$_2$(PO$_4$)$_3$ ↔ NaV$_2$(PO$_4$)$_3$. As a result, a theoretical capacity of 118 mAh g^{-1} is presented. The 3D NASICON-type crystal structure of NVP is shown in **Figure 4.21**b.

4.2.2.2 Synthesis of NVP/C and characterization

Although NVP holds many advantages, it suffers from the key drawback of inferior intrinsic electronic conductivity (1.63×10^{-6} S cm^{-1}) and poor ion diffusivity.[166] To address these problems, researchers have explored many approaches, mainly focus on surface-conducting modification (e.g., carbon coating), elemental doping and downsizing the NVP particles. Here, we choose a simple wet-ball-milling and in-situ carbon-coating process to synthesis NVP/C cathode material.[130]
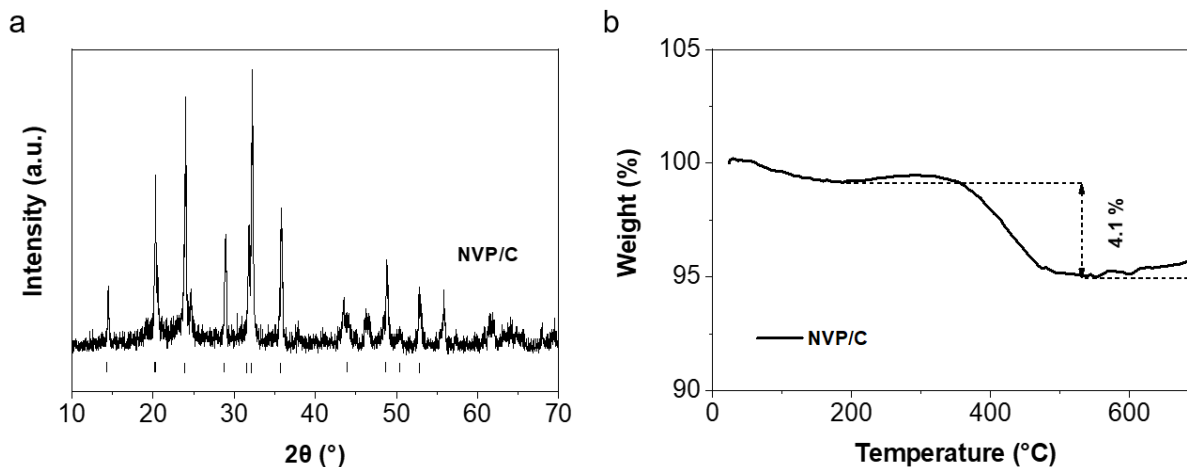
Figure 4.22 (a) X-ray diffraction pattern of NVP/C. (b) TGA plot for NVP/C in air.

As **Figure 4.22** shown, the crystal structure of synthesized NVP/C is well consistent with theoretical pattern (JCPDS card No.00–053–0018) and TGA plot indicates a carbon coating of 4.1 % weight is obtained. Wet-ball-milling method is expected to reduce the size of the primary

particles and increase the specific surface area with a beneficial effect of the carbon coating. Thus, SEM images of NVP/C show a decrease of the aggregation of the particles and the size of primary particles. The thermal treatment not only ensures the completion of the solid-state reaction but also contributes to the relaxation of the strain induced by the ball-milling process. After annealing treatment, the NVP/C particle show a porous structure, this could enlarge the interfacial contact between the electrolyte and the electrode and, hence, facilitate the Na^+ accessibility to the host framework.[130]

a

b
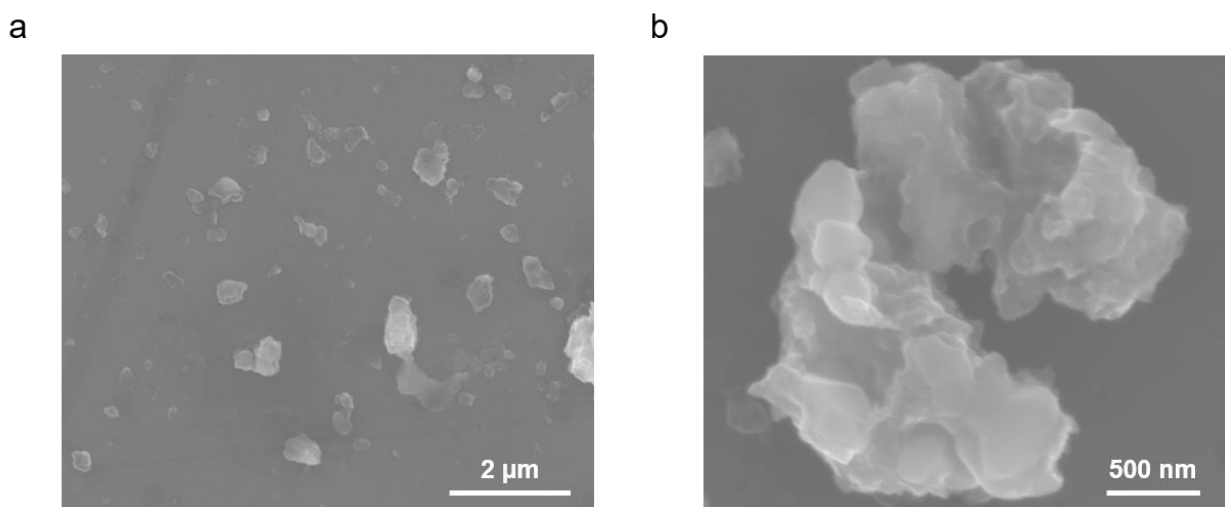
Figure 4.23 SEM (a and b) images of NVP/C particles.

4.2.2.3 Electrochemical performance

During the test for sodium-ion transference number, we noticed an unstable SEI formed on the surface of sodium, which caused larger interfacial resistance in **Figure 4.19**b. This effect could cause unstable side reaction and thus, lead to a short battery life when we use MOF/PTFE in sodium metal batteries. Specificlly, sodium in intimate contact with PTFE polymer leads to surface defluorination and NaF formation.[167] In order to get a stable battery performance, we use PVDF-HFP as the polymer for the following electrochemical performance tests.

74

In the beginning, we compared the 50% MOF-GF with pure GF in different rate using 1 M NaClO$_4$ in EC/PC (vol 1:1) with 5% FEC as the electrolyte. Here, FEC is Fluoroethylene Carbonate, an effective additive to improve the performance of Na-ion batteries.[168] As shown in **Figure 4.24**a, 50% MOF-GF exhibits an intial capacity of 91 mAh g^{-1} at 0.5 C (1 C = 118 mA g^{-1}) and reversible capacities of 90, 86, 79, 65, 55 and 42 mAh g^{-1} at 0.5, 1, 2, 5, 10 and 20 C rates, respectively. **Figure 4.24**b compared the cycling performance at 2 C. 50% MOF-GF presents an average Columbic efficiency (CE) of 99.8% at first 200 cycles, while GF only delivers 96.5% average CE and a continued decreasing of CE after 200 cycles.
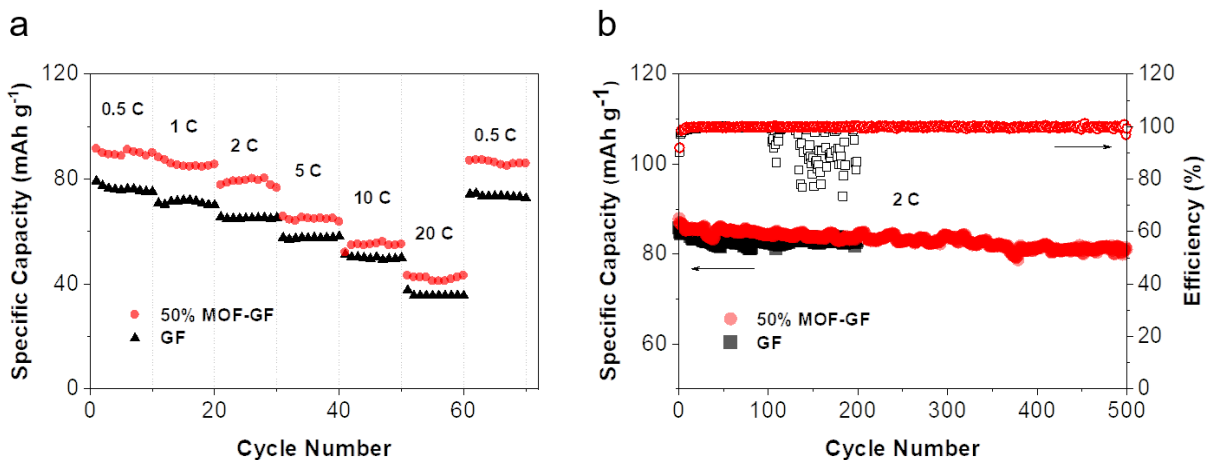
Figure 4.24 (a) Rate performance at 0.5 C, 1 C, 2 C, 5 C, 10 C, 20 C, and 0.5 C rates. (b) Galvanostatic cycling performance at 2 C, the empty symbols represent the Columbic efficiency.

To further show the advantages of MOF-polymer composite electrolyte, we compared the 50% MOF-GF with 0% MOF-GF using 1 M NaClO$_4$ in PC with no FEC as the electrolyte. As shown in **Figure 4.25**a, stepped rates were performed in consecutive manner from 0.5 C up to 20 C. Both cells show comparable specific capacity above 80 mAh g^{-1} at 0.5 C, signifying analogous cell resistance at low rate. However, the advantage of MOF in reducing anion mobility and concentration polarization is amplified in high-rate operation.[147] An evident discrepancy was

observed at relatively high rate of 20 C (**Figure 4.25**b), where the cell using reference separator

delivers no capacity while the one with MOF-modified separator could still achieve 40 mAh g^{-1}.
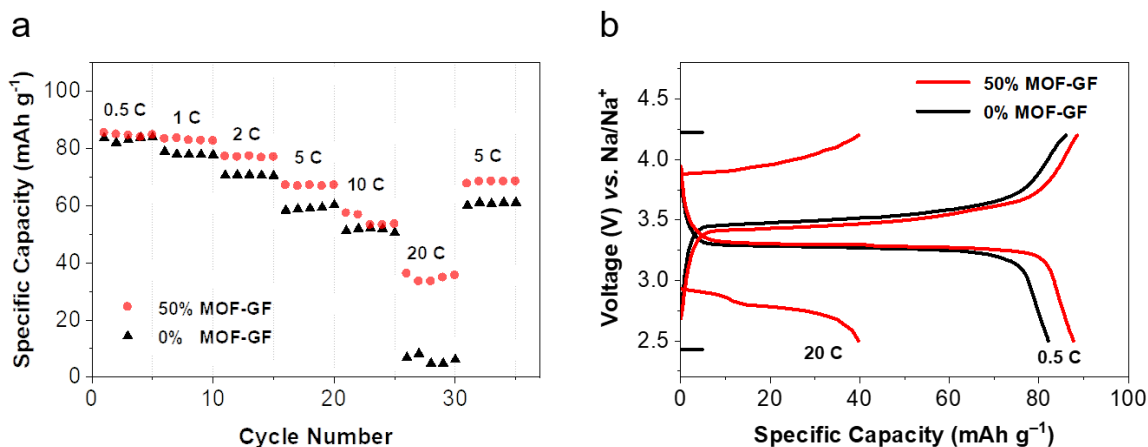
Figure 4.25 NVP|Na cells with MOF-modified and reference separator: (a) Rate performance at

0.5 C, 1 C, 2 C, 5 C, 10 C, 20 C. (b) Voltage-capacity plots at 0.5 C and 20 C.
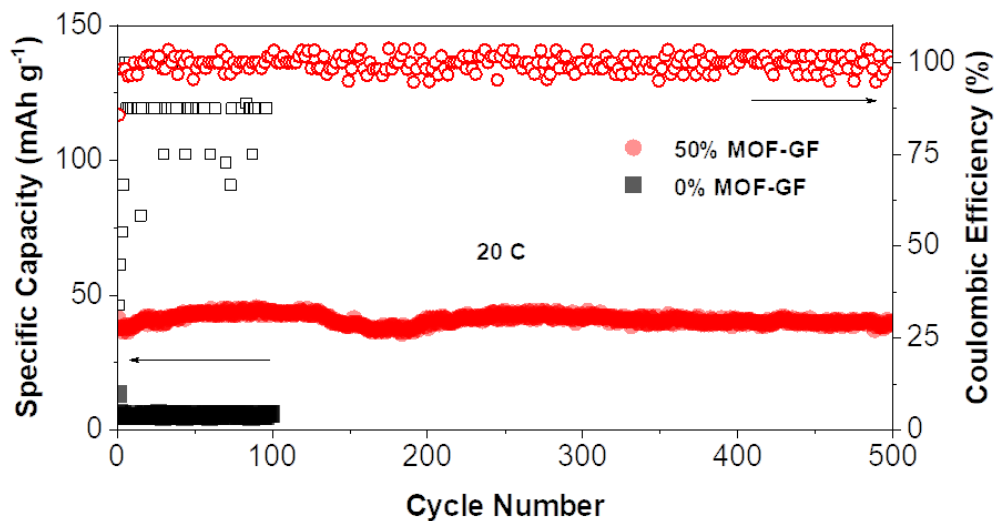
Figure 4.26 Galvanostatic cycling of NVP|Na cells at 20 C.

Moreover, the subsequent durability test at 20 C (**Figure 4.26**) clearly confirmed the exceptional

stability of MOF-modified separator. Besides, the CE of 50% MOF-GF is much higher than that

of 0% MOF-GF. The result indicates that MOF particles play an important role in MOF-polymer functional separator, leads to significantly improved rate performance and the columbic efficiency.

Furthermore, several wt% (0%, 25%, 50% and 75%) MOF were directly used as solid-like polymer gel electrolytes without GF in Na-metal batteries, in which 75% MOF exhibits the best Columbic efficiency (**Figure 4.27**).
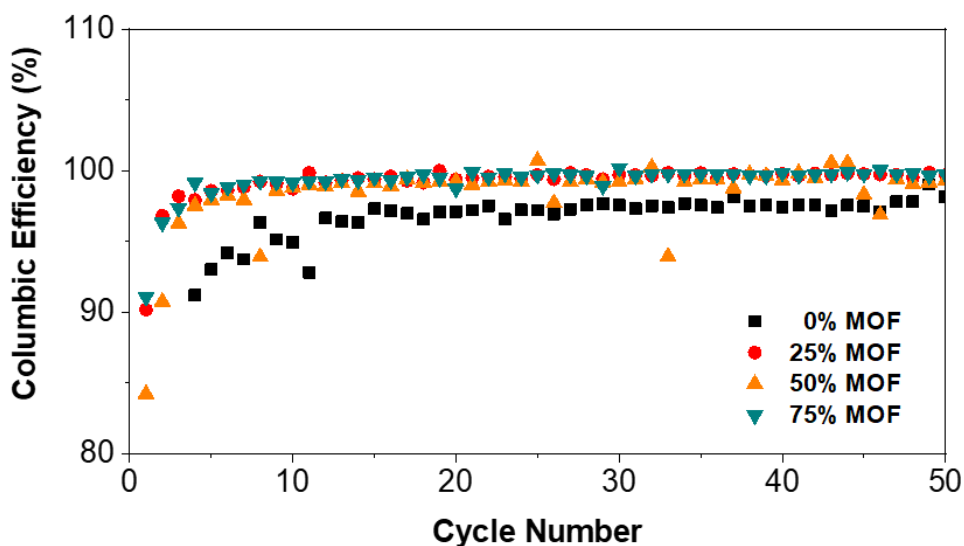
Figure 4.27 Columbic efficiency of different wt% MOF as polymer gel electrolytes in NVP|Na cells at 0.5 C.

In another approach, solid-like Na-metal batteries (NVP|Na) were assembled by coating MOF-based gel electrolyte (75% MOF) on Na anode. As shown in **Figure 4.28**a, galvanostatic cycling of the cells was compared using MOF-based gel electrolyte and liquid electrolyte (Na-PC). The cell using solid-like electrolyte notably surpasses the cell using liquid electrolyte in terms of cycle stability and Coulombic efficiency. The degrading capacity and Coulombic efficiency from the cell with liquid electrolyte indicate its poor cycle reversibility and interfacial stability (**Figure**

4.28b). Therefore, confining liquid electrolyte and complexing respective anions by MOFs substantially tackle the issues of cell polarization and interfacial stability.
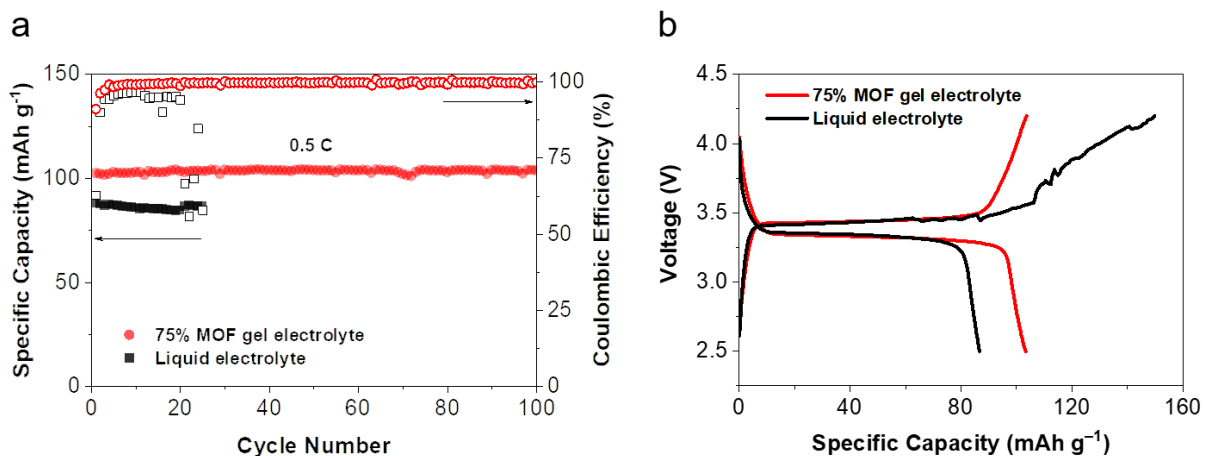
Figure 4.28 (a) Galvanostatic cycling performance of 75% MOF compared with PP at 0.5 C. The empty symbols represent the Columbic efficiency. (b) Charge–discharge curves of 75% MOF compared with PP at 0.5 C (25th cycle).

4.3 Attempt of MOF-based solid-like electrolytes in Li-S batteries

4.3.1 Design and synthesis of suitable MOF structure

In order to inhibit the major issue "shuttle effect" in Li-S batteries, we designed a modification to the metal centers in MOF structure. As we know, Al^{3+} is a strong Lewis acid to react with polysulfides anion (S_x^{2-}). So, we choose MIL-100(Cr) as our designable MOF material. Inspired by Nafion with sulfonated moieties ($-SO_3^-$), which may block the diffusion of polysulfides anions through electrostatic repulsion.[169] As shown in **Figure 4.29**, we use a small molecule HS-CH$_2$-CH$_2$-SO$_3$Na (MeSNa) to interact with the OMSs in MIL-100(Cr), leaving SO$_3^-$ groups outside to prevent LiS$_x$ from reacting with metal centers and may also inhibit the diffusion of polysulfides anions.
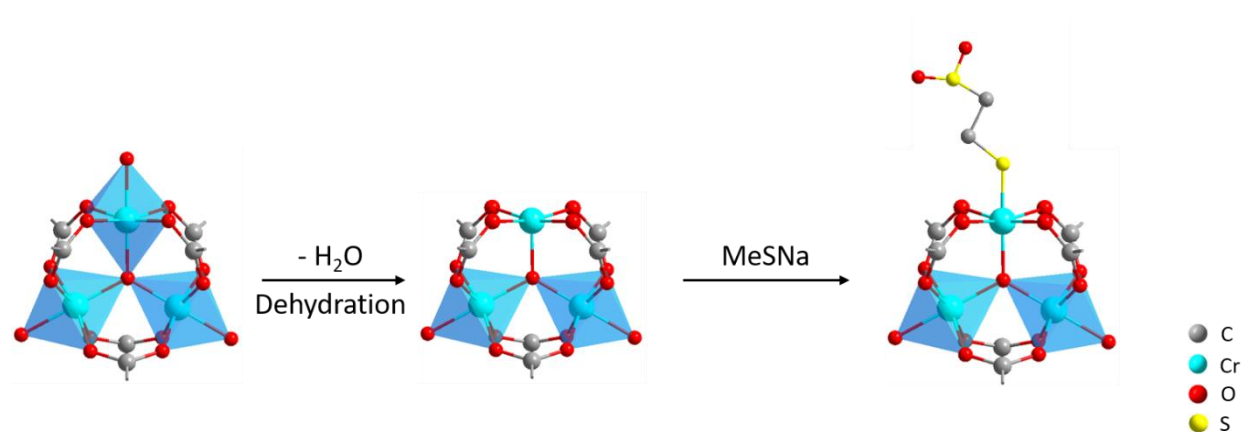
Figure 4.29 Illustration of MIL-100(Cr) OMSs modification.

MIL-100(Cr) was synthesized using a similar green microwave-assisted method,[129] which use water as solvent without any acid. After purification, the MIL-100(Cr) particles were ball-milled to get smaller particle size, then activated at 200 ℃ to remove the trapped solvent molecules and bound H_2O from the MOF. After reacting with MeSNa, MOF particles were exchanged with LiTFSI then washed by DMSO.

X-ray diffraction (XRD) pattern of the MOF particles (**Figure 4.30**) illustrates a crystalline structure, which is well retained after thermal activation at 200 ℃ under vacuum. After reacting with MeSNa, the crystallinity of MOF particles decreases slightly due to the interaction between MeSNa and OMSs in the MOF (denoted as MIL-100(Cr)-SH). The obtained particles were stable after treated in water, this benefits the following processes regarding the synthesis of solid-like electrolytes.
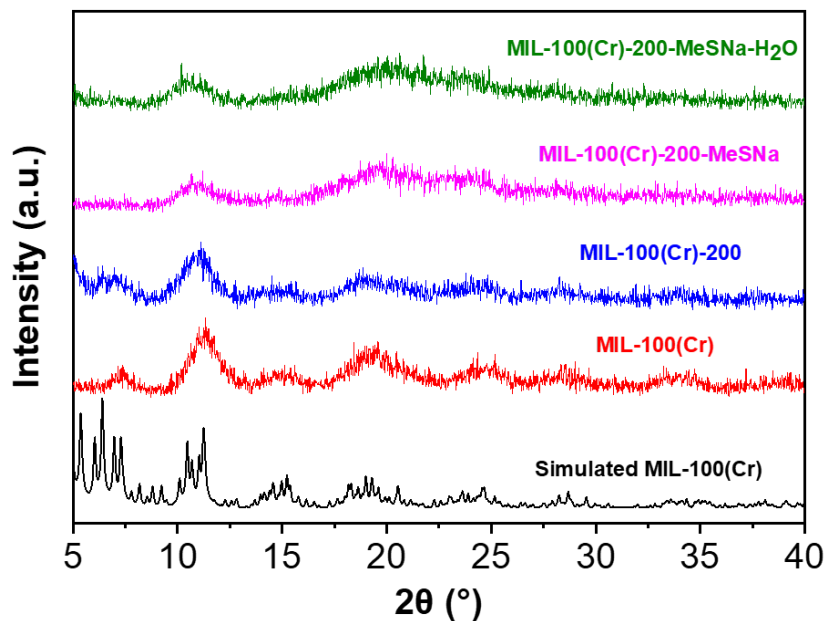
Figure 4.30 X-ray diffraction patterns of pristine, activated MIL-100(Cr), MIL-100(Cr)-MeSNa and MIL-100(Cr)-MeSNa treated in water.

   To confirm the content of MIL-100(Cr)-SH, we use TGA and XPS for analysis. **Figure 4.31** shows a weight loss of MIL-100(Cr)-SH after 100 ℃ compared with activated MIL-100(Cr). The weight loss difference is about 30%, which is in consistence with the theoretical molecular weight of two MeSNa coordinated to two OMSs in one Cr_3O trimer.
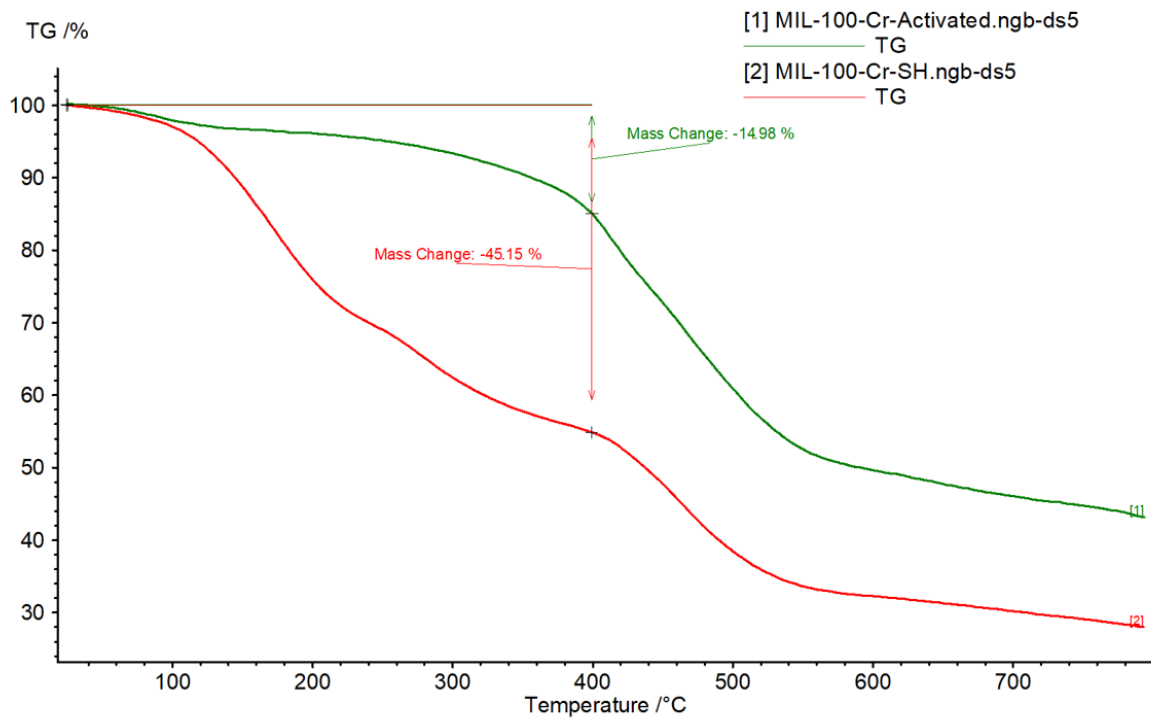
Figure 4.31 TGA plot for activated MIL-100(Cr) and MIL-100(Cr)-SH in argon.
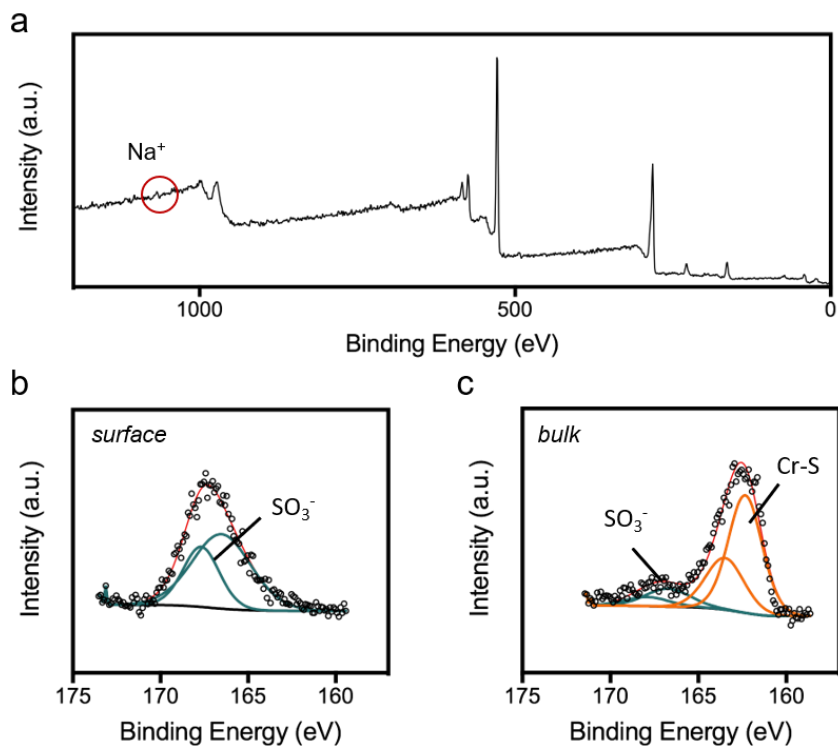
Figure 4.32 Interaction between Cr-S probed by XPS. (a) Survey scan of MIL-100(Cr)-SH. (b) Sulfur 2p core spectra on the surface of MIL-100(Cr)-SH. (c) Sulfur 2p core spectra on the bulk of MIL-100(Cr)-SH.

The survey scan of MIL-100(Cr)-SH showed in **Figure 4.32**a, indicates no sign of Na^+ from MeSNa. **Figure 4.32**b presents S 2p spectra on the surface MIL-100(Cr)-SH, the position of the S $2p_{3/2}$ peak was assigned to the sulfonic signal at around 167 eV.[170] The bulk of MIL-100(Cr)-SH was obtained using ion gun (3.8 KV) for 3 min. As **Figure 4.32**c shown, the position of the S $2p_{3/2}$ peak was assigned to the bound thiol (Cr-S).[171] The XPS result is in accordance with our structure design that thiol group (SH) was coordinated to the OMSs (Cr) in MOF, leaving SO_3^- groups outside at the surface of MIL-100(Cr)-SH.

4.3.2 Stability against lithium polysulfide

Before the electrochemical performance tests, we perform a simple stability test by soaking activated MIL-100(Cr) and MIL-100(Cr)-SH in 0.1 M Li_2S_6. As shown in **Figure 4.33**a, activated MIL-100(Cr) shows a clear color fade after centrifugation, indicating an adsorption of Li_2S_6 into MOF framework. In comparation, modified MIL-100(Cr) exhibits nearly no color change compared with pure Li_2S_6 due to the preemption of SH coordinated to the OMSs in MOF, which prevent further interaction between Cr in MOF and Li_2S_6. Although there is no major XRD peak changes after soaking in Li_2S_6 (**Figure 4.33**b), we claimed that MIL-100(Cr)-SH holds the ability to inhibit polysulfide from reacting with metal centers in MOF.
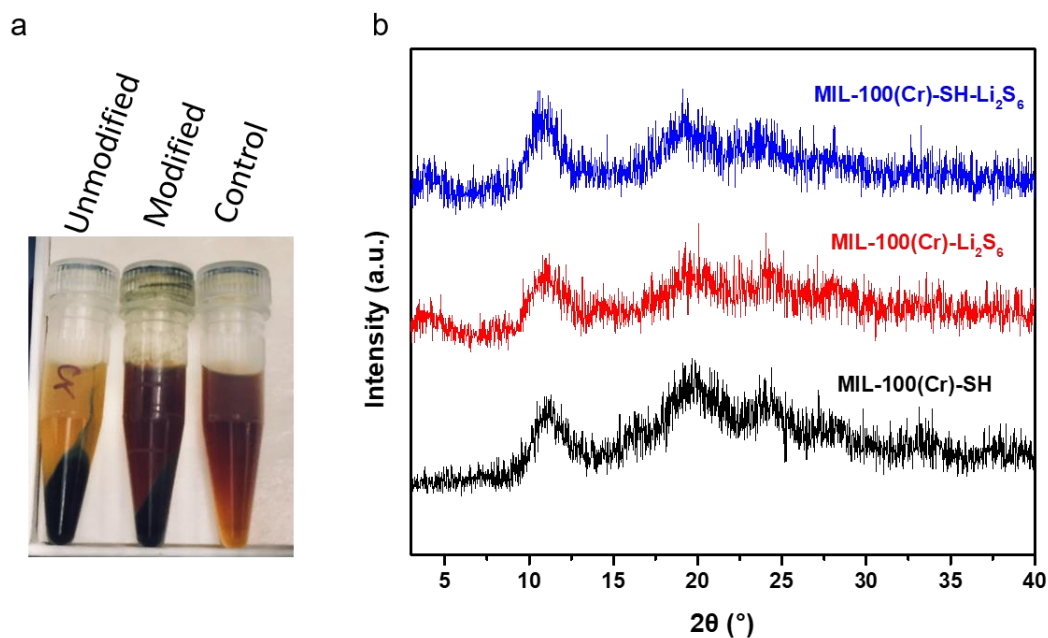
Figure 4.33 (a) Photograph of soaking activated MIL-100(Cr), MIL-100(Cr)-SH in 0.1 M Li$_2$S$_6$ compared with pure Li after centrifugation. (b) XRD patterns of MOF particles after the soaking process.
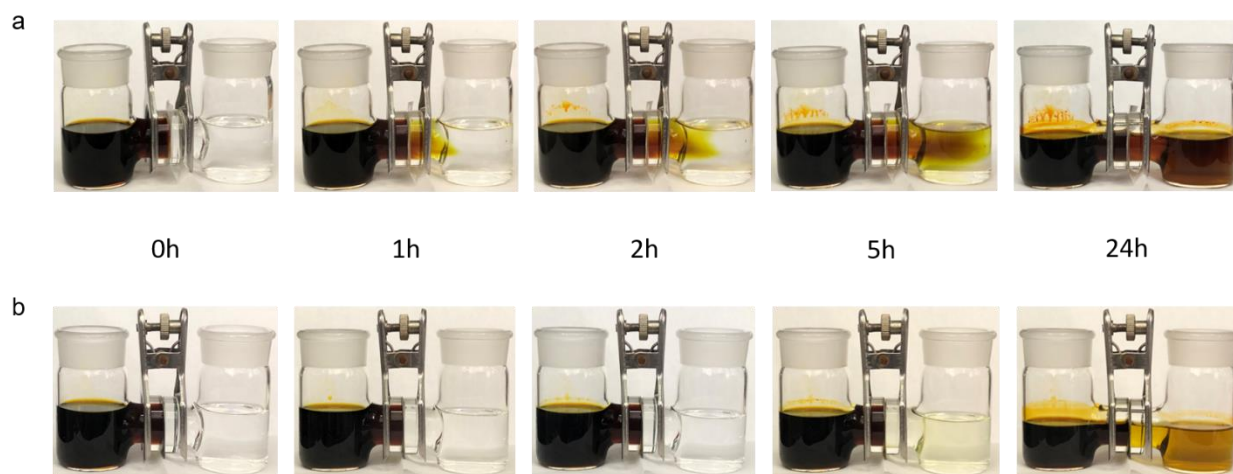
Figure 4.34 Photographs for the diffusion of polysulfide (a) commercial PP separator (b) MIL-100(Cr)-SH/PTFE membrane.

Furthermore, the polysulfide permeability across the membranes was tested using a U-type permeation device shown in **Figure 4.34**. In the beginning, the chocolate-brown lithium polysulfide solution is filled in the left device, while the solvent filled in the right is colorless. After testing for several hours, the polysulfide diffused gradually under the concentration gradient across the membrane. As for the commercial PP separator, the polysulfide almost permeated across the separator immediately and right device turned to chocolate-brown color in 5 hours. However, for the modified MOF/PTFE membrane, the polysulfide permeating rate is much slower, which only showed slightly color change in 5 hours. Here we should put covers on the U-type permeation device to prevent the increasement of the concentration of lithium polysulfide solution, which might increase the permeating rate.

4.3.3 Electrochemical performance

The electrochemical stability windows of MIL-100(Cr)-SH/PTFE membrane was examined by CV test using stainless steel as working electrode. The result (**Figure 4.35**a) indicates reversible Li^+ stripping-plating processes on steel electrode and a good anionic stability to 3 V (*vs.* Li/Li^+) at first 5 cycles for Li-S batteries. The lithium-ion transference number shown is **Figure 4.35**b exhibits a further improved t_{Li^+} up to 0.8, confirming the electrostatic role of SO_3^- groups outside the MOF/PTFE membrane, which benefit the fast single-ion transport of Li^+ within the MOF pores by electrostatic repelling of the anions.
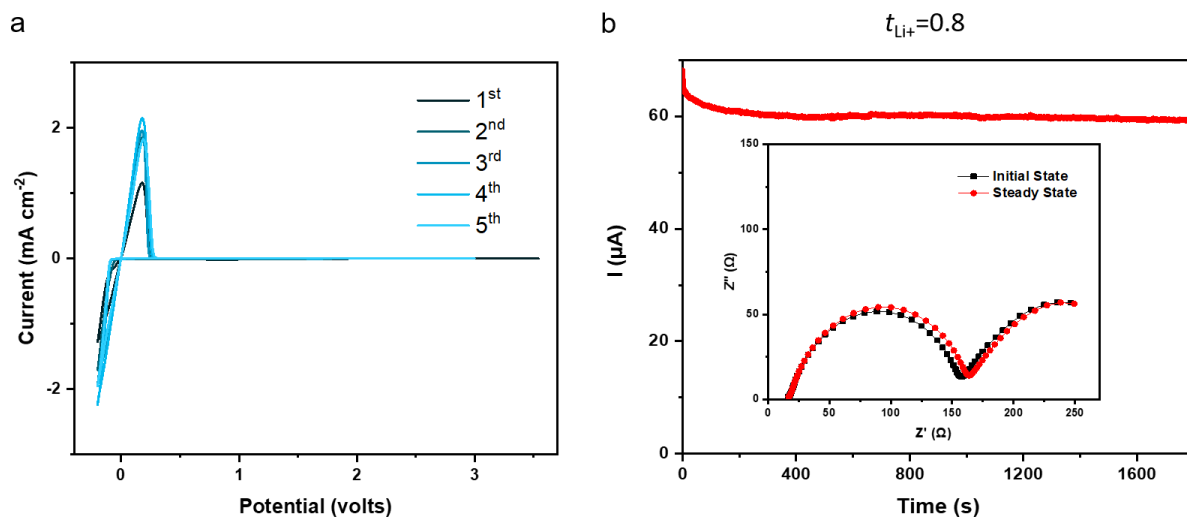
Figure 4.35 (a) CV curves of MIL-100(Cr)-SH/PTFE using electrolyte of 1M LiTFSI, 0.2M LiNO$_3$ form – 0.2 V to 3 V at a scan rate of 0.1 mV/s. (b) Measurement of Li$^+$ transference number of MIL-100(Cr)-SH/PTFE membrane.
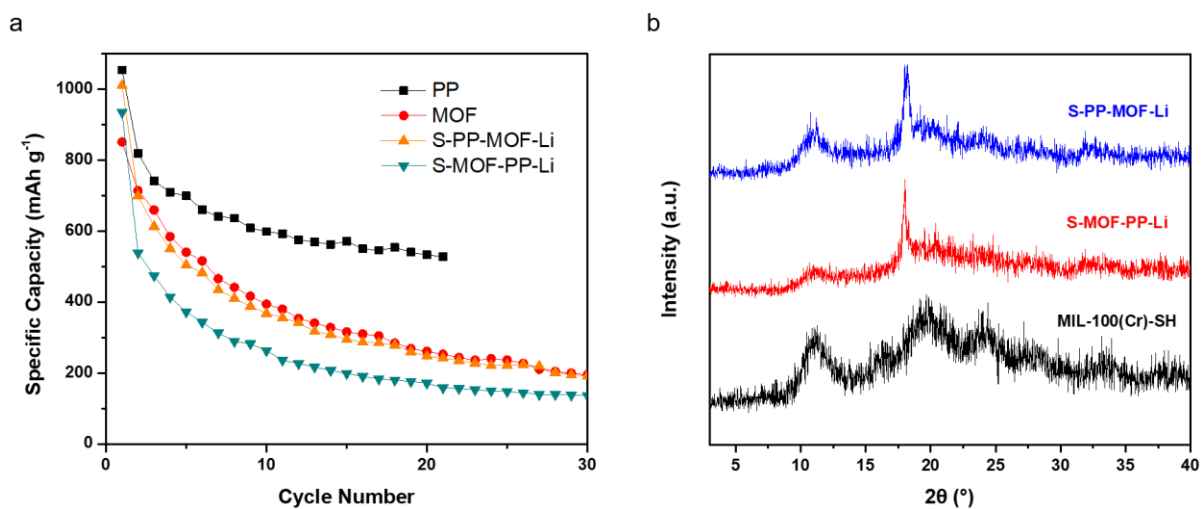
Figure 4.36 (a) Galvanostatic cycling performance of Li-S cells with PP, MIL-100(Cr)-SH/PTFE (denoted as MOF), PP-MOF double membranes with PP contact to sulfur cathode and MOF contact to sulfur cathode at 0.05 C for first cycle and then 0.1 C rates. (b) XRD patterns of MOF in PP-MOF double membranes after 30 cycles.

85

However, the cycling performance of MIL-100(Cr)-SH/PTFE membrane (MOF) is not good as we expected compraed with PP separator in Li-S cells. As shown in **Figure 4.36**a, the capacity of MOF/PTFE membrane fades quickly through the first 10 cycles. To find out the reason, we tried to use PP-MOF double membranes to check if the MOF is unstable when directly contact to sulfur cathode. The result shows no improvement to cycling performance when adding PP separator. In the meantime, the XRD patterns of MOF membranes after 30 cycles are shown in **Figure 4.36**b. Apart from the major peaks for PTFE polymer at around 18°, we can see a clear crystallinity decrease of MOF structure when it is directly contact to sulfur cathode.[172] This indicates an undesired side reaction between MOF and lithium polysulfide, leads to large capacity fading and short cycle life.

The Li-S cell discharge mechanism is well-known to be a complex multistep process, which might help us to understand why MOF-based membrane fails in Li-S cells. As shown in **Figure 4.37**, a possible mechanism for sulfur reduction consisting of three steps were proposed.[173] Long polysulfide chains are produced during the first reduction step (2.4 – 2.2 V *vs.* Li^+ /Li), such as S_8^{2-} and S_6^{2-}. The $S_3^{\bullet-}$ radical can also be found in solution because of a dissociation reaction from S_6^{2-}.[174-175] The $S_3^{\bullet-}$ radical might be stable in solvents commonly used in Li-S batteires.[176] However, when directly contact to MOF framework, it might coordinated to Cr metal centers due to higher reactivity than Cr-S we modified. This could explain why our MOF-based membrane fails in Li-S cells and researchsers usually use carbon nanotubes (CNT)[51] or graphene oxide (GO)[177] as MOF composite separators to prevent MOF from directly contacting to sulfur cathode.
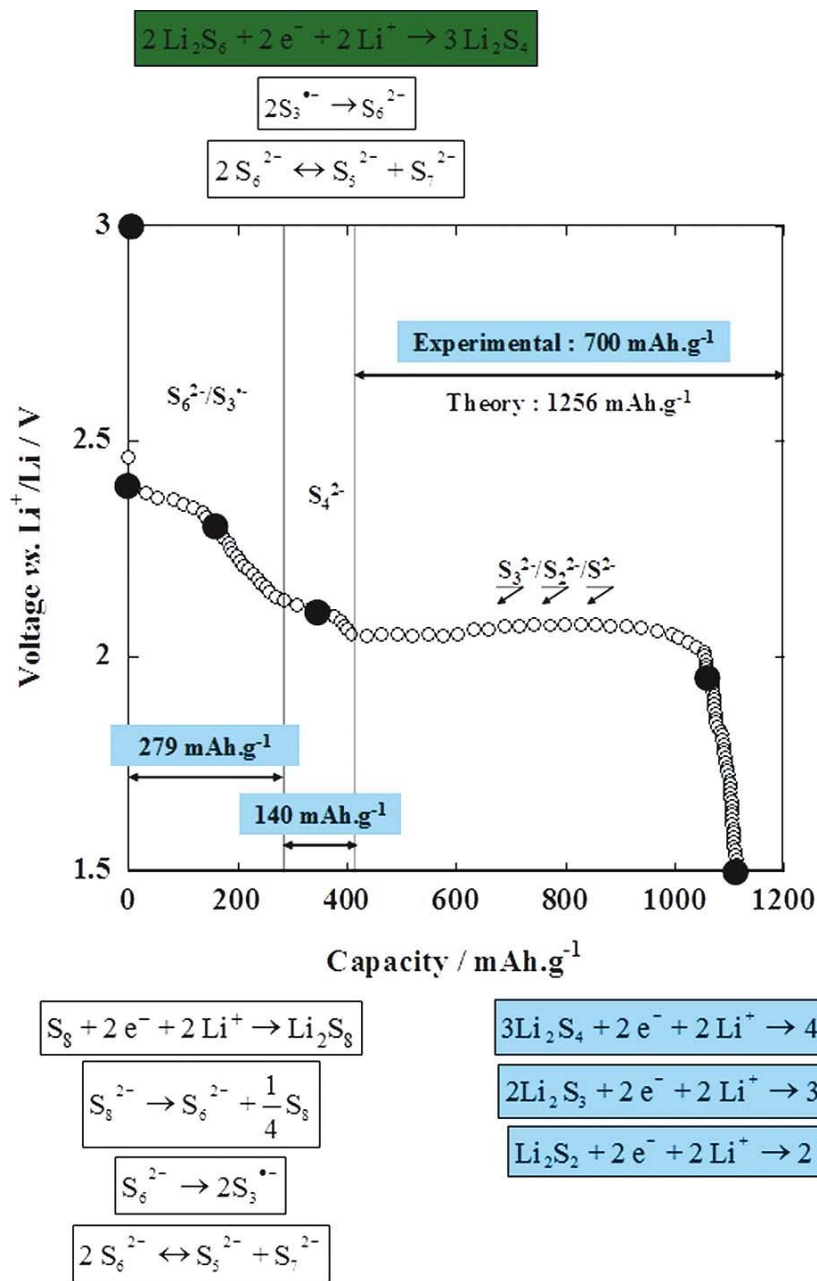
Figure 4.37 Proposed sulful reduction mechanism, involving disproportionation and electrochemical reactions. Major lithium polysulfide compounds are listed on the figure, as well as the specific capacities corresponding to each step.[173]

Although our MOF-based membrane fails in Li-S cells, it can still serve as a high lithium transference number single-ion conductor and it has been proven to be stable with lithium metal.

87

Thus, Li-LTO batteries were performed in **Figure 4.38**. A similar 50% MIL-100(Cr)-SH/PVDF-HFP-GF (denoted as MOF-GF) composite electrolyte was used here to compared with GF. The MOF-GF exhibits an initial capacity of 155 mAh g^{-1} at 0.2 C and a stable cycling performance at 0.5 C. While GF shows a lower initial capacity of 140 mAh g^{-1} 0.2 C and its discharge capacity decrease quickly after 300 cycles.
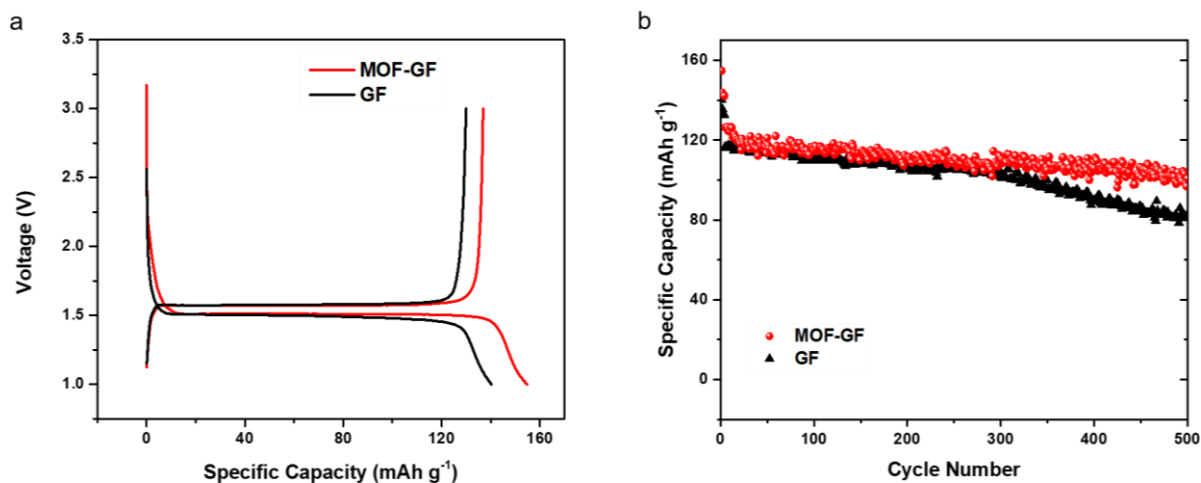
Figure 4.38 (a) Charge and discharge profile of first cycle of MOF-GF and GF in 0.2 C. (b) Cycling performance of MOF-GF and GF at 0.2 C for first 5 cycles then 0.5 C rates.

SUMMARY AND CONCLUSIONS

In summary, we developed a novel family of solid-like electrolytes containing the cations of the 3rd period (Na^+, Mg^{2+} and Al^{3+}) and 1st group (Li^+, Na^+, K^+ and Cs^+) by infiltrating MOF scaffolds with the liquid-electrolyte counterparts. The strategy reported here is enabled by the strong interactions between anions and the OMSs in MOFs. In these composite electrolytes, the anions are immobilized within the MOF channels and the cations are released for fast translocation. These solid-like electrolytes not only exhibit high ionic conductivities ($> 10^{-4}$ S cm^{-1}), but also low activation energies ($0.20 - 0.37$ eV), in which a record conductivity for Mg^{2+} was achieved (1.0 S cm^{-1}). From Na^+, Mg^{2+} to Al^{3+} ions with increasing charge density, the liquid electrolytes show reducing ionic conductivity. For the solid-like electrolytes, Mg-MOF exhibits the highest ionic and the lowest activation energy due to the highest charge-carrier concentration and highly mobile Mg^{2+} solvated in PC. From Li^+, Na^+, K^+ to Cs^+ with reducing Stokes radii and ionic solvation shell thickness, both the liquid electrolytes and solid-like electrolytes show a similar trend of increasing conductivity. This work reveals the ion-conduction principles of the corresponding solvated cations in anion-complexed MOFs, demonstrating the feasibility of using MOFs as hosts to design fast-conducting solid-state electrolytes for alkali or multivalent metal ions.

In addition, we successfully utilized MOF-based solid-like electrolytes in Na-metal batteries. Both MOF/polymer composite electrolytes on GF served as functional separator or directly as gel polymer electrolytes show advantages compared with commercial separators. For example, 50% MOF-GF exhibits much higher rate performance than GF and 75% MOF as gel polymer electrolyte presents highly improved cycle stability and Columbic efficiency compared with PP. Therefore, confining liquid electrolyte and complexing respective anions by MOFs substantially tackle the issues of cell polarization and interfacial stability. This work expands the application of MOF-

89

based solid-like electrolytes from Li to Na metal batteries, offering the possibility for further applications in rechargeable batteries.

Although the MOF-based solid-like electrolytes are not well suited in Li-S cells, the experience and lesson we learned are much more valuable. Here we conclude that during charge/discharge processes, the $S_3^{\bullet-}$ radical might be reactive to the metal center in MOF-based electrolytes. Thus, more strategy needed here to prevent MOF-based electrolytes from directly contact to sulfur cathode or design a more stable MOF structure when decorating functional groups.

In the end, we hope the work in this dissertation could shed some light on the design of fast-conducting solid-like electrolytes for alkali or multivalent metal ions, as well as the applications to the next-generation high energy density solid-state rechargeable batteries.

REFERENCE

(1) Dunn, B.; Kamath, H.; Tarascon, J.-M. Electrical energy storage for the grid: a battery of choices. *Science* **2011,** *334*, 928-935.

(2) Huang, Y.; Zhu, M.; Huang, Y.; Pei, Z.; Li, H.; Wang, Z.; Xue, Q.; Zhi, C. Multifunctional energy storage and conversion devices. *Advanced Materials* **2016**.

(3) McCloskey, B. D., Expanding the ragone plot: Pushing the limits of energy storage. ACS Publications: 2015.

(4) Jiang, D.-e.; Wu, J. Microscopic insights into the electrochemical behavior of nonaqueous electrolytes in electric double-layer capacitors. *The journal of physical chemistry letters* **2013,** *4*, 1260-1267.

(5) Ormerod, R. M. Solid oxide fuel cells. *Chemical Society Reviews* **2003,** *32*, 17-28.

(6) Tsutsumi, A. Fuel cell/battery system. *Tenth issue of Tansei* **2013**.

(7) Tsiropoulos, I.; Tarvydas, D.; Lebedeva, N. Li-ion batteries for mobility and stationary storage applications. *JRC Science for policy report* **2018**.

(8) Andwari, A. M.; Pesiridis, A.; Rajoo, S.; Martinez-Botas, R.; Esfahanian, V. A review of Battery Electric Vehicle technology and readiness levels. *Renewable and Sustainable Energy Reviews* **2017,** *78*, 414-430.

(9) Sekai, K.; Azuma, H.; Omaru, A.; Fujita, S.; Imoto, H.; Endo, T.; Yamaura, K.; Nishi, Y.; Mashiko, S.; Yokogawa, M. Lithium-ion rechargeable cells with LiCoO2 and carbon electrodes. *Journal of power sources* **1993,** *43*, 241-244.

(10) Kamat, P. V.; Goodenough, J. B.; Whittingham, M. S.; Siu, C.; Ding, J.; Wang, X.; Lin, Y.-C.; Zhou, H.; Omenya, F.; Chu, I.-H. Lithium-Ion Batteries and Beyond: Celebrating the 2019 Nobel Prize in Chemistry-A Virtual Issue. *Acc. Chem. Res* **2019,** *46*, 1053-1061.

(11) Goodenough, J. B. How we made the Li-ion rechargeable battery. *Nature Electronics* **2018, 1**, 204-204.

(12) Goodenough, J. B. Rechargeable batteries: challenges old and new. *Journal of Solid State Electrochemistry* **2012, 16**, 2019-2029.

(13) Goodenough, J. B.; Kim, Y. Challenges for rechargeable Li batteries. *Chemistry of materials* **2010, 22**, 587-603.

(14) Cheng, X.-B.; Zhang, R.; Zhao, C.-Z.; Zhang, Q. Toward safe lithium metal anode in rechargeable batteries: a review. *Chemical reviews* **2017, 117**, 10403-10473.

(15) Smith, L.; Dunn, B. Opening the window for aqueous electrolytes. *Science* **2015, 350**, 918-918.

(16) Chan, C. K.; Peng, H.; Liu, G.; McIlwrath, K.; Zhang, X. F.; Huggins, R. A.; Cui, Y. High-performance lithium battery anodes using silicon nanowires. *Nature nanotechnology* **2008, 3**, 31-35.

(17) Kim, S.; Cho, W.; Zhang, X.; Oshima, Y.; Choi, J. W. A stable lithium-rich surface structure for lithium-rich layered cathode materials. *Nature communications* **2016, 7**, 13598.

(18) Nazar, L. F.; Cuisinier, M.; Pang, Q. Lithium-sulfur batteries. *MRS Bulletin* **2014, 39**, 436-442.

(19) Bruce, P. G.; Freunberger, S. A.; Hardwick, L. J.; Tarascon, J.-M. Li-O2 and Li-S batteries with high energy storage. *Nat Mater* **2012, 11**, 19-29.

(20) Aurbach, D.; McCloskey, B. D.; Nazar, L. F.; Bruce, P. G. Advances in understanding mechanisms underpinning lithium–air batteries. *Nature Energy* **2016, 1**, 16128.

(21) Wang, H.; Matsui, M.; Kuwata, H.; Sonoki, H.; Matsuda, Y.; Shang, X.; Takeda, Y.; Yamamoto, O.; Imanishi, N. A reversible dendrite-free high-areal-capacity lithium metal electrode. *Nature Communications* **2017,** *8*.

(22) Muldoon, J.; Bucur, C. B.; Oliver, A. G.; Sugimoto, T.; Matsui, M.; Kim, H. S.; Allred, G. D.; Zajicek, J.; Kotani, Y. Electrolyte roadblocks to a magnesium rechargeable battery. *Energy & Environmental Science* **2012,** *5*, 5941-5950.

(23) Zhang, T.; Tao, Z.; Chen, J. Magnesium–air batteries: from principle to application. *Materials Horizons* **2014,** *1*, 196-206.

(24) Grishina, E.; Gelman, D.; Belopukhov, S.; Starosvetsky, D.; Groysman, A.; Ein-Eli, Y. Improvement of Aluminum-Air Battery Performances by the Application of Flax Straw Extract. *ChemSusChem* **2016,** *9*, 2103-2111.

(25) Gao, Z.; Sun, H.; Fu, L.; Ye, F.; Zhang, Y.; Luo, W.; Huang, Y. Promises, challenges, and recent progress of inorganic solid-state electrolytes for all-solid-state lithium batteries. *Advanced materials* **2018,** *30*, 1705702.

(26) Janek, J.; Zeier, W. G. A solid future for battery development. *Nature Energy* **2016,** *1*, 1-4.

(27) Kim, T.; Song, W.; Son, D.-Y.; Ono, L. K.; Qi, Y. Lithium-ion batteries: outlook on present, future, and hybridized technologies. *Journal of materials chemistry A* **2019,** *7*, 2942-2964.

(28) Liang, Z.; Lin, D.; Zhao, J.; Lu, Z.; Liu, Y.; Liu, C.; Lu, Y.; Wang, H.; Yan, K.; Tao, X. Composite lithium metal anode by melt infusion of lithium into a 3D conducting scaffold with lithiophilic coating. *Proceedings of the National Academy of Sciences* **2016,** *113*, 2862-2867.

(29) Tarascon, J.-M.; Armand, M. Issues and challenges facing rechargeable lithium batteries. *Nature* **2001,** *414*, 359-367.

(30) Xu, W.; Wang, J.; Ding, F.; Chen, X.; Nasybulin, E.; Zhang, Y.; Zhang, J.-G. Lithium metal anodes for rechargeable batteries. *Energy & Environmental Science* **2014,** *7*, 513-537, DOI: 10.1039/C3EE40795K.

(31) Yan, K.; Lee, H.-W.; Gao, T.; Zheng, G.; Yao, H.; Wang, H.; Lu, Z.; Zhou, Y.; Liang, Z.; Liu, Z.; Chu, S.; Cui, Y. Ultrathin Two-Dimensional Atomic Crystals as Stable Interfacial Layer for Improvement of Lithium Metal Anode. *Nano Letters* **2014,** *14*, 6016-6022, DOI: 10.1021/nl503125u.

(32) Dias, F. B.; Plomp, L.; Veldhuis, J. B. J. Trends in polymer electrolytes for secondary lithium batteries. *Journal of Power Sources* **2000,** *88*, 169-191, DOI: https://doi.org/10.1016/S0378-7753(99)00529-7.

(33) Thangadurai, V.; Narayanan, S.; Pinzaru, D. Garnet-type solid-state fast Li ion conductors for Li batteries: critical review. *Chemical Society Reviews* **2014,** *43*, 4714-4727, DOI: 10.1039/C4CS00020J.

(34) Lu, Y.; Tu, Z.; Archer, L. A. Stable lithium electrodeposition in liquid and nanoporous solid electrolytes. *Nat Mater* **2014,** *13*, 961-969, DOI: 10.1038/nmat4041

http://www.nature.com/nmat/journal/v13/n10/abs/nmat4041.html#supplementary-information.

(35) Ding, F.; Xu, W.; Graff, G. L.; Zhang, J.; Sushko, M. L.; Chen, X.; Shao, Y.; Engelhard, M. H.; Nie, Z.; Xiao, J.; Liu, X.; Sushko, P. V.; Liu, J.; Zhang, J.-G. Dendrite-Free Lithium Deposition via Self-Healing Electrostatic Shield Mechanism. *Journal of the American Chemical Society* **2013,** *135*, 4450-4456, DOI: 10.1021/ja312241y.

(36) Han, F.; Westover, A. S.; Yue, J.; Fan, X.; Wang, F.; Chi, M.; Leonard, D. N.; Dudney, N. J.; Wang, H.; Wang, C. High electronic conductivity as the origin of lithium dendrite formation within solid electrolytes. *Nature Energy* **2019,** *4*, 187-196.

(37) Massé, R. C.; Uchaker, E.; Cao, G. Beyond Li-ion: electrode materials for sodium-and magnesium-ion batteries. *Science China Materials* **2015,** *58*, 715-766.

(38) Kubota, K.; Dahbi, M.; Hosaka, T.; Kumakura, S.; Komaba, S. Towards K-Ion and Na-Ion Batteries as "Beyond Li-Ion". *The Chemical Record* **2018,** *18*, 459-479.

(39) Zhang, Y.; Liu, S.; Ji, Y.; Ma, J.; Yu, H. Emerging Nonaqueous Aluminum-Ion Batteries: Challenges, Status, and Perspectives. *Advanced Materials* **2018,** *30*, 1706310.

(40) Elia, G. A.; Marquardt, K.; Hoeppner, K.; Fantini, S.; Lin, R.; Knipping, E.; Peters, W.; Drillet, J. F.; Passerini, S.; Hahn, R. An overview and future perspectives of aluminum batteries. *Advanced Materials* **2016,** *28*, 7564-7579.

(41) Hwang, J.-Y.; Myung, S.-T.; Sun, Y.-K. Sodium-ion batteries: present and future. *Chemical Society Reviews* **2017,** *46*, 3529-3614.

(42) Li, F.; Wei, Z.; Manthiram, A.; Feng, Y.; Ma, J.; Mai, L. Sodium-based batteries: from critical materials to battery systems. *Journal of materials chemistry A* **2019,** *7*, 9406-9431.

(43) Hwang, J. Y.; Myung, S. T.; Sun, Y. K. Recent progress in rechargeable potassium batteries. *Advanced Functional Materials* **2018,** *28*, 1802938.

(44) Zhang, W.; Liu, Y.; Guo, Z. Approaching high-performance potassium-ion batteries via advanced design strategies and engineering. *Science advances* **2019,** *5*, eaav7412.

(45) Muldoon, J.; Bucur, C. B.; Gregory, T. Quest for nonaqueous multivalent secondary batteries: magnesium and beyond. *Chemical reviews* **2014,** *114*, 11683-11720.

(46) Zheng, J.; Tian, J.; Wu, D.; Gu, M.; Xu, W.; Wang, C.; Gao, F.; Engelhard, M. H.; Zhang, J.-G.; Liu, J. Lewis acid–base interactions between polysulfides and metal organic framework in lithium sulfur batteries. *Nano letters* **2014,** *14*, 2345-2352.

(47) Peng, H. J.; Huang, J. Q.; Cheng, X. B.; Zhang, Q. Review on high-loading and high-energy lithium–sulfur batteries. *Advanced Energy Materials* **2017,** *7*, 1700260.

(48) Pang, Q.; Liang, X.; Kwok, C. Y.; Nazar, L. F. Advances in lithium-sulfur batteries based on multifunctional cathodes and electrolytes. *Nature Energy* **2016,** *1*, 16132.

(49) Park, H.; Siegel, D. J. Tuning the Adsorption of Polysulfides in Lithium-Sulfur Batteries with Metal–Organic Frameworks. *Chem. Mater* **2017,** *29*, 4932-4939.

(50) Zheng, Y.; Zheng, S.; Xue, H.; Pang, H. Metal–organic frameworks for lithium-sulfur batteries. *Journal of Materials Chemistry A* **2019,** *7*, 3469-3491.

(51) Li, M.; Wan, Y.; Huang, J.-K.; Assen, A. H.; Hsiung, C.-E.; Jiang, H.; Han, Y.; Eddaoudi, M.; Lai, Z.; Ming, J. Metal-organic framework-based separators for enhancing Li-S battery stability: mechanism of mitigating polysulfide diffusion. *ACS Energy Letters* **2017,** *2*, 2362-2367.

(52) Kamaya, N.; Homma, K.; Yamakawa, Y.; Hirayama, M.; Kanno, R.; Yonemura, M.; Kamiyama, T.; Kato, Y.; Hama, S.; Kawamoto, K. A lithium superionic conductor. *Nature materials* **2011,** *10*, 682-686.

(53) Khurana, R.; Schaefer, J. L.; Archer, L. A.; Coates, G. W. Suppression of Lithium Dendrite Growth Using Cross-Linked Polyethylene/Poly(ethylene oxide) Electrolytes: A New Approach for Practical Lithium-Metal Polymer Batteries. *Journal of the American Chemical Society* **2014,** *136*, 7395-7402, DOI: 10.1021/ja502133j.

(54) Hovington, P.; Lagacé, M.; Guerfi, A.; Bouchard, P.; Mauger, A.; Julien, C. M.; Armand, M.; Zaghib, K. New Lithium Metal Polymer Solid State Battery for an Ultrahigh Energy: Nano C-LiFePO$_4$ versus Nano Li$_{1.2}$V$_3$O$_8$. *Nano Letters* **2015,** *15*, 2671-2678, DOI: 10.1021/acs.nanolett.5b00326.

(55) Kobayashi, T.; Imade, Y.; Shishihara, D.; Homma, K.; Nagao, M.; Watanabe, R.; Yokoi, T.; Yamada, A.; Kanno, R.; Tatsumi, T. All solid-state battery with sulfur electrode and thio-LISICON electrolyte. *Journal of Power Sources* **2008,** *182*, 621-625, DOI: https://doi.org/10.1016/j.jpowsour.2008.03.030.

(56) Faraday, M. Experimental researches in electricity. third series. *Philosophical Transactions of the Royal Society of London* **1833,** *123*, 23-54.

(57) Knödler, R. Thermal properties of sodium-sulphur cells. *Journal of applied electrochemistry* **1984,** *14*, 39-46.

(58) Fenton, D.; Parker, J.; Wright, P. Complexes of alkali metal ions with poly (ethylene oxide). *polymer* **1973,** *14*, 589.

(59) Dudney, N.; Bates, J.; Zuhr, R.; Luck, C.; Robertson, J. Sputtering of lithium compounds for preparation of electrolyte thin films. *solid state ionics* **1992,** *53*, 655-661.

(60) Bachman, J. C.; Muy, S.; Grimaud, A.; Chang, H.-H.; Pour, N.; Lux, S. F.; Paschos, O.; Maglia, F.; Lupart, S.; Lamp, P. Inorganic solid-state electrolytes for lithium batteries: mechanisms and properties governing ion conduction. *Chemical reviews* **2015,** *116*, 140-162.

(61) Manthiram, A.; Yu, X.; Wang, S. Lithium battery chemistries enabled by solid-state electrolytes. *Nature Reviews Materials* **2017,** *2*, 16103.

(62) Zhang, H.; Yang, T.; Wu, X.; Zhou, Y.; Yang, C.; Zhu, T.; Dong, R. Using Li^+ as the electrochemical messenger to fabricate an aqueous rechargeable Zn-Cu battery. *Chemical Communications* **2015,** *51*, 7294-7297.

(63) Quartarone, E.; Mustarelli, P. Electrolytes for solid-state lithium rechargeable batteries: recent advances and perspectives. *Chemical Society Reviews* **2011,** *40*, 2525-2540.

(64) Hu, Y.-S. Batteries: getting solid. *Nature Energy* **2016,** *1*, 16042.

(65) Fan, L.; Wei, S.; Li, S.; Li, Q.; Lu, Y. Recent progress of the solid-state electrolytes for high-energy metal-based batteries. *Advanced Energy Materials* **2018,** *8*, 1702657.

(66) Zhang, Z.; Hu, L.; Wu, H.; Weng, W.; Koh, M.; Redfern, P. C.; Curtiss, L. A.; Amine, K. Fluorinated electrolytes for 5 V lithium-ion battery chemistry. *Energy & Environmental Science* **2013,** *6*, 1806-1810, DOI: 10.1039/C3EE24414H.

(67) Xu, K. Nonaqueous liquid electrolytes for lithium-based rechargeable batteries. *Chemical reviews* **2004,** *104*, 4303-4418.

(68) Zhang, J.; Bai, Y.; Sun, X.-G.; Li, Y.; Guo, B.; Chen, J.; Veith, G. M.; Hensley, D. K.; Paranthaman, M. P.; Goodenough, J. B. Superior conductive solid-like electrolytes: nanoconfining liquids within the hollow structures. *Nano letters* **2015,** *15*, 3398-3402.

(69) Aubrey, M.; Ameloot, R.; Wiers, B. M.; Long, J. R. Metal–organic frameworks as solid magnesium electrolytes. *Energy & Environmental Science* **2014,** *7*, 667-671.

(70) Wiers, B. M.; Foo, M.-L.; Balsara, N. P.; Long, J. R. A solid lithium electrolyte via addition of lithium isopropoxide to a metal-organic framework with open metal sites. *Journal of the American Chemical Society* **2011,** *133*, 14522-14525.

(71) Zhou, D.; Liu, R.; He, Y. B.; Li, F.; Liu, M.; Li, B.; Yang, Q. H.; Cai, Q.; Kang, F. SiO2 Hollow Nanosphere-Based Composite Solid Electrolyte for Lithium Metal Batteries to Suppress Lithium Dendrite Growth and Enhance Cycle Life. *Advanced Energy Materials* **2016,** *6*, 1502214.

(72) Tu, Z.; Kambe, Y.; Lu, Y.; Archer, L. A. Nanoporous polymer-ceramic composite electrolytes for lithium metal batteries. *Advanced Energy Materials* **2014,** *4*, 1300654.

(73) Tu, Z.; Zachman, M. J.; Choudhury, S.; Wei, S.; Ma, L.; Yang, Y.; Kourkoutis, L. F.; Archer, L. A. Nanoporous hybrid electrolytes for high-energy batteries based on reactive metal anodes. *Advanced Energy Materials* **2017,** *7*, 1602367.

(74) Ramaswamy, P.; Wong, N. E.; Shimizu, G. K. H. MOFs as proton conductors - challenges and opportunities. *Chemical Society Reviews* **2014,** *43*, 5913-5932, DOI: 10.1039/C4CS00093E.

(75) Goodenough, J. B. Oxide-Ion Electrolytes. *Annual Review of Materials Research* **2003,** *33*, 91-128, DOI: 10.1146/annurev.matsci.33.022802.091651.

(76) Mukherjee, L.; Coetzee, J. Non-Aqueous Solvent Chemistry–Some Recent Studies. **1974**.

(77) Coetzee, J. Ligand substitution kinetics of labile metal complexes in nonaqueous solvents. In *Solute-Solvent Interactions*; Marcel Dekker: 1976; pp 331-418.

(78) Matsuura, N.; Umemoto, K.; Takeda, Y.; Sasaki, A. Formation constants of dibenzo-18-crown-6 complexes with alkali metal ions in DMSO, DMF, and PC at 25 C. *Bulletin of the Chemical Society of Japan* **1976,** *49*, 1246-1249.

(79) Srivastava, A. K.; Shankar, S. L. Ionic conductivity in binary solvent mixtures. 3. Dimethyl sulfoxide+ propylene carbonate at 25° C. *Journal of Chemical & Engineering Data* **1998,** *43*, 25-28.

(80) Matsuda, Y.; Nakashima, H.; Morita, M.; Takasu, Y. Behavior of some ions in mixed organic electrolytes of high energy density batteries. *Journal of the electrochemical society* **1981,** *128*, 2552.

(81) Kaminsky, M. Ion-solvent interaction and the viscosity of strong-electrolyte solutions. *Discussions of the Faraday Society* **1957,** *24*, 171-179.

(82) Puhovski, Y. P.; Rode, B. M. Solvated ion dynamics in the water-formamide mixtures using molecular dynamics simulations. *The Journal of chemical physics* **1997,** *107*, 6908-6916.

(83) Bahga, S. S.; Bercovici, M.; Santiago, J. G. Ionic strength effects on electrophoretic focusing and separations. *Electrophoresis* **2010,** *31*, 910-919.

(84) Porras, S. P.; Riekkola, M.-L.; Kenndler, E. Electrophoretic mobilities of cationic analytes in non-aqueous methanol, acetonitrile and their mixtures: Influence of ionic strength and ion-pair formation. *Journal of Chromatography A* **2001,** *924*, 31-42.

(85) Linford, R.; Hackwood, S. Physical techniques for the study of solid electrolytes. *Chemical Reviews* **1981,** *81*, 327-364.

(86) Evans, J.; Vincent, C. A.; Bruce, P. G. Electrochemical measurement of transference numbers in polymer electrolytes. *Polymer* **1987,** *28*, 2324-2328.

(87) Lu, Y.; Das, S. K.; Moganty, S. S.; Archer, L. A. Ionic Liquid-Nanoparticle Hybrid Electrolytes and their Application in Secondary Lithium-Metal Batteries. *Advanced Materials* **2012,** *24*, 4430-4435.

(88) Tu, Z.; Kambe, Y.; Lu, Y.; Archer, L. A. Nanoporous polymer-ceramic composite electrolytes for lithium metal batteries. *Advanced Energy Materials* **2014,** *4*.

(89) Park, K.; Cho, J. H.; Shanmuganathan, K.; Song, J.; Peng, J.; Gobet, M.; Greenbaum, S.; Ellison, C. J.; Goodenough, J. B. New battery strategies with a polymer/Al_2O_3 separator. *Journal of Power Sources* **2014,** *263*, 52-58.

(90) Ansari, Y.; Guo, B.; Cho, J. H.; Park, K.; Song, J.; Ellison, C. J.; Goodenough, J. B. Low-Cost, Dendrite-Blocking Polymer-Sb2O3 Separators for Lithium and Sodium Batteries. *Journal of The Electrochemical Society* **2014,** *161*, A1655-A1661.

(91) Ameloot, R.; Aubrey, M.; Wiers, B. M.; Gómora-Figueroa, A. P.; Patel, S. N.; Balsara, N. P.; Long, J. R. Ionic Conductivity in the Metal–Organic Framework UiO-66 by Dehydration and Insertion of Lithium tert-Butoxide. *Chemistry-A European Journal* **2013,** *19*, 5533-5536.

(92) Zhao, R.; Liang, Z.; Zou, R.; Xu, Q. Metal-Organic Frameworks for Batteries. *Joule* **2018,** *2*, 2235-2259, DOI: https://doi.org/10.1016/j.joule.2018.09.019.

(93) Song, J. Y.; Ahmed, I.; Seo, P. W.; Jhung, S. H. UiO-66-Type Metal–Organic Framework with Free Carboxylic Acid: Versatile Adsorbents via H-bond for Both Aqueous and Nonaqueous Phases. *ACS Applied Materials & Interfaces* **2016,** *8*, 27394-27402, DOI: 10.1021/acsami.6b10098.

(94) Zhang, J.-P.; Zhang, Y.-B.; Lin, J.-B.; Chen, X.-M. Metal azolate frameworks: from crystal engineering to functional materials. *Chemical reviews* **2011,** *112*, 1001-1033.

(95) Mason, J. A.; Veenstra, M.; Long, J. R. Evaluating metal–organic frameworks for natural gas storage. *Chemical Science* **2014,** *5*, 32-51.

(96) Yamada, T.; Sadakiyo, M.; Kitagawa, H. High proton conductivity of one-dimensional ferrous oxalate dihydrate. *Journal of the American Chemical Society* **2009,** *131*, 3144-3145.

(97) Yoon, M.; Suh, K.; Natarajan, S.; Kim, K. Proton conduction in metal–organic frameworks and related modularly built porous solids. *Angewandte Chemie International Edition* **2013,** *52*, 2688-2700.

(98) Ortiz, A. l. U.; Boutin, A.; Fuchs, A. H.; Coudert, F. o.-X. Investigating the pressure-induced amorphization of zeolitic imidazolate framework ZIF-8: mechanical instability due to shear mode softening. *The journal of physical chemistry letters* **2013,** *4*, 1861-1865.

(99) Park, S. S.; Tulchinsky, Y.; Dinca, M. Single-Ion Li$^+$, Na$^+$, and Mg^{2+} Solid Electrolytes Supported by a Mesoporous Anionic Cu-azolate MOF. *Journal of the American Chemical Society* **2017**.

(100) Tranchemontagne, D. J.; Mendoza-Cortes, J. L.; O'Keeffe, M.; Yaghi, O. M. Secondary building units, nets and bonding in the chemistry of metal-organic frameworks. *Chemical Society Reviews* **2009,** *38*, 1257-1283, DOI: 10.1039/B817735J.

(101) Kaneko, F.; Wada, S.; Nakayama, M.; Wakihara, M.; Koki, J.; Kuroki, S. Capacity Fading Mechanism in All Solid-State Lithium Polymer Secondary Batteries Using PEG-Borate/Aluminate Ester as Plasticizer for Polymer Electrolytes. *Advanced Functional Materials* **2009,** *19*, 918-925.

(102) Cepeda, J.; Pérez-Yáñez, S.; Beobide, G.; Castillo, O.; Goikolea, E.; Aguesse, F.; Garrido, L.; Luque, A.; Wright, P. A. Scandium/Alkaline Metal-Organic Frameworks: Adsorptive Properties and Ionic Conductivity. *Chemistry of Materials* **2016,** *28*, 2519-2528, DOI: 10.1021/acs.chemmater.5b03458.

(103) Miner, E. M.; Park, S. S.; Dinca, M. High Li^+ and Mg^{2+} conductivity in a Cu-azolate metal-organic framework. *Journal of the American Chemical Society* **2019**.

(104) Wu, F.; Yushin, G. Conversion cathodes for rechargeable lithium and lithium-ion batteries. *Energy & Environmental Science* **2017,** *10*, 435-459.

(105) Hwang, J.-Y.; Myung, S.-T.; Sun, Y.-K. Sodium-ion batteries: present and future. *Chemical Society Reviews* **2017**.

(106) Fergus, J. W. Ceramic and polymeric solid electrolytes for lithium-ion batteries. *Journal of Power Sources* **2010,** *195*, 4554-4569.

(107) Lian, P.-J.; Zhao, B.-S.; Zhang, L.-Q.; Xu, N.; Wu, M.-T.; Gao, X.-P. Inorganic sulfide solid electrolytes for all-solid-state lithium secondary batteries. *Journal of Materials Chemistry A* **2019,** *7*, 20540-20557.

(108) Tikekar, M. D.; Choudhury, S.; Tu, Z.; Archer, L. A. Design principles for electrolytes and interfaces for stable lithium-metal batteries. *Nature Energy* **2016,** *1*, 1-7.

(109) Chen, R.; Qu, W.; Guo, X.; Li, L.; Wu, F. The pursuit of solid-state electrolytes for lithium batteries: from comprehensive insight to emerging horizons. *Materials Horizons* **2016,** *3*, 487-516.

(110) Yao, P.; Yu, H.; Ding, Z.; Liu, Y.; Lu, J.; Lavorgna, M.; Wu, J.; Liu, X. Review on polymer-based composite electrolytes for Lithium batteries. *Frontiers in chemistry* **2019,** *7*, 522.

(111) Zhao, Y.; Wang, Y. Tailored Solid Polymer Electrolytes by Montmorillonite with High Ionic Conductivity for Lithium-Ion Batteries. *Nanoscale Research Letters* **2019,** *14*, 366.

(112) Ortner, H.; Xu, H.; Dahmen, J.; Englert, K.; Opfermann, H.; Görtz, W. Surface characterization of fluorinated polymers (PTFE, PVDF, PFA) for use in ultratrace analysis. *Fresenius' journal of analytical chemistry* **1996,** *355*, 657-664.

(113) Kerman, K.; Luntz, A.; Viswanathan, V.; Chiang, Y.-M.; Chen, Z. practical challenges hindering the development of solid state Li ion batteries. *Journal of The Electrochemical Society* **2017,** *164*, A1731.

(114) Kaboli, S.; Demers, H.; Paolella, A.; Darwiche, A.; Dontigny, M.; Clement, D.; Guerfi, A.; Trudeau, M. L.; Goodenough, J. B.; Zaghib, K. Behavior of Solid Electrolyte in Li-Polymer Battery with NMC Cathode via in-situ Scanning Electron Microscopy. *Nano Letters* **2020**.

(115) Lu, Q.; Fang, J.; Yang, J.; Miao, R.; Wang, J.; Nuli, Y. Novel cross-linked copolymer gel electrolyte supported by hydrophilic polytetrafluoroethylene for rechargeable lithium batteries. *Journal of membrane science* **2014,** *449*, 176-183.

(116) Stephan, A. M.; Nahm, K. S.; Kulandainathan, M. A.; Ravi, G.; Wilson, J. Poly (vinylidene fluoride-hexafluoropropylene)(PVdF-HFP) based composite electrolytes for lithium batteries. *European Polymer Journal* **2006,** *42*, 1728-1734.

(117) Liu, W.; Zhang, X.; Wu, F.; Xiang, Y. In *A study on PVDF-HFP gel polymer electrolyte for lithium-ion batteries*, IOP Conference Series: Materials Science and Engineering, IOP Publishing: 2017; p 012036.

(118) Croce, F.; Appetecchi, G.; Persi, L.; Scrosati, B. Nanocomposite polymer electrolytes for lithium batteries. *Nature* **1998,** *394*, 456-458.

(119) Lin, D.; Liu, W.; Liu, Y.; Lee, H. R.; Hsu, P.-C.; Liu, K.; Cui, Y. High ionic conductivity of composite solid polymer electrolyte via in situ synthesis of monodispersed SiO2 nanospheres in poly (ethylene oxide). *Nano letters* **2016,** *16*, 459-465.

(120) Xu, Z.; Yang, T.; Chu, X.; Su, H.; Wang, Z.; Chen, N.; Gu, B.; Zhang, H.; Deng, W.; Zhang, H. Strong Lewis Acid-base and Weak Hydrogen Bond Synergistically Enhancing Ionic Conductivity of Poly (ethylene oxide)@ SiO2 Electrolytes for High Rate-capability Li-metal Battery. *ACS Applied Materials & Interfaces* **2020**.

(121) Chiang, C.-Y.; Reddy, M. J.; Chu, P. P. Nano-tube TiO_2 composite PVDF/$LiPF_6$ solid membranes. *Solid State Ionics* **2004,** *175*, 631-635.

(122) Malmonge, L. F.; Langiano, S. d. C.; Cordeiro, J. M. M.; Mattoso, L. H. C.; Malmonge, J. A. Thermal and mechanical properties of PVDF/PANI blends. *Materials Research* **2010,** *13*, 465-470.

(123) Zhang, X.; Liu, T.; Zhang, S.; Huang, X.; Xu, B.; Lin, Y.; Xu, B.; Li, L.; Nan, C.-W.; Shen, Y. Synergistic coupling between $Li_{6.75}La_3Zr_{1.75}Ta_{0.25}O_{12}$ and poly (vinylidene fluoride) induces high ionic conductivity, mechanical strength, and thermal stability of solid composite electrolytes. *Journal of the American Chemical Society* **2017,** *139*, 13779-13785.

(124) Wang, Z.; Tan, R.; Wang, H.; Yang, L.; Hu, J.; Chen, H.; Pan, F. A Metal-Organic-Framework-Based Electrolyte with Nanowetted Interfaces for High-Energy-Density Solid-State Lithium Battery. *Advanced Materials* **2018,** *30*, 1704436.

(125) Wang, Z.; Wang, Z.; Yang, L.; Wang, H.; Song, Y.; Han, L.; Yang, K.; Hu, J.; Chen, H.; Pan, F. Boosting interfacial Li^+ transport with a MOF-based ionic conductor for solid-state batteries. *Nano Energy* **2018,** *49*, 580-587.

(126) Xue, Z.; He, D.; Xie, X. Poly (ethylene oxide)-based electrolytes for lithium-ion batteries. *Journal of Materials Chemistry A* **2015,** *3*, 19218-19253.

(127) D'epifanio, A.; Fiory, F. S.; Licoccia, S.; Traversa, E.; Scrosati, B.; Croce, F. Metallic-lithium, LiFePO 4-based polymer battery using PEO-ZrO_2 nanocomposite polymer electrolyte. *Journal of applied electrochemistry* **2004,** *34*, 403-408.

(128) Wang, Z.; Wang, S.; Wang, A.; Liu, X.; Chen, J.; Zeng, Q.; Zhang, L.; Liu, W.; Zhang, L. Covalently linked metal–organic framework (MOF)-polymer all-solid-state electrolyte membranes for room temperature high performance lithium batteries. *Journal of Materials Chemistry A* **2018,** *6*, 17227-17234.

(129) García Márquez, A.; Demessence, A.; Platero-Prats, A. E.; Heurtaux, D.; Horcajada, P.; Serre, C.; Chang, J. S.; Férey, G.; de la Peña-O'Shea, V.; Boissière, C. Green Microwave Synthesis of MIL-100 (Al, Cr, Fe) Nanoparticles for Thin-Film Elaboration. *European Journal of Inorganic Chemistry* **2012,** *2012*, 5165-5174.

(130) Klee, R.; Aragón, M. J.; Alcántara, R.; Tirado, J. L.; Lavela, P. High-Performance Na_3V_2 $(PO_4)_3$/C Cathode for Sodium-Ion Batteries Prepared by a Ball-Milling-Assisted Method. *European Journal of Inorganic Chemistry* **2016,** *2016*, 3212-3218.

(131) Howarth, A. J.; Liu, Y.; Li, P.; Li, Z.; Wang, T. C.; Hupp, J. T.; Farha, O. K. Chemical, thermal and mechanical stabilities of metal–organic frameworks. *Nature Reviews Materials* **2016,** *1*, 15018.

(132) Pearson, R. G.; Songstad, J. Application of the principle of hard and soft acids and bases to organic chemistry. *Journal of the American Chemical Society* **1967,** *89*, 1827-1836.

(133) Bai, Y.; Dou, Y.; Xie, L.-H.; Rutledge, W.; Li, J.-R.; Zhou, H.-C. Zr-based metal–organic frameworks: design, synthesis, structure, and applications. *Chemical Society Reviews* **2016,** *45*, 2327-2367.

(134) Volkringer, C.; Leclerc, H.; Lavalley, J.-C.; Loiseau, T.; Férey, G. r.; Daturi, M.; Vimont, A. Infrared spectroscopy investigation of the acid sites in the metal-organic framework aluminum trimesate MIL-100 (Al). *The Journal of Physical Chemistry C* **2012,** *116*, 5710-5719.

(135) Shen, L.; Wu, H. B.; Liu, F.; Brosmer, J. L.; Shen, G.; Wang, X.; Zink, J. I.; Xiao, Q.; Cai, M.; Wang, G. Creating Lithium-Ion Electrolytes with Biomimetic Ionic Channels in Metal–Organic Frameworks. *Advanced Materials* **2018,** *30*, 1707476.

(136) Maes, M.; Trekels, M.; Boulhout, M.; Schouteden, S.; Vermoortele, F.; Alaerts, L.; Heurtaux, D.; Seo, Y. K.; Hwang, Y. K.; Chang, J. S. Selective Removal of N-Heterocyclic Aromatic Contaminants from Fuels by Lewis Acidic Metal-Organic Frameworks. *Angewandte Chemie* **2011,** *123*, 4296-4300.

(137) Della Rocca, J.; Liu, D.; Lin, W. Nanoscale metal–organic frameworks for biomedical imaging and drug delivery. *Accounts of chemical research* **2011,** *44*, 957.

(138) Volkringer, C.; Popov, D.; Loiseau, T.; Férey, G.; Burghammer, M.; Riekel, C.; Haouas, M.; Taulelle, F. Synthesis, single-crystal X-ray microdiffraction, and NMR characterizations of the giant pore metal-organic framework aluminum trimesate MIL-100. *Chemistry of Materials* **2009,** *21*, 5695-5697.

(139) Llewellyn, P. L.; Bourrelly, S.; Serre, C.; Vimont, A.; Daturi, M.; Hamon, L.; De Weireld, G.; Chang, J.-S.; Hong, D.-Y.; Kyu Hwang, Y. High uptakes of CO_2 and CH_4 in mesoporous metal organic frameworks mil-100 and mil-101. *Langmuir* **2008,** *24*, 7245-7250.

(140) Haouas, M.; Volkringer, C.; Loiseau, T.; Férey, G.; Taulelle, F. Monitoring the Activation Process of the Giant Pore MIL-100(Al) by Solid State NMR. *The Journal of Physical Chemistry C* **2011,** *115*, 17934-17944, DOI: 10.1021/jp206513v.

(141) Leclerc, H.; Vimont, A.; Lavalley, J.-C.; Daturi, M.; Wiersum, A. D.; Llwellyn, P. L.; Horcajada, P.; Férey, G.; Serre, C. Infrared study of the influence of reducible iron (III) metal sites on the adsorption of CO, CO_2, propane, propene and propyne in the mesoporous metal–organic framework MIL-100. *Physical Chemistry Chemical Physics* **2011,** *13*, 11748-11756.

(142) Seo, D. M.; Reininger, S.; Kutcher, M.; Redmond, K.; Euler, W. B.; Lucht, B. L. Role of mixed solvation and ion pairing in the solution structure of lithium ion battery electrolytes. *The Journal of Physical Chemistry C* **2015,** *119*, 14038-14046.

(143) Cvjetićanin, N. Conductivity, viscosity and IR spectra of Li, Na and Mg perchlorate solutions in propylene carbonate/water mixed solvents. *Physical Chemistry Chemical Physics* **1999,** *1*, 5157-5161.

(144) Chen, Y.; Zhang, Y.-H.; Zhao, L.-J. ATR-FTIR spectroscopic studies on aqueous $LiClO_4$, $NaClO_4$, and Mg $(ClO_4)_2$ solutions. *Physical Chemistry Chemical Physics* **2004,** *6*, 537-542.

(145) Brooksby, P. A.; Fawcett, W. R. Infrared (attenuated total reflection) study of propylene carbonate solutions containing lithium and sodium perchlorate. *Spectrochimica Acta Part A: Molecular and Biomolecular Spectroscopy* **2006,** *64*, 372-382.

(146) Gowda, N.; Naikar, S.; Reddy, G. Perchlorate ion complexes. In *Advances in Inorganic Chemistry*; Elsevier: 1984; pp 255-299.

(147) Park, S. S.; Tulchinsky, Y.; Dincă, M. Single-ion Li$^+$, Na$^+$, and Mg^{2+} solid electrolytes supported by a mesoporous anionic Cu-azolate metal-organic framework. *Journal of the American Chemical Society* **2017,** *139*, 13260-13263.

(148) Mohtadi, R.; Mizuno, F. Magnesium batteries: Current state of the art, issues and future perspectives. *Beilstein journal of nanotechnology* **2014,** *5*, 1291.

(149) Morita, M.; Araki, F.; Kashiwamura, K.; Yoshimoto, N.; Ishikawa, M. Ionic structure and conductance behavior of plasticized polymeric electrolytes containing multivalent cations. *Electrochimica acta* **2000,** *45*, 1335-1340.

(150) Allen, T.; Hoyles, M.; Kuyucak, S.; Chung, S.-H. Molecular and Brownian dynamics study of ion selectivity and conductivity in the potassium channel. *Chemical physics letters* **1999,** *313*, 358-365.

(151) Parsegian, A. Energy of an ion crossing a low dielectric membrane: solutions to four relevant electrostatic problems. *Nature* **1969,** *221*, 844-846.

(152) Devlin, D. J.; Herley, P. J. Thermal decomposition and dehydration of magnesium perchlorate hexahydrate. *Thermochimica acta* **1986,** *104*, 159-178.

(153) Devlin, D. J.; Herley, P. J. Thermal decomposition and dehydration of sodium perchlorate monohydrate. *Reactivity of solids* **1987,** *3*, 75-84.

(154) Muhuri, P. K.; Ghosh, S. K.; Hazra, D. K. Solubilities of some alkali-metal salts, tetraphenylarsonium chloride, and tetraphenylphosphonium bromide in propylene carbonate at 25. degree. C using the ion-selective electrode technique. *Journal of Chemical and Engineering Data* **1993,** *38*, 242-244.

(155) Matsuura, N.; Umemoto, K.; Takeda, Y. Formulation of stokes' radii in DMF, DMSO and propylene carbonate with solvent structure cavity size as parameter. *Bulletin of the Chemical Society of Japan* **1975,** *48*, 2253-2257.

(156) Exner, J. H.; Steiner, E. C. Solvation and ion pairing of alkali-metal alkoxides in dimethyl sulfoxide. Conductometric studies. *Journal of the American Chemical Society* **1974,** *96*, 1782-1787.

(157) Das, B.; Hazra, D. K. Conductometric, viscometric, and spectroscopic investigations on the solvation phenomena of alkali-metal ions and ion pairs in 2-methoxyethanol. *The Journal of Physical Chemistry* **1995,** *99*, 269-273.

(158) Ahrens, L. H. The use of ionization potentials Part 1. Ionic radii of the elements. *Geochimica et cosmochimica Acta* **1952,** *2*, 155-169.

(159) Wang, D.-X.; Su, M.; Yu, Z.-Y.; Wang, X.-L.; Ando, M.; Shintani, T. Separation performance of a nanofiltration membrane influenced by species and concentration of ions. *Desalination* **2005,** *175*, 219-225.

(160) Bulavin, L.; Zhyganiuk, I.; Malomuzh, M.; Pankratov, K. Specific Features of Motion of Cations and Anions in Electrolyte Solutions. *arXiv preprint arXiv:1203.3844* **2012**.

(161) Georén, P.; Lindbergh, G. Characterisation and modelling of the transport properties in lithium battery gel electrolytes: Part I. the binary electrolyte PC/LiClO4. *Electrochimica acta* **2004,** *49*, 3497-3505.

(162) Ponrouch, A.; Monti, D.; Boschin, A.; Steen, B.; Johansson, P.; Palacin, M. Non-aqueous electrolytes for sodium-ion batteries. *Journal of Materials Chemistry A* **2015,** *3*, 22-42.

(163) Bieker, G.; Winter, M.; Bieker, P. Electrochemical in situ investigations of SEI and dendrite formation on the lithium metal anode. *Physical Chemistry Chemical Physics* **2015,** *17*, 8670-8679.

(164) Li, L.; Zheng, Y.; Zhang, S.; Yang, J.; Shao, Z.; Guo, Z. Recent progress on sodium ion batteries: potential high-performance anodes. *Energy & Environmental Science* **2018,** *11*, 2310-2340.

(165) Zhang, X.; Rui, X.; Chen, D.; Tan, H.; Yang, D.; Huang, S.; Yu, Y. $Na_3V_2(PO_4)_3$: An advanced cathode for sodium-ion batteries. *Nanoscale* **2019,** *11*, 2556-2576.

(166) Muruganantham, R.; Chiu, Y.-T.; Yang, C.-C.; Wang, C.-W.; Liu, W.-R. An efficient evaluation of F-doped polyanion cathode materials with long cycle life for Na-ion batteries applications. *Scientific reports* **2017,** *7*, 1-9.

(167) Tasker, S.; Chambers, R.; Badyal, J. Surface defluorination of PTFE by sodium atoms. *The Journal of Physical Chemistry* **1994,** *98*, 12442-12446.

(168) Bouibes, A.; Takenaka, N.; Fujie, T.; Kubota, K.; Komaba, S.; Nagaoka, M. Concentration Effect of Fluoroethylene Carbonate on the Formation of Solid Electrolyte Interphase Layer in Sodium-Ion Batteries. *ACS applied materials & interfaces* **2018,** *10*, 28525-28532.

(169) Huang, J.-Q.; Zhang, Q.; Peng, H.-J.; Liu, X.-Y.; Qian, W.-Z.; Wei, F. Ionic shield for polysulfides towards highly-stable lithium-sulfur batteries. *Energy & environmental science* **2014,** *7*, 347-353.

(170) Yue, J.; Epstein, A. XPS study of self-doped conducting polyaniline and parent systems. *Macromolecules* **1991,** *24*, 4441-4445.

(171) Castner, D. G.; Hinds, K.; Grainger, D. W. X-ray photoelectron spectroscopy sulfur 2p study of organic thiol and disulfide binding interactions with gold surfaces. *Langmuir* **1996,** *12*, 5083-5086.

(172) Li, S.; Arenholz, E.; Heitz, J.; Bäuerle, D. Pulsed-laser deposition of crystalline Teflon (PTFE) films. *Applied Surface Science* **1998,** *125*, 17-22.

(173) Barchasz, C.; Molton, F.; Duboc, C.; Leprêtre, J.-C.; Patoux, S. b.; Alloin, F. Lithium/sulfur cell discharge mechanism: an original approach for intermediate species identification. *Analytical chemistry* **2012,** *84*, 3973-3980.

(174) Cuisinier, M.; Hart, C.; Balasubramanian, M.; Garsuch, A.; Nazar, L. F. Radical or not radical: revisiting lithium–sulfur electrochemistry in nonaqueous electrolytes. *Advanced Energy Materials* **2015,** *5*, 1401801.

(175) Cuisinier, M.; Cabelguen, P.-E.; Evers, S.; He, G.; Kolbeck, M.; Garsuch, A.; Bolin, T.; Balasubramanian, M.; Nazar, L. F. Sulfur speciation in Li-S batteries determined by operando X-ray absorption spectroscopy. *The Journal of Physical Chemistry Letters* **2013,** *4*, 3227-3232.

(176) Wujcik, K. H.; Pascal, T. A.; Pemmaraju, C.; Devaux, D.; Stolte, W. C.; Balsara, N. P.; Prendergast, D. Characterization of Polysulfide Radicals Present in an Ether-Based Electrolyte of a Lithium–Sulfur Battery During Initial Discharge Using In Situ X-Ray Absorption Spectroscopy Experiments and First-Principles Calculations. *Advanced Energy Materials* **2015,** *5*, 1500285.

(177) Bai, S.; Liu, X.; Zhu, K.; Wu, S.; Zhou, H. Metal-organic framework-based separator for lithium-sulfur batteries. *Nature Energy* **2016,** *1*, 1-6.